Products of reactive collisions between cold Rb atoms and an Ba^+ ion

Dissertation

zur Erlangung des akademischen Grades
Doktor der Naturwissenschaften (Dr. rer. nat.)

eingereicht an der
Fakultät für Naturwissenschaften
der
Universität Ulm

von
Amir Mohammadi
aus
Zanjan

Betreuer der Dissertation: Johannes Hecker Denschlag

2020

Amtierender Dekan: Prof. Dr. Thorsten Bernhardt
Erstgutachter: Prof. Dr. Johannes Hecker Denschlag
Zweitgutachter: Prof. Dr. Joachim Ankerhold
Tag der mündlichen Prüfung: 13. November 2020

Die in dieser Dissertation beschriebenen Arbeiten wurden durchgeführt an der

Universität Ulm
Institut für Quantenmaterie
Albert-Einstein-Allee 45
D-89069 Ulm

Abstract

For my dissertation, I have carried out experiments with a single Ba^+ ion which is immersed in a cloud of ultracold neutral Rb atoms. The ion is held in a Paul trap and is initially laser cooled to about $1\text{mK}\times k_\text{B}$. The atom cloud consists of about 10^6 Rb atoms at a typical temperature of about 1 μK and it is trapped in an optical dipole trap. In the experiments, the ion trap and the optical dipole trap are brought to an overlap and as a consequence, the ion and atoms can collide with each other. Besides elastic collisions between the two species, also a variety and concatenation of inelastic and reactive collisions can take place.

My thesis mainly consists of two parts:

In the first part, I use the elastic and reactive collisions between the atoms and the ion to investigate and fine-tune the properties of the Paul trap. A Paul trap is based on electric radio-frequency fields which exert oscillating forces on the trapped ion. In an ideal case, these electrical fields vanish at the precise location of the trapped ion. Because of imperfections in the setup, however, typically there are still some remaining electrical fields. This leads to an unwanted motion of the trapped ion, called excess-micromotion. For many of our (planned) experiments in Ulm, it is important to minimize this excess-micromotion, to obtain the lowest possible kinetic energy of the ion. It turns out that the elastic and reactive collision rates between the ion and the atoms are strongly correlated with the kinetic energy of the ion and therefore are correlated with the excess-micromotion. I show in my thesis that by minimizing losses in the Rb cloud which are due to the elastic and reactive ion-atom collisions one can suppress excess-micromotion quite well by additional radio-frequency fields that are applied to the Paul trap.

In the second part, I studied the evolution of a single $BaRb^+$ molecule while it continuously collides with ultracold Rb atoms. The $BaRb^+$ molecule forms within one ms when we immerse the cold Ba^+ ion into a dense gas of Rb. The molecule is initially weakly-bound and can undergo a sequence of elastic, inelastic, reactive, and radiative processes. I investigated these processes by developing methods for discriminating between different ion species, electronic states, and kinetic ion energy ranges. By comparing the measurements to model calculations a consistent description of the typical trajectory of the ion through the manifold of available atomic and molecular states has been gained. As a further result, rates for collisional and radiative relaxation as well as photodissociation, spin-flip collisions, and chemical reactions have been determined.

To my wife, Sepideh

who is the biggest asset of my life.

Contents

Chapter 1

Introduction

For several decays, it was an important goal to reduce the kinetic energy of atoms and make them cold and trapped, because this allows for precision measurements and a new generation of experiments in which a high degree of experimental control is available over internal and external quantum states of atoms. Cold atoms are in two classes of neutral atoms and ions and can be realized by laser cooling, a well-known technique that makes cold atoms samples near absolute zero. The idea of cooling atoms by laser beams goes back to 1975 when in independent works Hänsch and Schawlow [1] and Wineland and Dehmlet [2] suggested that the radiation pressure of quasi-monochromatic lights can be used for reducing the average translational energy of atoms.

First experiments related to the laser cooling of atoms were reported in 1978 for a cloud of Mg^+ [3] ions and Ba^+ ions [4]. Making samples of cold ions was more realistic than that of neutral atoms because ions could be first trapped with an initial temperature above the room temperature and then laser cooled. Nevertheless, in 1985, trapping of neutral Na atoms in a magnetic trap [5] and in an "optical molasses" [6] were reported. An interesting review over early studies in cold neutral atoms can be found in Ref [7]. Cooling of neutral atoms came to a new phase after successful realization of the Bose-Einstein Condensate (BEC) for rubidium-87 atoms [8] and sodium atoms [9]. In parallel to developments in cold neutral atoms systems, advances in cold ion systems reached the point that, in the 1990s, the motional ground state preparation of ions at the level of a single particle was achieved [10]. Such a great control on the quantum level led to various applications for cold ion systems such as high fidelity quantum gates [11, 12], very accurate atomic clocks [13], entangled quantum bits [14,15] and investigation of variation of fundamental constants [16,17]. Attempts for developing the ion trapping and atom cooling technique, and achieving

the BEC resulted in physics Nobel prizes 1989, 1997 and 2001. The field of cold atoms has been exploded nowadays by many topics in ultracold Fermi gases [18], optical lattices [19], magnetic atom chips [20, 21], quantum lattice gases [22], dipolar quantum gases [23, 24], many-body [25], quantum simulation [26, 27], quantum computation and information processing [28, 29], and cold chemistry [30, 31].

Due to good control over these two quantum systems of cold neutral atoms and ions, coupling them with each other has also become of interest. Merging these two distinct fields creates the new field of the hybrid atom-ion system to study collisional properties, investigate the formation, dissociation, reactions, and applications of cold molecular ions, and it provides a platform for quantum simulation, precision spectroscopy, and cold chemistry [32–34].

Currently, a number of groups are working with hybrid atom-ion as e.g., group of Stefan Willitsch from Basel (Ca^+, Ba^+ with Rb MOT) [35,36], Eric. R. Hudson from L. A. (Ba^+, Yb^+, Ca_2^+, $BaCl^+$ with Ca MOT) [16,37], Roee Ozeri from Rehovot (Sr^+ with Rb BEC) [38], Takashi Mukaiyama from Tokyo (Ca^+ with Li) [39], Sadiq Rangwala from Bangalore (Rb^+ with Rb MOT) [40], Winthrop Smith from Storrs (Na^+ with Na MOT) [41], Matthias Weidemüller from Heidelburg (OH^- with Rb Dark SPOT [1]), Rene Gerritsma from Amsterdam (Yb^+ with Rb BEC), Roland Wester from Innsbruck, Carls Sias from Florence, and excellent progress has been made in the field as many interesting results were published. Considering the fact that the hybrid atom-ion field is young, more exciting results are expected to be released by the present groups in future.

Many of these experimental advances are inspired by theoretical works. There are even a larger number of theoretical groups in the field which can not all be listed here, and their contributions to the field have been discussed elsewhere in more details [34]. There are fascinating theoretical predictions for hybrid atom-ion systems at low collision energies which are waiting to be observed. Some of my personal favorites are: Feshbach resonances for atom-ion scattering [43], shape resonances in cross sections [44], crossing from classical charge mobility to hopping conductivity for ions [45], polarons in a strongly coupled regimes [46], mesoscopic molecular ions [47].

The current experimental system in Ulm was built to study dynamics of cold trapped $^{138}Ba^+$ and $^{87}Rb^+$ in ^{87}Rb BECs at very low energies [48]. In order to reach this, the ion excess micromotion should be minimized as possible. One of the main sources for ion excess micromotion are uncompensated electrical stray fields at the Paul trap

[1] a dark spontaneous-force optical trap [42]

center. A partial minimization of ion micromotion energy has been accomplished previously in our hybrid system by compensating dc-electrical fields via ultracold gas of Rb atoms [49]. As a first part of my thesis work, I show how to compensate ion excess micromotion due to rf-electrical stray fields. Among other things, I show how to use reactive collisions to probe the ion kinetic energy. We minimize the residual rf-electrical field at the Paul trap center down to the level of about $1\,\mathrm{Vm}^{-1}$ comparable to other conventional methods reported by now [50–54].
In the second part of my thesis work, I investigate the evolution of a $BaRb^+$ molecule in an ultracold gas of Rb atoms. We find that while the molecular evolution is dominated by vibrational relaxation for the most weakly-bound levels, radiative processes become increasingly important for more deeply bound levels. We also determine the fraction of other ion species that can be formed in our experiments due to photodissociation of the $BaRb^+$ ion with 1064 nm laser beam, or due to the substitution reaction of this molecular ion with neutral Rb atoms. We show how differently the $BaRb^+$ molecular ions behave depending on their electronic state. Some of the methods presented in this thesis are very general and can be directly adopted for studies of other ion-atom species. The results of this work can be helpful for developing novel methods for preparing, manipulating and probing a variety of molecular states.

Overview of thesis

This Ph.D. thesis is structured as follows:
Chapter 2 gives a short introduction to the basics of a hybrid atom-ion system. I discuss in this chapter the cross-sections that are used for explaining the atom-ion collisions from classical and semi-classical perspective.
In **chapter 3**, I shortly introduce our experimental setup and explain in some detail the procedure of preparing cold Ba^+ ions and ultracold Rb atoms. Trapping parameters and detection of other ion species that are produced in our experiments are also discussed in this chapter.
In **chapter 4**, the ion excess-micromotion caused by rf-electric field sources is discussed in our ion trap. I explain the methods that are used to compensate parasitic rf-fields in our Paul trap center and the detail of calculations for determining the ion kinetic energy.
In **chapter 5**, we study the evolution of a single $BaRb^+$ molecule while it keeps colliding with ultracold Rb atoms. The initially weakly-bound molecule can undergo a

sequence of elastic, inelastic, reactive, and radiative processes. We investigate these processes by developing methods for discriminating between different ion species, electronic states, and kinetic ion energy ranges.

In **chapter 6**, I summarize the result and give a short outlook about possible future projects that can be investigated in our hybrid atom-ion system.

Chapter 7 contains all appendices sections including some detail of calculations, theoretical models and, simulation of experimental data.

Chapter 2

The basics of a hybrid atom-ion system

2.1 The atom-ion interaction

An ion considered as a point charge Q with the electrical field of $\xi(r) = |Q/4\pi\epsilon_0 r^2|$ can induce the dipole moment of $p(r) = \alpha_{at}\xi(r)$ to a nearby atom where ϵ_0 and $\alpha_{\rm at}$ are the vacuum permittivity and the static electric dipole polarizability of the neutral atom, respectively (see figure 2.1). This leads to a long-range interaction potential

$$V(r) = -\frac{1}{2}p(r)\xi(r) = -\frac{C_4}{2r^4}\,. \tag{2.1}$$

Considering the partial waves l we obtain the effective potential of $-C_4/2r^4 + l(l+1)\hbar^2/(2\mu r^2)$ where μ is the reduced mass of the atom-ion system. For the first non-zero angular momentum, i.e. p-wave scattering, the potential barrier is located at

$$r^* = \sqrt{\frac{\mu C_4}{\hbar^2}}\,, \tag{2.2}$$

where r^* is defined as the characteristic length scale for atom-ion collisions. By using r^*, one can determine a characteristic collision energy $E^*_{\rm col}$ as

$$E^*_{\rm col} = \frac{\hbar^2}{2\mu r^{*2}} \tag{2.3}$$

which indicates how far we should reduce the collision energy to reach to the s-wave scattering regime in the atom-ion experiment. In our hybrid system, by using $\alpha_{\rm at}$=$4\pi\epsilon_0 \times 47.39\mathring{A}^3$ for ^{87}Rb atoms [55], r^* and $E^*_{\rm col}$ for a colliding pair of ^{138}Ba

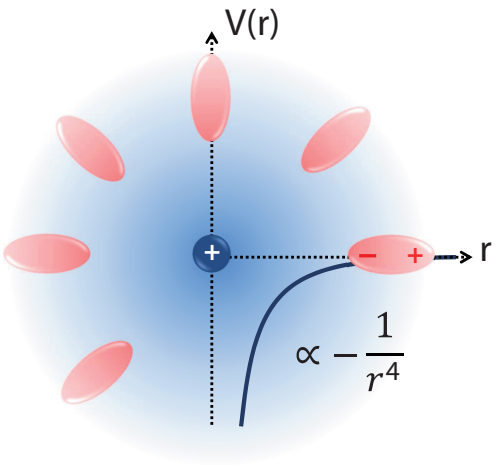

Figure 2.1: An ion as an impurity inside a cloud of ultracold neutral atoms. The electric field of the ion polarizes nearby atoms. The interaction potential between the ion and the atom is attractive and inversely proportional to r^4.

ion and ^{87}Rb atom are approximately 300 nm and 40 $k_B\times$nK, respectively. In the homonuclear case of a ^{87}Rb ion and a ^{87}Rb atom, these values change to about 280 nm and 70 $k_B\times$nK. For the ultracold atomic ensemble of ^{87}Rb atoms, the s-wave scattering length is roughly 5 nm [56].

2.1.1 Langevin cross section

In a classical description (see figure 2.2) we distinguish two types of collisions: glancing collisions and Langevin collisions. If the impact parameter b is smaller than the critical impact parameter b_c a Langevin collision takes place otherwise we expect a glancing collision. In the Langevin collision, the kinetic energy exchange can be large while in the glancing collision there is a small momentum transfer between colliding particles. The trajectory can be described by taking the atom and the ion in the same plane during the collision which we take to be in x-y plane, $\vec{r} = r\cos\hat{x} + r\sin\hat{y}$. Here, r is the distance between atom and ion. The total collision energy of the particle is given by

$$E_{\text{col}} = \frac{\mu}{2}(\dot{r}^2 + r^2\dot{\varphi}^2) - \frac{C_4}{2r^4}\,. \tag{2.4}$$

Furthermore, at $r \longrightarrow \infty$ the relative velocity of the atom and the ion is v_0 which gives the total energy of

$$E_{\rm col} = \frac{\mu}{2} v_0^2 \,. \tag{2.5}$$

The angular momentum conservation of the system before and after the collision says that $L = b\mu v_0 = \mu r^2 \dot{\varphi}$ where $\vec{L} = L\hat{z}$, in our coordinates and b is the impact parameter. By considering equations (2.4) and (2.5) and using the angular momentum conservation, $\dot{r}$ can be expressed by

$$\dot{r} = \pm v_0 (1 - \frac{b^2}{r^2} + \frac{C_4}{\mu r^4 v_0^2})^{1/2} \,. \tag{2.6}$$

By taking $\dot{r} = 0$, the above expression gives the closest distance of the atom to the ion. This distance is introduced as r_0 in figure 2.2 and it's given by

$$r_0^2 = \frac{b^2}{2} \pm (\frac{b^4}{4} - \frac{C_4}{\mu v_0^2})^{1/2} \,. \tag{2.7}$$

We can define a critical impact parameter $b_{\rm c} = (4C_4/\mu v_0^2)^{1/4}$. For the case $b < b_c$, the atom and the ion have a spiraling motion onto each other until a hardcore collision takes place between two nuclei. After having a hardcore collision, the atom will be scattered outward almost isotropically. Langevin collisions [57] have the cross section of $\sigma_{\rm Lng} = \pi b_{\rm c}^2$.

Langevin collisions can give rise to inelastic and reactive collisions, e.g. forming a molecule, spin-exchange or charge transfer. If inelastic and reactive collisions happen at a close distance, then the rate of these collisions should be independent of collision energy. This can be seen in the Langevin collision rate of $\Gamma_{\rm Lng} = n_{\rm at}\sigma_{\rm Lng}\sqrt{2E_{\rm col}/\mu}$ where $n_{\rm at}$ is the atomic density and the square root is the relative velocity. Considering that $\sigma_{\rm Lng} \propto E_{\rm col}^{-1/2}$, the Langevin rate becomes a collision energy independent rate which is given by $\Gamma_{\rm Lng} = 2\pi \times n_{\rm at}\sqrt{C_4/\mu}$. For a Ba^+ that collides with a Rb atom, $\Gamma_{\rm Lng} \simeq n_{\rm at} \times 2.44 \times 10^{-9}\,{\rm cm^3 s^{-1}}$. It gives rise to a Langevin rate of about 2.4 $\rm ms^{-1}$ for atomic density $n_{\rm at} = 1 \times 10^{12}{\rm cm^{-3}}$.

2.1.2 Semi-classical cross section

To obtain a cross-section for elastic two-body collisions in an atom-ion system, one needs to consider Langevin collisions and glancing collisions. The cross-section of the atom-ion system can be written as sum of the contribution of each partial wave

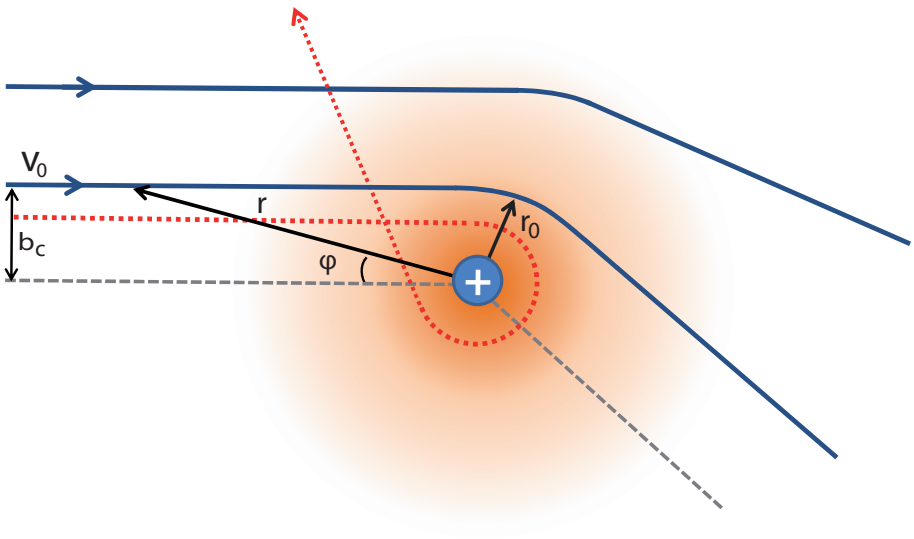

Figure 2.2: A classical picture for trajectories of atoms with a velocity of v_0 entering the polarization potential of the ion. For impact parameters larger than b_c, there are glancing collisions during which the atom trajectory gets slightly deflected as the blue curves show for two different incoming atoms. For impact parameters smaller than b_c, e.g. the red dashed curve, a hardcore collision is expected between two nuclei known as Langevin collisions which lead to an isotropic scattering. r_0 is the minimal distance between atom and ion for the collision with the critical impact parameter b_c.

as [58]

$$\sigma_{\mathrm{el}} = \frac{4\pi}{k^2} \sum_{l=0}^{\infty} (2l+1) \sin^2(\eta_l) \,, \tag{2.8}$$

where k and η_l are the corresponding wave number of the collision and the phase shift of the lth partial wave, respectively. The exact value of η_l depends on the potential of the scatterer. To determine the cross-section for each partial wave, the Schrödinger equation for that partial wave has to be solved to calculate the corresponding phase shift of the wave function. The elastic scattering phase shift can be obtained from the asymptotic form of

$$\psi_l(kr) \sim \sin[kr - \frac{l\pi}{2} + \eta_l] \,, \tag{2.9}$$

for large distances r. In our cold atom-ion experiments in Ulm, the collision energy is typically around a few mK$\times k_{\mathrm{B}}$. Some lower partial waves can pass over the angular momentum and collide with the core. For some collision energies and partial waves, there are resonance features (called shape resonances) in the scattering cross section. It occurs when for a specific partial wave, the energy level behind the

centrifugal potential barrier matches the collision energy. In this case, the probability of tunneling through the potential barrier increases significantly allowing a collision with the core potential. The atoms which are reflected back from the centrifugal barrier correspond to glancing collisions and the other ones correspond to Langevin collisions.
Without knowing the exact form of the interaction potential in equation (2.8) and by assuming that partial waves are scattered either by the centrifugal barrier or the core potential, one can make an independent approximation for each part, calculate the cross section and sum up the results which lead to a semi-classical approximation [59]

$$\sigma_{\rm el}(E_{\rm col}) \simeq \pi\Big(\frac{\mu C_4^2}{\hbar^2}\Big)^{1/3}\Big(1+\frac{\pi^2}{16}\Big)E_{\rm col}^{-1/3}\,. \tag{2.10}$$

For a hybrid system of Ba^+-Rb, the rate of elastic binary collision is given by $\Gamma_{\rm el} = n_{\rm at}\sigma_{\rm el}\sqrt{2E_{\rm col}/\mu}$. For a collision energy of $1\,{\rm mK}\times k_{\rm B}$ and atomic density $n_{\rm at} = 1\times 10^{12}\,{\rm cm}^{-3}$, $\Gamma_{\rm el} \approx 12.4\ {\rm ms}^{-1}$ which is almost a factor of 6 larger compared with the Langevin rate.

2.2 Reactive collisions in the Ba^+-Rb system

In our hybrid system, the following two-body reactive collisions

$$\begin{aligned} &1)\ {\rm Rb} + {\rm Ba}^+ \longrightarrow {\rm Ba}\ + {\rm Rb}^+ + \gamma \qquad \text{(Radiative charge exchange)} \\ &2)\ {\rm Rb} + {\rm Ba}^+ \longrightarrow {\rm BaRb}^+ + \gamma \qquad\quad \text{(Radiative association)}\,, \end{aligned}$$

are possible between the Ba^+ ion and the Rb atom due to the shape of the inter-nuclear potential energy curves (see figure 2.3). The energy difference between the input channel (i.e., the Rb(5s)+Ba^+ (6s) asymptote) and the output channel (i.e., Rb+Ba^+($6s^2$) asymptote) is mainly taken away by the emitted photon γ and, the RA process leads to the formation of a translationally cold and deeply bound $BaRb^+$ while the RCT process produces a translationally cold Rb^+ ion.
Besides two-body collisons, three-body collisions are also observed in our experiment. In this case, a Ba^+ ion can react with two Rb atoms to form a translationally cold and weakly-bound $BaRb^+$ ion. The total reaction rate of Ba^+ inside the Rb atomic cloud is given by $\Gamma^{(2)}_{\rm rec.}+\Gamma^{(3)}_{\rm rec.}$ where $\Gamma^{(2)}_{\rm rec.}$ and $\Gamma^{(3)}_{\rm rec.}$ are the two- and three-body reaction rates, respectively. More details about two- and three-body reactive collisions in our Ba^+-Rb system can be found in Appendices C and D.

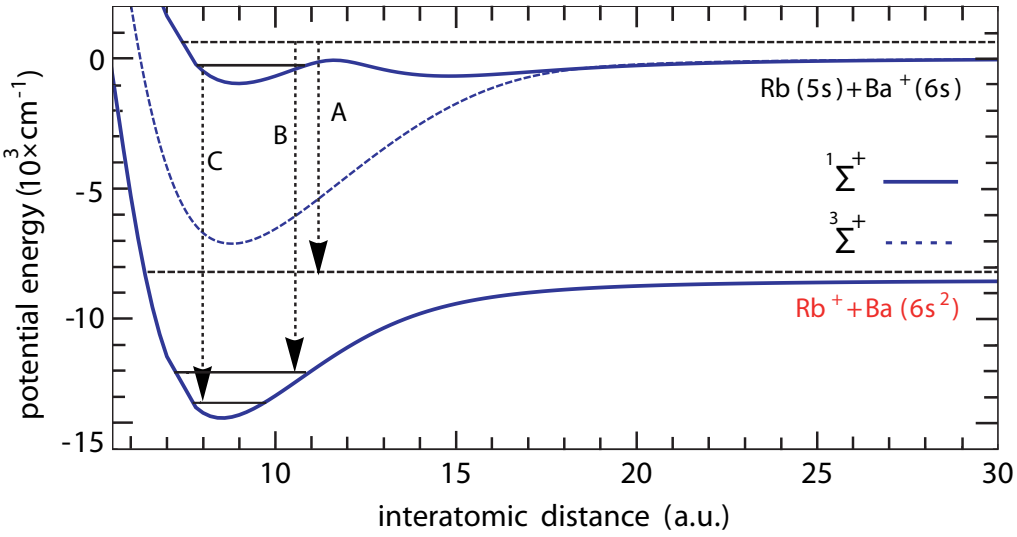

Figure 2.3: Three possible reactions in a Ba^+-Rb hybrid system. The processes A, B, and C are radiative charge transfer(RCT), radiative association (RA) and bound to bound radiative relaxation. Potential curves are taken from Ref [60].

2.3 Cold molecular ion-atom hybrid system

Besides the atomic ions, the collisional dynamics of molecular ions with neutral atoms can also be investigated in a hybrid atom-ion system. Molecules have more internal degrees of freedom than that of atoms and therefore, providing a system in which molecules and atoms can interact is a very interesting platform for investigating chemical processes.

By a hybrid atom-ion system, the collisional dynamics of a molecular ion in a bath of neutral atoms can also be investigated. There are inelastic collisions that change the rovibrational state of the molecule as well as the spin-state. There are also reactive collisions that dissociate the molecule or make substitution reactions. Elastic collisions with neutral atoms can also occur in a molecular ion-atom system which leads to the sympathetic cooling of the molecule.

In chapter 5, I discuss the collisions of a single $BaRb^+$ ion with neutral Rb atoms in our hybrid atom-ion system. A weakly-bound $BaRb^+$ ion can be understood as consisting of two almost unperturbed individual atoms; a Ba^+ ion and a neutral atom. When another free Rb atom approaches such a system with a distance much larger than the binding length of the molecule, one can consider the whole system as

a single charged particle with a total mass of the BaRb molecule that collides with a Rb atom. In this case, all cross-sections discussed in subsections 2.1.1 and 2.1.2 can also be applied to the molecular ion-atom system.

Chapter 3

Experimental setup

In our hybrid atom-ion system, we work with a single $^{138}Ba^+$ ion or a crystal of $^{138}Ba^+$ ions and an ensemble of spin-polarized ^{87}Rb neutral atoms. We can run experiments with different atomic densities of $n_{\rm at} \sim 10^{11}$-10^{14} cm^{-3} and collision energies of a few mK to a few hundred mK$\times k_{\rm B}$. An overview of our experimental setup can be found elsewhere [48]. In following sections, I shortly review how ions and atoms are prepared for the experiments.

3.1 The cold ion system

3.1.1 A linear Paul trap

We use a symmetric linear Paul trap to confine the Ba^+ (or $BaRb^+$, Rb_2^+, Rb^+) ions. Linear Paul traps consist of four electrodes known as rf-electrodes which confine the ion radially by producing an oscillating quadrupole electric field. Two end-cap electrodes with static potentials lead to axial confinement of the ion. In the symmetric Paul trap, the rf electrodes are held an electrostatic potential of $\pm V_0 \cos \Omega t$. We use $\Omega \simeq 2\pi \times 4.2$ MHz and $V_0 \approx 150$ V for our ion trap and a static potential of about 7.6 V for end-cap electrodes. Near the Paul trap center, the potential can be estimated by

$$\Phi(x,y,z,t) = \frac{V_0}{{R_0}^2}[x^2 - y^2]\cos\Omega t + \frac{\kappa U_0}{Z_0^2}[z^2 - \frac{(x^2+y^2)}{2}]\,, \tag{3.1}$$

where $R_0 = 2.6$ mm and $Z_0 = 7$ mm are the distance of the rf- and endcap electrode to the Paul trap center. Here, $\kappa = 0.29$ is a geometrical factor related to the Paul trap configuration. For an ion with a mass of $m_{\rm i}$ and the charge of e, the equation of motion can be written as $-e\vec{\nabla}\Phi(x,y,z,t)/m_{\rm i} = \ddot{\vec{r}}(x,y,z,t)$ where

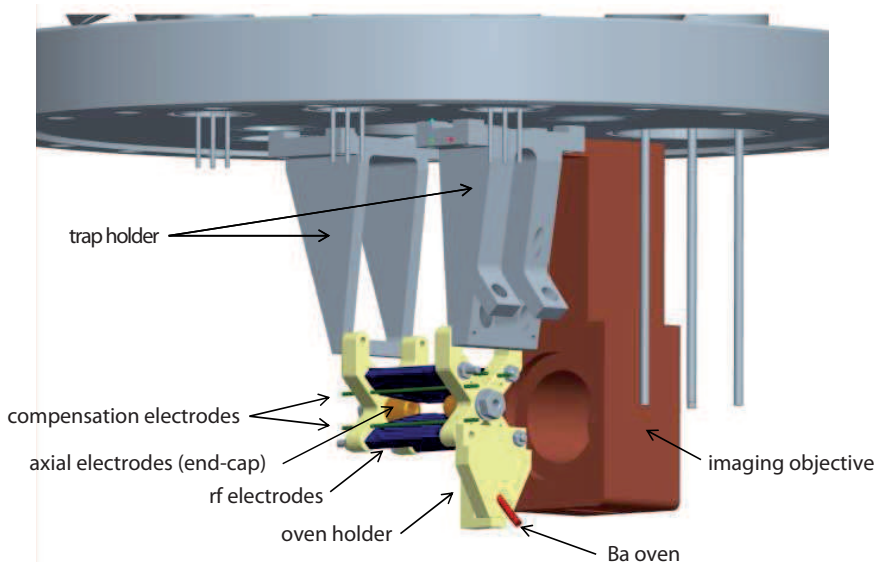

Figure 3.1: The linear Paul trap in our science chamber. The optical trap for atoms and the ion cooling beams are not shown here.

$\vec{r}(x, y, z, t)$ is the displacement vector of the ion around the Paul trap center. The equation of motion leads to the Mathieu equation

$$\ddot{\vec{r}_j} + [a_j + 2q_j \cos(2\tau)]\vec{r_j} = 0\,, \tag{3.2}$$

where $j = (x, y, z)$ and $\tau = \Omega t/2$. Here, a_j and q_j, are defined as $\{a_x, a_y, a_z\} = \{a, a, -2a\}$ and $\{q_x, q_y, q_z\} = \{q, -q, 0\}$ where $a = -4e\kappa U_0/m_{\rm i}Z_0^2\Omega^2$ and $q = 4eV_0/m_{\rm i}R_0^2\Omega^2$. Mathieu equation (3.2) has several stability regions for different values of a and q. Ions are confined in the Paul trap if they are in these stability regions. For our case, i.e., $|a| \ll 1$ and $|q| \ll 1$, we are in the first stability region of the Mathieu equation (see figure 3.2) and the ion position can be well described by [61]

$$r_j(t) = r_{j0}\cos(\omega_j t + \phi_j^*)[1 + \frac{q_j}{2}\cos\Omega t]\,, \tag{3.3}$$

where $\omega_j \cong \frac{\Omega}{2}\sqrt{a_j + q_j^2/2}$ is the trapping frequency and r_{j0} is the oscillation amplitude of the ion around the Paul trap center for $j = (x, y, z)$. Here, ϕ_j^* is a phase related to the initial position and the velocity of the ion. I listed in table 3.1 the typical trapping frequencies and the values of a and q for the ion species we use in our experiments.

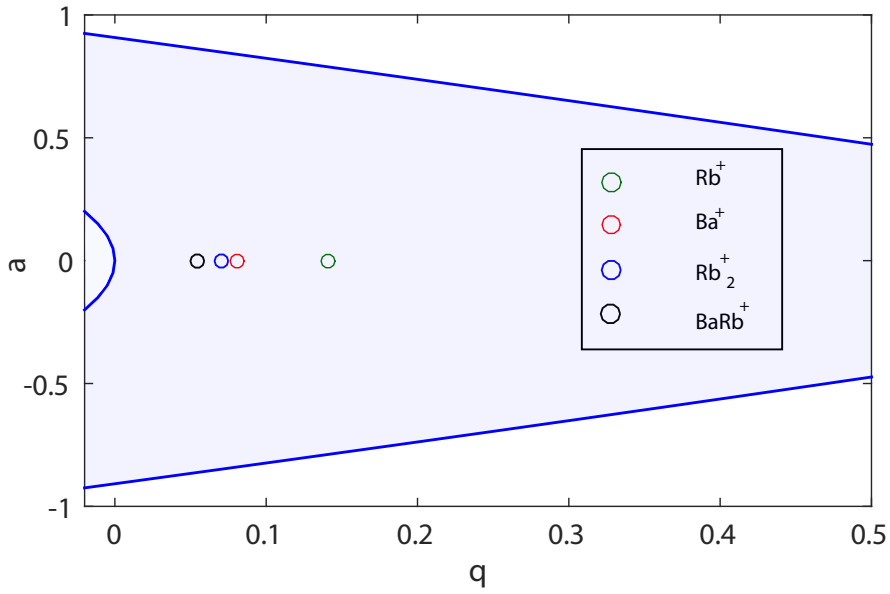

Figure 3.2: The stability diagram of ion species given in table 3.1. All ions are inside the first stability region (colored area) of the Paul trap. Parameters a and q are related to the Paul trap configuration and the mass of the charged particle, see text for more detail.

Figure 3.1 shows the schematic of our Paul trap and its location in the vacuum chamber. The trapping potential is deep enough ($\sim$ 1eV) to confine ions with kinetic energies of up to $10.000\mathrm{K} \times k_\mathrm{B}$. There are four additional electrodes (colored green in figure 3.1) that are used for compensating stray electric fields at the ion trap center. A stray dc electric field of $\vec{\mathcal{E}}_\mathrm{dc}$ at the Paul trap center changes equation (3.3) to [61]

$$r_j(t) = [r_{j0}^{'} + r_{j0}\cos(\omega_j t + \phi_j^*)][1 + \frac{q_j}{2}\cos\Omega t]\,, \tag{3.4}$$

and causes an excess micromotion for the ion with an amplitude of $r_{j0}^{'} = e\vec{\mathcal{E}}_\mathrm{dc}.\hat{j}/(m_\mathrm{i}\omega_j^2)$. From equation (3.4), the average kinetic energy of the ion can be written as [61]

$$E_{Kj} \cong \frac{m_\mathrm{i}}{4} r_{j0}^2(\omega_j^2 + \frac{1}{8}q_j^2\Omega^2) + \frac{m_\mathrm{i}}{16}(r_{j0}^{'}q_j\Omega)^2\,. \tag{3.5}$$

As equation (3.5) shows, uncompensated electric fields at the Paul trap center determines on average the atom-ion collision energy. Therefore, the compensation electrodes can be used to vary the collision energy in the experiments.

Table 3.1: Typical trapping frequencies of different ion species in our linear Paul trap.

ion	radial (kHz)	axial (kHz)	a	q
$^{138}Ba^+$	130	38.8	1.7×10^{-4}	0.08
$^{87}Rb^+$	206	49	2.7×10^{-4}	0.13
Rb_2^+	103	34.5	1.3×10^{-4}	0.068
$BaRb^+$	80	30	1×10^{-4}	0.05

3.1.2 Production of Ba^+ ions

A beam of neutral barium atoms is released toward the ion trap center by heating the barium oven with a high current. Ba^+ ions are produced by ionizing the neutral Barium atoms with 413 nm and 560 nm laser beams. The relevant energy levels for the Barium ionization scheme are shown in figure 3.3. We perform our experiment with ^{138}Ba ions which have an abundance of 71.7%. To avoid exciting other isotopes of the barium, we align the path of the 413 nm beam to be orthogonal to the path of the emitted atomic beam of the barium.
The rate of producing the Ba^+ ions depends on the atomic flux of Barium atoms and the time during which the Ba atoms are exposed to the ionization beam. Therefore, by adjusting the ionization time and the heating rate of the oven, we can select to either dominantly catch a single ion or to produce a crystal of Ba ions.

3.1.3 Laser cooling of the Ba^+ ion

In the beginning, the trapped Ba ions are extremely hot and need to be cooled down. We use a 493 nm laser beam and a 650 nm laser beam which are spatially overlapped as cooling and re-pumper beams, respectively. As it is shown in figure 3.3, the 493 nm laser drives the transition between $6S_{1/2}$ and $6P_{1/2}$. The Ba^+ in the excited $6P_{1/2}$ state can decay to the ground state $6S_{1/2}$ or to the meta-stable state $5D_{3/2}$ with a ratio of 3 to 1. The selected isotope (^{138}Ba) has no nuclear spin and therefore no hyperfine structure. There is no initial polarization for the spin of the ground state Ba^+ ion in our experiments. The excited state $6P_{1/2}$ has a natural linewidth 15.1 MHz which leads to a Doppler temperature of around 360 μK. Since the transition $6P_{1/2} \rightarrow 5D_{5/2}$ is not dipole allowed, decay into this meta-stable state is very unlikely during laser cooling. To depopulate the ion from this meta-stable

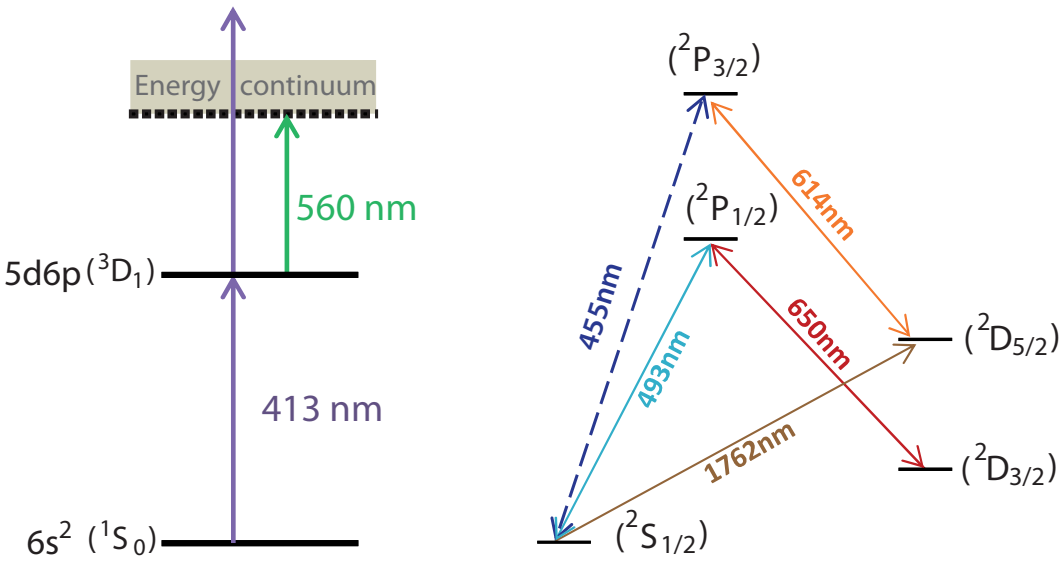

Figure 3.3: Left: The schematic of relevant barium energy levels (not to scale) for the ionization procedure in the left and, Right: the energy level of the barium ion for laser cooling on the right hand side.

state, a 614 nm laser beam is used. We collect around 1% of the scattered photons of the Ba ion(s) with a lens and the light will be imaged onto the chip of the EM-CCD camera. The resolution of the imaging system (i.e., diffraction limit) is about 1.6 μm which is much smaller than the distance between two ions in an ion string.

3.1.4 Detection of non-laser cooled ions

When there is no laser cooling available, we use another detector which is the dilute atomic clouds of ^{87}Rb with a density $n_{\text{at}} \sim 10^{11} - 10^{12}\,\text{cm}^{-3}$. Here, the detected signal is the atom loss which is mostly due to elastic collisions between the atom and the ion. Since the kinetic energy of ions are orders of magnitude larger than that of atoms, collisions transfer kinetic energy from the ion to the atoms. Consequently, atoms find an energy well above their trapping depth and leave the trap [1].
We start to detect ions by modulating the voltages on the compensation electrodes of the Paul trap. For modulation frequency, we use the radial trapping frequency of the ion species we would like to detect (see table 3.1). The method is very mass-selective meaning ion species will be only excited with their radial trapping frequencies. When

[1]To read more about how the atom loss can be modeled in our atom-ion system, see section 4.4.1.

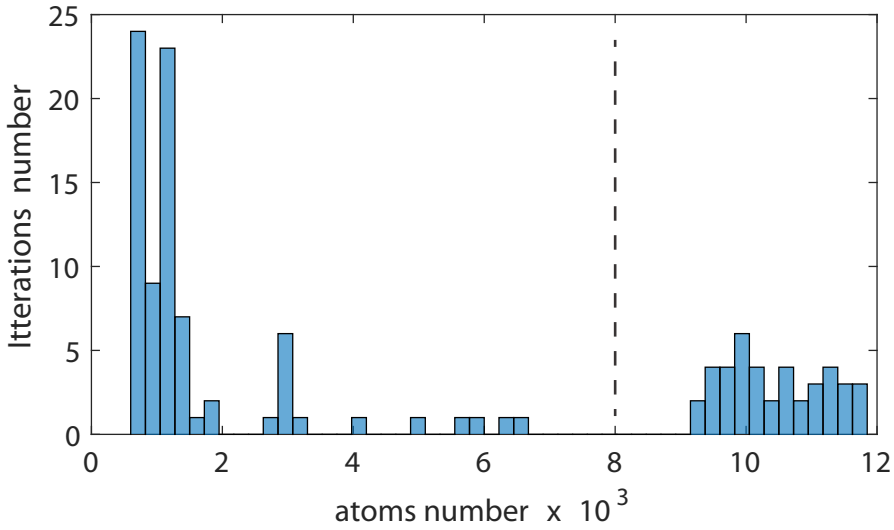

Figure 3.4: A sample histogram which shows the number of Rb atoms after overlapping the atom trap and the ion trap centers for a fixed interaction time of 15 s. Data is for 120 iterations and all cases with atoms number larger than the discriminator line of 80 K have no atom loss due to collision with Rb atoms meaning there was no ion inside the Paul trap after the modulation. Data belongs to the detection of the $BaRb^+$ ion in one of our experiments explained in chapter 5.

the ion trap modulation is over, we prepare a dilute cloud of Rb atoms and overlap the atoms center with the ion trap center letting them interact for fixed interaction time. It causes a significant atom loss if there is a charged particle in the Paul trap and, atoms number remains unchanged when the ion trap is empty. Therefore, the probability of observing the X^+ ion, where X^+ is one of the given ion species in table 3.1, is calculated by

$$P_{X^+} = \frac{\text{number of iterations with no atom loss}}{\text{total number of iterations}} . \tag{3.6}$$

Figure 3.4 shows one sample data by which we can determine P_{BaRb^+}. Data were obtained after modulating the ion trap with the trapping frequency of $\omega_{BaRb^+}/2\pi = 80\,\text{kHz}$ for 3 s and then overlapping the ion and atom trap centers for 15 s. To get some statistics, the process of detection has been repeated 120 times. The relatively long interaction time of 15 s was used mainly because of detecting ions which have very high kinetic energy. When the ion is kinematically hot, it has an orbit that is much larger than the probe atomic cloud with typical radial and axial sizes of $9\,\mu$m $60\,\mu$m, respectively. In this case, the atom-ion overlap and consequently that atom

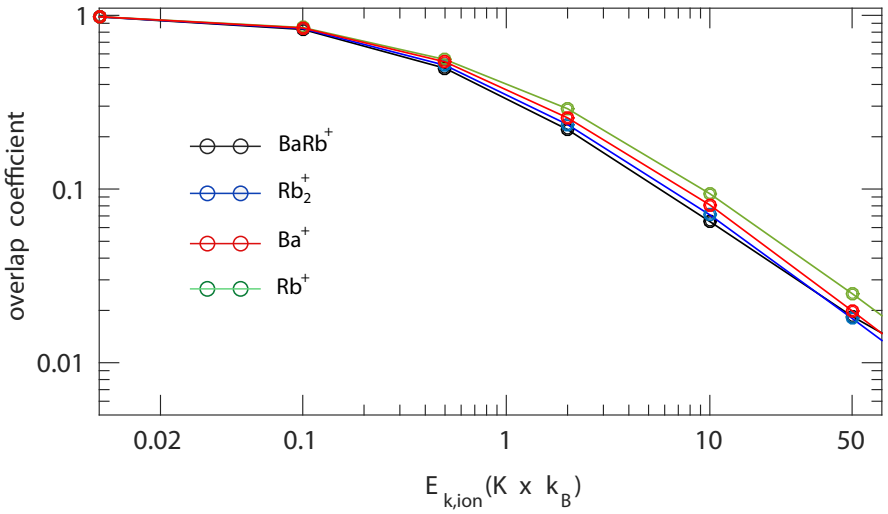

Figure 3.5: Overlap coefficients between the probe atomic cloud and ion species in our experiments as functions of ions kinetic energies. Curves are just lines connecting data points.

loss signal decrease significantly or it may stop.

By running a simple simulation based on parameters of our atom - ion system, one can determine an overlap coefficient for ion species of table 3.1 as functions of their initial kinetic energies. Figure 3.5 shows the simulation results. The simulation uses equation (3.3) to calculate the ion position by taking random values for ϕ_j^* based on the given initial kinetic energy of $E_{\mathrm{k,\,ion}}$. For simplicity, we assume only a secular motion and no micromotion for the ion by taking $(1 + q_j \cos \Omega t/2) \approx 1$ in equation (3.3). The simulation calculates the ion position for 1 s after overlapping the atoms and the ion centers. The time advances in small steps of 10 ns which results in 10^8 calculated positions for the ion. We repeat the simulation above for 10^3 times every time starting with a new initial phase ϕ_j^* for $j = (x, y, z)$ to get some average for the ion positions during its secular motions around the Paul trap center. We simply define an atom-ion overlap coefficient by taking the number of ion positions in which the ion is inside the atomic cloud divided by the number of total positions. We use a Gaussian distribution for the Rb cloud with the radial and the axial size of 6 μm and 9 μm, respectively.

For instance, for a Ba^+ ion that is shifted into the atomic cloud and has an initial kinetic energy of $50\,\mathrm{K} \times k_\mathrm{B}$, the overlap coefficient is about 0.02 meaning that it will take a factor of 50 longer than for the case where the ion is fully immersed in the cloud to a collision takes place between the ion and the atom.

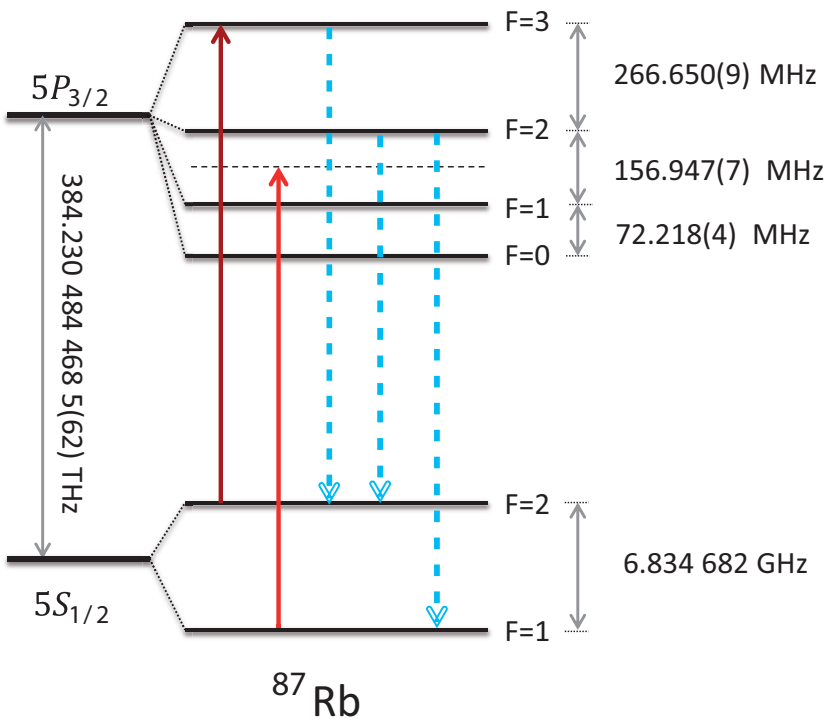

Figure 3.6: The schematic of ^{87}Rb energy levels (not to scale) for the D_2 transition line and laser frequencies which are used to create the MOT. The dark red arrow depicts the master frequency which is locked on the transition between $F = 2$ of the ground state and $F = 3$ of the excited state. This laser drives the main cooling cycle. The lighter red arrow represents the re-pumper beam (tuned to the red by $\sim 87.5\,\mathrm{MHz}$) which is locked on the transition between $F = 1$ and the crossover peak of $F = 1$ and $F = 2$. The dashed-blue arrows show spontaneous emissions to the ground state. Data for the transition frequencies are taken from [62, 63].

Collisions with atoms reduce the ion kinetic energy and increase the overlap coefficient. The cooling process takes always some time that varies depending on the atom-ion mass ratio and the initial kinetic energy of the ion.

3.2 Preparation of cold atoms

We prepare atoms in three steps in our experimental setup. Figure 3.7 shows a simplified schematic of our experimental setup. In the following, I discuss each step very briefly.

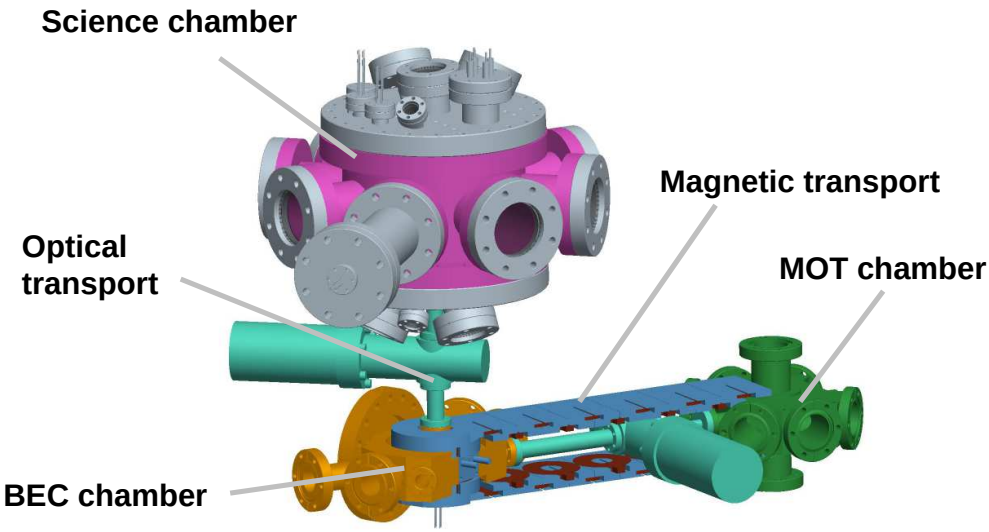

Figure 3.7: A simplified schematic of our experimental setup.

3.2.1 Magneto-optical trap (MOT)

In the first step, a Rb MOT is created in the MOT chamber using 780 nm laser beams which are locked to the D_2 line of the Rb atom (see figure 3.6). Atoms are then optically pumped into the quantum state $F = 1, m_F = -1$ to polarize the atoms and prepare them in a low seeking magnetic field state for magnetic transportation. Afterward, the atoms are pushed toward the next chamber called the BEC chamber via a magnetic transport system which has around 50% efficiency.

3.2.2 Quadrupole-Ioffe configuration (QUIC) magnetic trap

After reaching the BEC chamber, Rb atoms are loaded into a QUIC trap (i.e., quadrpol ioffe configuration trap) [64]. A strong magnetic gradient is used to confine atoms within the BEC chamber and at the same time, an optical dipole trap consists of a 1064 nm focussed high power laser beam is utilized to provide an additional trapping potential. By applying forced evaporative cooling, the temperature of the atomic cloud is reduced by two orders of magnitude. At this temperature (i.e., $\sim 1\,\mu$K), the thermal vapor can be entirely trapped by the dipole trap beam. In the optical trap, we can continue with evaporation to reach the sub μK regime and to achieve BEC.

3.2.3 Optical dipole trap

As the final step of preparation, atoms in the BEC chamber are transported to the last chamber (i.e., Science chamber) where the Paul trap is located. For transferring atoms from the BEC to the Science chamber, an optical elevator (moving optical lattice) is used which consists of two high power, and counter-propagating 1064 nm laser beams. The beams have been aligned such that they connect the Paul trap center with the center of the BEC chamber. The process of transporting and loading the atoms is aimed to be adiabatic and again approximately half of the trapped atoms can be brought into the upper chamber. Finally, when the transportation is over, another 1064 nm beam with a beam waist of about 95μm and the intensity of 14 kW/cm^2 crosses the lattice beam at a right angle and form a crossed dipole trap for atoms in the Science chamber. The atoms form a cigar-shaped cloud with the radial and the axial size of about 9 and 60 μm, respectively, for typical trap frequencies $(\omega_r; \omega_z) = 2\pi \times (145, 23)$ Hz. Here, subscripts r and z denote the radial and the axial axes of the atomic dipole trap. The axial axis of the atomic cloud forms an angle of 45° with respect to the ion trap axis. The depth of the crossed optical trap is about 20 μK so that atoms with 1 μK temperature or colder can be easily trapped. We image the cloud after some time of flight (TOF) to determine the atom number and the temperature of the atomic cloud. Thermal atomic clouds as well as a BEC can be obtained in the Science chamber in a controlled way.

Chapter 4

Minimizing rf-induced excess micromotion of a trapped ion

Reprint with permission

Material from:'Amir Mohammadi, Joschka Wolf, Artjom Krükow, Markus Deiß, and Johannes Hecker Denschlag, Minimizing rf-induced excess micromotion of a trapped ion, Applied Physics B: Lasers and Optics, published 2019, Springer-Verlag GmbH Germany'

Abstract

We report on the compensation of excess micromotion due to parasitic rf-electric fields in a Paul trap. The parasitic rf-electric fields stem from the Paul trap drive but cause excess micromotion, e.g. due to imperfections in the setup of the Paul trap. We compensate these fields by applying rf-voltages of the same frequency but adequate phases and amplitudes to Paul trap electrodes. The magnitude of micromotion is probed by studying elastic collision rates of the trapped ion with a gas of ultracold neutral atoms. Furthermore, we demonstrate that also reactive collisions can be used to quantify micromotion. We achieve compensation efficiencies of about $1\,\mathrm{Vm}^{-1}$, which is comparable to other conventional methods.

4.1 Introduction

Ideally, a single ion located in the center of a Paul trap experiences vanishing rf-trap fields, leading to vanishing micromotion. Typically, however, electrical stray fields and imperfections of the trap setup lead to a remaining level of micromotion, the excess micromotion. Minimization of this micromotion is important for many research fields such as quantum information processing [65, 66], quantum simulation [67], high precision spectroscopy [68,69], single-ion atomic clocks [70], and cold atom-ion collisions where reaching the s-wave regime is a challenge [34, 71, 72]. Therefore, in recent years much effort has been put into the investigation and minimization of micromotion. A variety of detection and compensation methods have been developed, which generally rely on optical probing the motional state of the ion (see, e.g. [50–54, 61, 73–75]). Recently, our group has demonstrated that excess micromotion due to static stray electrical fields can be sensitively probed and compensated with the help of a cold cloud of atoms which elastically collide with the ion [49]. This method can also be applied to ions that are not laser-cooled. Furthermore, it is direction independent, in contrast to sideband techniques as described e.g. in [61].

Here, we extend our work of [49] and demonstrate the minimization of excess micromotion which is linked to rf-electric fields of the Paul trap. In particular, we compensate phase micromotion which is due to a time delay in the oscillating rf-voltages of opposite Paul trap electrodes. Furthermore, we compensate rf-induced micromotion along the axial direction of our linear Paul trap which can arise from rf-pick up on the endcap dc-electrodes or simply from imperfections in the alignment of electrodes. As a further development of the minimization method as compared

to [49] we show that instead of elastic collisions also reactive collisions between the ion and atoms can be used to probe excess micromotion. In fact, making use of the known scaling law of the reaction rate with collisional energy we can determine by which factor the kinetic energy of the ion is decreased. After minimization of the excess micromotion due to both dc- and rf-fields we estimate the remaining total residual excess rf-field amplitudes to be about $1\,\mathrm{Vm}^{-1}$ and the excess dc-fields to be about $0.02\,\mathrm{Vm}^{-1}$. These compensation results are comparable to values reported using other methods [50–54].

This chapter is structured as follows. In section 4.2 we describe our ion trap setup and provide a brief review on excess micromotion. Then, in section 4.3 our detection method for micromotion is introduced. Section 4.4 is dedicated to the discussion of the minimization of phase and axial rf-excess micromotion, respectively. Here, atom loss due to elastic collisions is used as signal for optimization. In section 4.5 we describe the probing of micromotion via reactive collisions. Finally, in section 4.6 a summary is given and future prospects are addressed.

4.2 Ion trap and excess micromotion

In the following we consider micromotion in a linear Paul trap. Figure 4.1 shows the setup in our lab, which has been described in detail in [48, 49]. The four gray electrodes (e1-e4) are the rf-electrodes of the Paul trap. They are driven with a rf-frequency of $\Omega = 2\pi \times 4.2\,\mathrm{MHz}$ and generate the radial trapping confinement (i.e. within the $\hat{x}$-$\hat{y}$-plane) while the static field of two endcap electrodes (yellow) confines the ion in the axial direction ($\hat{z}$-direction). The effective distance from the trap center to the tips of the four rf-electrodes is $R_0 = 2.6\,\mathrm{mm}$, while the spacing between the two endcap electrodes is $2 \times Z_0 = 14\,\mathrm{mm}$. We nominally operate the ion trap in a symmetric manner. In a perfectly aligned linear Paul trap with vanishing rf-potentials on the endcaps such a symmetric rf-drive leads to a vanishing axial micromotion on the trap axis. The rf-electrode pair (e1, e2) is driven by a voltage $+V_0\cos(\Omega t)$ and the rf-electrode pair (e3, e4) by a voltage $-V_0\cos(\Omega t)$. The voltage amplitude[1] is $V_0 \approx 150\,\mathrm{V}$. At the center of the Paul trap this gives rise to the

[1] Measurements of the electrode voltages indicate, however, that the voltage amplitude V_0 for the electrode pair (e1, e2) and the pair (e3, e4) are not equal but 160 V and 143 V, respectively. Therefore, a cancellation of micromotion along the axial direction might be compromised. A simulation of the electrical fields for our setup can be found in [76].

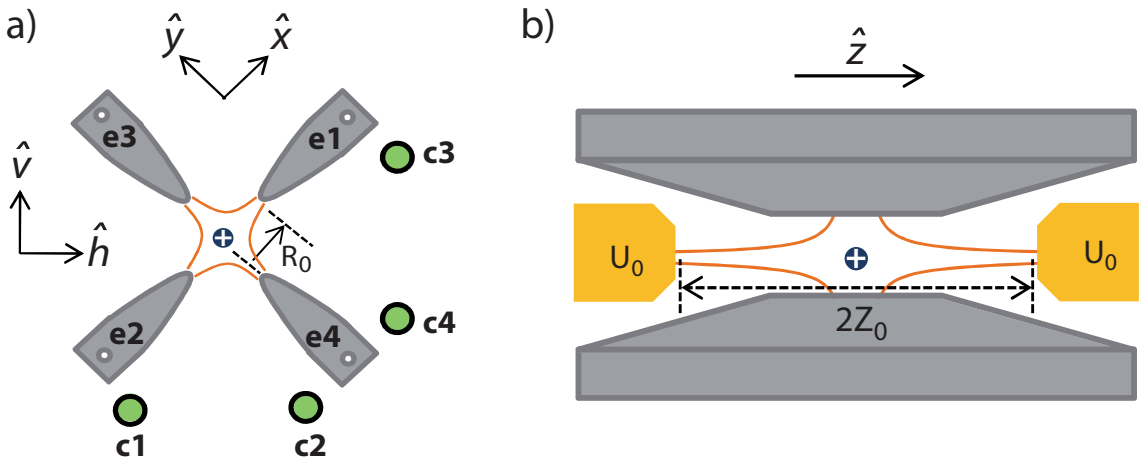

Figure 4.1: Schematic of the linear Paul trap. Shown is the configuration in the radial $\hat{x}$-$\hat{y}$-plane (**a**) and in the axial direction $\hat{z}$ (**b**). The rf-electrodes are indicated in gray, the endcap electrodes are yellow and the compensation electrodes (c1, c2, c3, c4) are green. For better visibility, the endcap electrodes are not depicted in **a** and the compensation electrodes are omitted in **b**. The orange lines illustrate some rf-electric field lines between the electrodes.

following electrical field

$$\begin{aligned}\vec{\mathcal{E}}(x,y,z,t) = &-\frac{2V_0}{R'^2}(x\hat{x}-y\hat{y})\cos(\Omega t)\\ &-\frac{\kappa U_0}{Z_0^2}(2z\hat{z}-x\hat{x}-y\hat{y})\,.\end{aligned} \tag{4.1}$$

We use $\{\hat{x},\hat{y},\hat{z}\}$ to denote the unit vectors for the directions of the coordinate system given in figure 4.1. The first term in equation (4.1) represents the electrical field generated by the rf-electrodes. Here, $R' \cong R_0$. The second term expresses the electrical field due to the endcap electrodes, which are held at constant electrostatic potential $U_0 = 7.6\,\mathrm{V}$, and $\kappa = 0.29$ is a geometrical factor for our setup. We work with single $^{138}\mathrm{Ba}^+$ ions at trapping frequencies (for the secular motion) of $\omega_{x,y,z} = 2\pi \times (131, 130, 38.8)$ kHz. The trap depth is about 2 eV. Before each measurement the ion is laser-cooled to the Doppler limit.

For the ideal case of equation (4.1), the particle is trapped exactly at the origin ($x = y = z = 0$) and exhibits vanishing micromotion. An additional quasi-constant stray electrical offset field with components in the transverse direction, however, shifts the ion to a different position where it experiences oscillating electrical fields and therefore undergoes micromotion. Applying the experimental technique that

we have demonstrated in Ref. [49] such an electrical stray field can be very well compensated to values smaller than $0.02\mathrm{Vm}^{-1}$ in our setup. This is the starting point for the measurements described in the present work. The kinetic energy contribution due to dc-stray electric fields is negligible as compared to the excess micromotion energies discussed in the remainder. In the following we simply assume the dc-stray fields to be fully compensated and we focus on excess micromotion resulting from phase delay and rf-fields in axial direction. A more general discussion can be found in appendix section A. Excess micromotion due to phase delay occurs when there is a relative phase φ_x between the oscillating voltages of the electrode pair (e1, e2) or a relative phase φ_y for the pair (e3, e4). Using the same approach as in Ref. [61], such phase differences give rise to additional oscillating electrical field terms. For $\varphi_{x_i} \ll 1$ ($x_i \in \{x, y\}$) these terms can be approximated by

$$\vec{\mathcal{E}}_{x_i} = V_0 \frac{\alpha_{x_i}\varphi_{x_i}}{2R_0} \sin(\Omega t)\hat{x}_i \equiv \mathcal{E}_{x_i,0} \sin(\Omega t)\hat{x}_i \,, \tag{4.2}$$

where the factors α_{x_i} depend on the trap geometry. We note that our configuration is characterized by $\alpha_{x_i} \approx 0.8$.

Rf-induced axial micromotion occurs when rf-electric fields are created along the trap axis, e.g. due to slight misalignment of the rf-electrodes or as a consequence of unwanted, asymmetric pick up of the rf-drive voltage on the endcap electrodes. This produces dominantly the electric field

$$\vec{\mathcal{E}}_z = \mathcal{E}_{z,0} \sin(\Omega t + \varphi_z)\ \hat{z} \,, \tag{4.3}$$

in the trap center, with unknown amplitude $\mathcal{E}_{z,0}$ and phase φ_z.

Excess micromotion readily increases the kinetic energy of the ion. This fact is also exploited for our detection scheme. The average kinetic energy is given by $E^{\mathrm{kin}} = m_{\mathrm{Ba}}\langle \dot{u}^2 \rangle/2$ (see also [61] and Appendix A for more detail), where m_{Ba} and $\dot{u}$ are the mass and the velocity of the Ba^+ ion, and $\langle\,\rangle$ represents the time average over a period of the secular motion at frequency Ω. The individual components of $\dot{u}$ are derived from the equations of motion. Using this approach, the kinetic energy contributions of motion in the three directions of space are given by

$$E^{\mathrm{kin}}_{x_i} = \frac{e^2\mathcal{E}^2_{x_i}}{4m_{\mathrm{Ba}}\Omega^2} \,, \tag{4.4}$$

where e is the elementary charge and $x_i \in \{x, y, z\}$.

The four green electrodes (c1-c4) in figure 4.1a are used to compensate the ac-

electric fields due to phase delay. We denote the pairs of compensation electrodes (c1, c2) and (c3, c4) as vertical (v) and horizontal (h) electrode pairs, respectively. Driving the vertical pair of compensation electrodes with the same ac-voltage will create an rf- electrical field at the position of the ion, which is pointing along the $\hat{\text{v}}$-direction. An ac-voltage applied at the horizontal pair of compensation electrodes produces an rf- electric field along $\hat{\text{h}}$. One of the endcaps is utilized to compensate ac-electric fields along the z-axis. Here, besides applying ac-voltages to compensation electrodes, one can also use alternative compensation methods. For example, phase delays can be implemented by adjusting cable lengths or by using additional capacitances similarly as in [77]. Besides excess micromotion arising from dc electrical stray fields and parasitic rf-fields, there is yet another kind of excess micromotion present in our setup. It is linked to elastic collisions of the ion with the cold atoms and has been predicted and investigated in [34, 54, 78, 79]. In simple terms its origin can be understood as follows: In a collision the ion can be pulled out from the center of the ideal Paul trap where no micromotion occurs to a location with non-vanishing electrical rf-fields and micromotion. Thus, even at negligible temperatures of the atom cloud the ion can acquire a non-vanishing average kinetic energy. The typical kinetic energy scale for collisional excess micromotion can be calculated. Using the approach of [78] for a 3D trap and taking our current trap parameters we obtain about $40\,\mu\text{K} \times k_\text{B}$ for a Ba^+ ion colliding with ultracold Rb atoms. Such collisional micromotion cannot be compensated. However, as it is a function of the atom-ion mass ratio and the general ion trap parameters, setups and configurations can be optimized to minimize it.

4.3 General method for minimizing excess micromotion using cold atoms

In order to minimize excess micromotion we generalize here the method we introduced in [49]. A single, cold Ba^+ ion in a Paul trap is immersed into an ultracold cloud of Rb atoms. In the cloud elastic and reactive atom-ion collisions take place with rates that depend on the micromotion energy. The experiments are done in two different atomic densities since for elastic collisions a relatively dilute cloud and for reactive collisions a dense atomic clouds are needed to be created. We find the minimum of micromotion by steering towards a local minimum (maximum) for the elastic (reactive) rate, respectively. Tuning of the micromotion is done via suitable electrical rf-fields at the center of the Paul trap which are produced by applying

rf-voltages on the compensation electrodes or on one of the endcap electrodes of the Paul trap.

The ultracold Rb atoms are held in a far-off-resonant, crossed optical-dipole trap at a wavelength of 1064 nm with a trap depth of about 22 $\mu\mathrm{K} \times k_\mathrm{B}$. The atomic temperature is about 700 nK. The atoms are spin-polarized in the hyperfine state $f = 1, m_f = -1$. We work with 1 to 3×10^4 ^{87}Rb atoms and shot-to-shot fluctuations of the atom number are typically on the level of a few percent.

Once it is immersed into an atomic cloud, a trapped ion undergoes elastic collisions with the atoms, which quickly leads to a non-thermal kinetic energy distribution of the ion. Because of its relevance for the developing field of cold atom-ion interactions [34, 71, 72], this issue has been recently investigated in a number of studies (e.g. [40, 54, 80–85]). The ionic energy distribution depends in a non-trivial way on quantities such as the atom-ion mass ratio, the atomic cloud size, and the ion trap parameters. In our case of Rb and Ba^+, the kinetic energy distribution of the ion is still nearly thermal, and the ion's average kinetic energy $E^{\mathrm{kin,a}}$ in the presence of atoms is given approximately by $5 \times E^{\mathrm{kin}}$, where E^{kin} represents the excess micromotion energy in the absence of atoms, see Appendix D. When we only compensate excess micromotion due to dc-electrical fields the remaining kinetic energy of the ion is about $E^{\mathrm{kin,a}} = 4\,\mathrm{mK} \times k_\mathrm{B}$ (see Appendices C and D) in our trap. This energy is partially due to phase delay and axial rf-fields.

4.4 Probing micromotion compensation via elastic atom-ion collisions

Here, we describe how we use elastic collisions between atoms and the ion to minimize rf-induced excess micromotion. As already discussed the typical kinetic energy of the ion in the atomic cloud is in the range of a few $\mathrm{mK} \times k_\mathrm{B}$ for our experiments. Thus, when the ion elastically collides with an ultracold atom it will typically kick the atom out of its shallow dipole trap. Alternatively, it only heats the atomic cloud at first, which finally also leads to atomic loss due to evaporation. In general, we expect the atomic loss to increase weakly with the average ion energy and therefore with the excess micromotion. The rate Γ_el for elastic binary collisions of an atom and an ion with reduced mass μ is given by [59]

$$\Gamma_\mathrm{el} = \sigma_\mathrm{el} n_\mathrm{at} \sqrt{2E_\mathrm{col}/\mu} \propto E_\mathrm{col}^{1/6}\,, \tag{4.5}$$

where n_{at} is the atomic particle density, σ_{el} is the atom-ion elastic scattering cross section given by equation(2.10) and E_{col} is the two-body collision energy of the particles in the center-of-mass reference frame.

In order to probe excess micromotion, we measure the loss rate of the atom number in the atomic cloud for various rf-voltages applied on the respective electrodes used for compensation.

Besides the elastic collisions between atom and ion also inelastic and reactive collisions can take place which disturb our minimization scheme. As it is discussed in chapter C, a typical reactive process is the three-body recombination of Ba^++Rb+Rb for which the reaction rate is given by $\Gamma_{\mathrm{inel}} = k_3 n_{\mathrm{at}}^2$ with $k_3 = 1.04 \times 10^{-24}\,\mathrm{cm^6 s^{-1}}$ for a three-body collisional energy of $2.2\,\mathrm{mK} \times k_{\mathrm{B}}$. Another reaction is charge exchange, $Ba^+ + Rb \rightarrow Ba + Rb^+$, with an energy independent rate $k_2 n_{\mathrm{at}}$, where $k_2 = 3.1 \times 10^{-13}\,\mathrm{cm^3 s^{-1}}$ In order to suppress three-body recombination we work with comparatively low densities n_{at} ranging from 2 to $4 \times 10^{11}\,\mathrm{cm^{-3}}$. This reduces the total reaction rate to about 0.3 Hz. Nevertheless, since for our experiments typical interaction times of up to 1 s are needed in order to gain enough atom loss due to elastic collisions, there is still a sizeable probability that the Ba^+ ion undergoes a reaction. We therefore use post-selection to only take into account runs where no reaction between the Ba^+ ion and an atom has occurred. For this, we determine via fluorescence imaging whether the Ba^+ ion is still present in the trap center immediately after the interaction time with the atom cloud. All runs for which this is not the case, are discarded.

4.4.1 Compensation of phase micromotion

Following equation (4.2) we compensate transverse phase micromotion by applying suitable voltages $V_{\mathrm{c,h}} \sin(\Omega t)$ and $V_{\mathrm{c,v}} \sin(\Omega t)$ to the compensation electrode pairs h and v. These rf-voltages are added on top of the dc compensation voltages. For this, we use a two-channel signal generator which is phase-locked to the rf-drive of the Paul trap.

Because we do not precisely know the phases of the rf-compensation voltages at the location of the respective electrodes we first carry out calibration measurements to determine these phases. We use the fact, that according to the trigonometric addition formulas a phase deviation of the compensation voltage, i.e. $\propto \sin(\Omega t + \phi)$ can be written as $\propto [\sin(\phi)\cos(\Omega t) + \cos(\phi)\sin(\Omega t)]$. The component $\propto \sin(\phi)\cos(\Omega t)$ leads to a position shift [see equation (4.1)] and the corresponding spatial displacement of the ion is proportional to $\sin(\phi)$. Instead of only a single phase ϕ, there

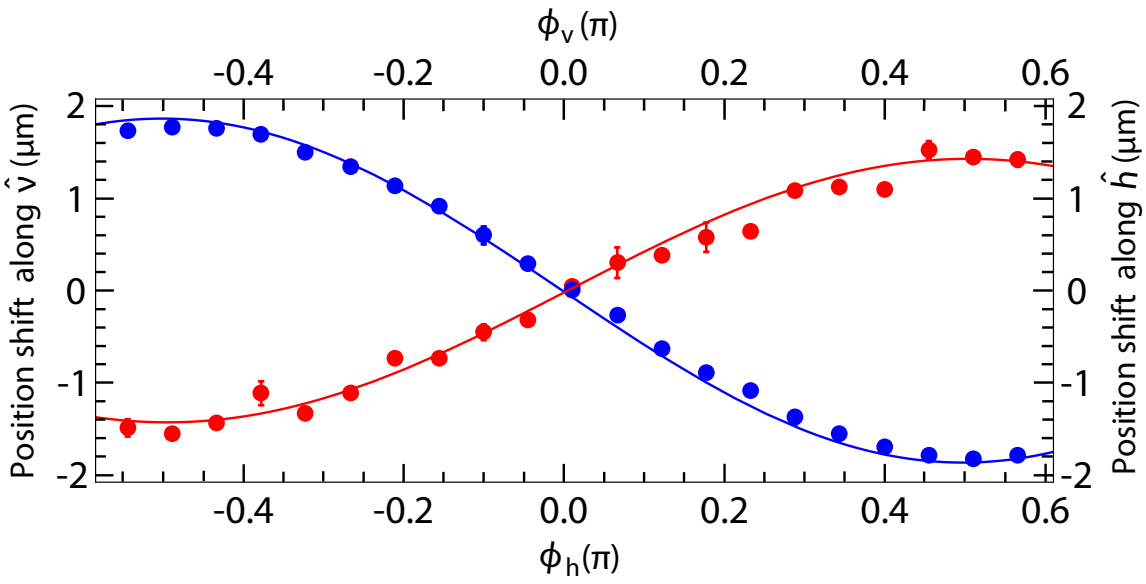

Figure 4.2: Measured position shifts of a Ba^+ ion along the directions $\hat{v}$ (blue filled circles) and $\hat{h}$ (red filled circles) (see figure 4.1a) as functions of the phases ϕ_h and ϕ_v, respectively. The solid lines are functions $\propto -\sin(\phi_h)$ (blue) and $\propto \sin(\phi_v)$ (red).

are two different phases ϕ_h and ϕ_v in our experiment, associated with the compensation electrode pairs h and v. A phase ϕ_h (ϕ_v) leads to a displacement in the $\hat{v}$ ($\hat{h}$) -direction, respectively. We carry out two measurements of the Ba^+ ion position (using fluorescence imaging) where we vary either ϕ_h or ϕ_v. Figure 4.2 shows the data. For simplicity, we have defined the phases ϕ_h and ϕ_v such that $\phi_v = 0$ and $\phi_h = 0$ correspond to a vanishing position shift. Both data sets were obtained using ac voltage amplitudes of $V_{c,v} = 10\,V$ ($V_{c,h} = 10\,V$), respectively, on the compensation rods, individually creating an electric field amplitude of $31\,Vm^{-1}$ at the trap center. In order to obtain larger position shifts of the ion, the voltage amplitude for the quadrupole blades was reduced by about a factor of 0.6. With these parameters the maximum position shifts are between 1 to $2\,\mu m$. The position shifts are detected via accumulating the scattered photons from the ion within $100\,\mu s$. We note that the line of view of the camera detecting the ion is perpendicular to the $\hat{v}$-direction but has an angle of about 45° with respect to the $\hat{h}$-direction. Therefore, the position shift along the $\hat{h}$-axis appears smaller than it is.

We now work with phases $\phi_h = 0$ and $\phi_v = 0$, and minimize phase micromotion. For this, we step through a range of ac voltage amplitudes $V_{c,v}$ and $V_{c,h}$ and search for a minimum in atomic loss. Figures 4.3a and b show the remaining atom numbers as a function of the field amplitudes $\varepsilon_{c,v} = V_{c,v} \times 3.1\,m^{-1}$ and $\varepsilon_{c,h} = V_{c,h} \times 3.1\,m^{-1}$,

respectively. For plot (a) we set $V_{\mathrm{c,h}} = 0$ while in (b) $V_{\mathrm{c,v}} = 0$ was used. The interaction time was 1 s. We change the sign of the electric field by flipping its phase by π at the rf-generator. On the top axis of the figures the electrical field amplitudes $\varepsilon_{\mathrm{c,h(v)}}$ are translated into the corresponding micromotion energies $E^{\mathrm{kin}}_{\mathrm{c,h(v)}}$ using equation (4.4).

As can be read off from figure 4.3a, an electric compensation field amplitude of $\varepsilon_{\mathrm{c,v}} \approx 4\,\mathrm{Vm}^{-1}$ reduces the micromotion energy by about $50\,\mu\mathrm{K} \times k_{\mathrm{B}}$. In contrast to that, figure 4.3b reveals that micromotion in the horizontal direction is already close to the minimum such that only small compensation fields $\varepsilon_{\mathrm{c,h}}$ are needed. In order to determine optimal electric field amplitudes for compensation more precisely, we heuristically use a cusp-like fit function $N_j = -\chi_j|\varepsilon_{\mathrm{c,j}} - \varepsilon^{\mathrm{max}}_{\mathrm{c,j}}| + N^{\mathrm{max}}_j$ with $j \in \{\mathrm{v,h}\}$ for the remaining atom numbers N_j. Here, χ_j, $\varepsilon^{\mathrm{max}}_{\mathrm{c,j}}$, and N^{max}_j represent fit parameters for the respective cusp. The given approach is simple and in general describes the data quite well. The cusp-like behavior was also observed in our previous measurements on the compensation of excess micromotion due to dc-stray fields [49]. Our fit results for the optimal amplitudes for the electric field compensation are $\varepsilon^{\mathrm{max}}_{\mathrm{c,v}} = 4.2 \pm 0.4\,\mathrm{Vm}^{-1}$ and $\varepsilon^{\mathrm{max}}_{\mathrm{c,h}} = 0.6 \pm 0.7\,\mathrm{Vm}^{-1}$, respectively. We note that although at these fields the atomic loss is minimized, it still remains at a level of about 15%, which is mainly due to other uncompensated excess micromotion. For comparison, the atom loss in the absence of an ion after a hold time of 1 s is only about 3%.

To check for consistency we carry out model calculations for the remaining number of atoms N as a function of micromotion energy. In our model we take into account atom loss due to elastic atom-ion collisions with a loss rate Γ_{el} [see equations (4.5) and (2.10)]. This elastic rate depends on the average two-body collision energy $E_{\mathrm{col}} = (1-\mu/m_{\mathrm{Rb}}) \times E^{\mathrm{kin,a}}$, where m_{Rb} is the mass of a ^{87}Rb atom. Here, $E^{\mathrm{kin,a}}$ is a function of the electrical field amplitudes $\varepsilon_{\mathrm{c,j}}$. We calculate $E^{\mathrm{kin,a}}$ using equation (4.4) and $E^{\mathrm{kin,a}}(\varepsilon_{\mathrm{c,j}} = 0) = 4\,\mathrm{mK} \times k_{\mathrm{B}}$. Furthermore, we include background atom loss with a rate of about $\Gamma_{\mathrm{bg}} = 500\,\mathrm{s}^{-1}$ in our model. The rate equation for the atom loss reads

$$\dot{N} = -\frac{\Gamma_{\mathrm{el}} + \Gamma_{\mathrm{bg}}}{N_0} N\,, \tag{4.6}$$

where N_0 is the initial atom number. This yields the solution

$$N(t) = N_0 \exp\left(-\frac{\Gamma_{\mathrm{el}} + \Gamma_{\mathrm{bg}}}{N_0} t\right)\,. \tag{4.7}$$

The red dashed lines in Figs. 4.3a and b show the results of our model calculations

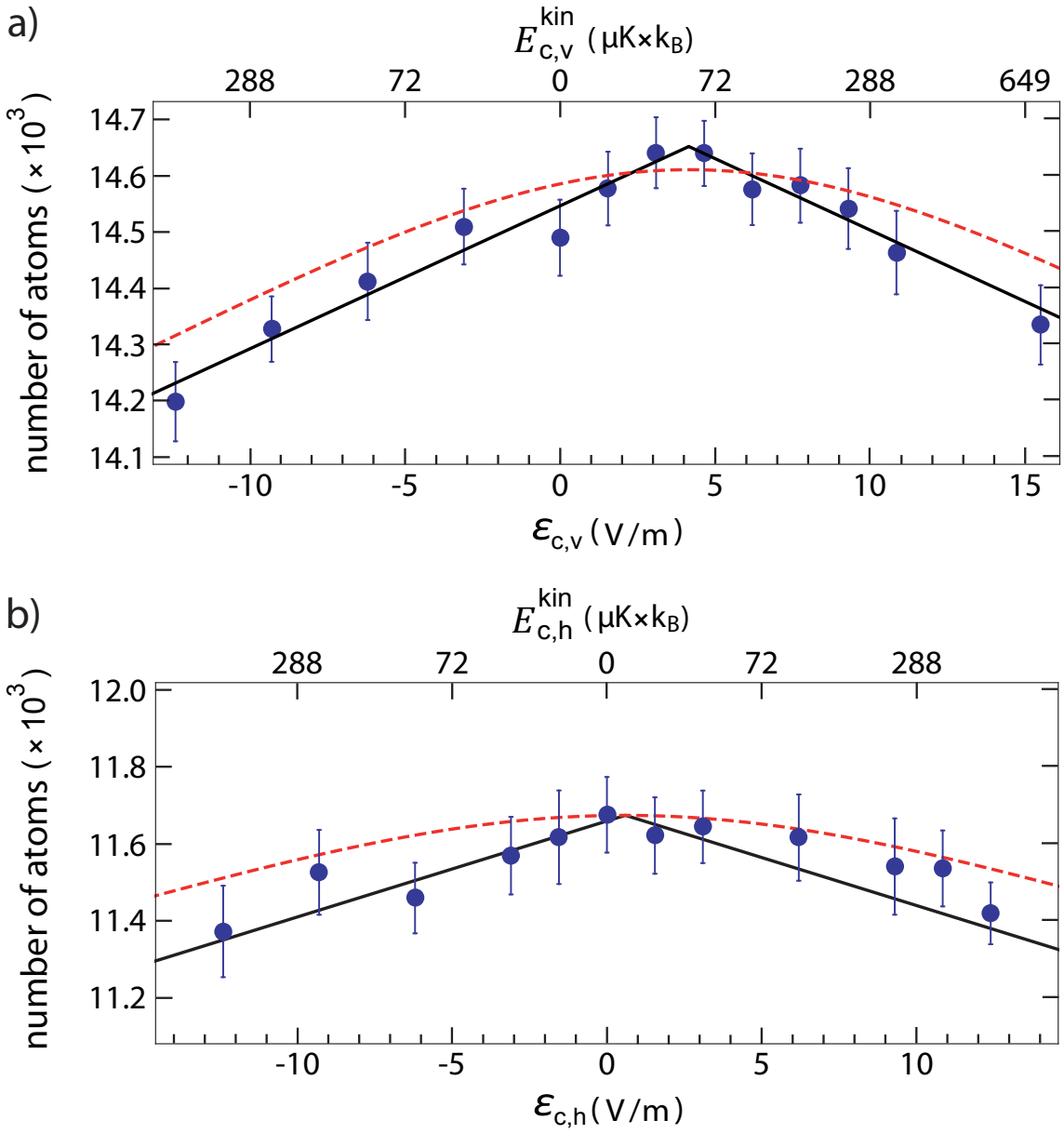

Figure 4.3: Remaining atom number after 1s of interaction with the ion as a function of the electric field amplitude $\varepsilon_{\mathrm{c,v}}$ (**a**) and $\varepsilon_{\mathrm{c,h}}$ (**b**), respectively. The upper horizontal axis translates the electric field amplitudes into the corresponding kinetic micromotion energies $E^{\mathrm{kin}}_{\mathrm{c,h(v)}}$ as determined by equation (4.4). Measurements are given by blue data points. Each of these data points is the average value of 170 experimental runs. The error bars represent the 1σ statistical uncertainty. Black solid lines are fits of the cusp function $N_j = -\chi_j|\varepsilon_{\mathrm{c,j}} - \varepsilon^{\mathrm{max}}_{\mathrm{c,j}}| + N^{\mathrm{max}}_j$ with $j \in \{\mathrm{v,h}\}$. The red dashed lines represent model calculations for the remaining number of atoms for the given experimental parameters and assuming elastic two-body atom-ion collisions [equation (4.7)]. In the model, also the background atom loss is taken into account (see text).

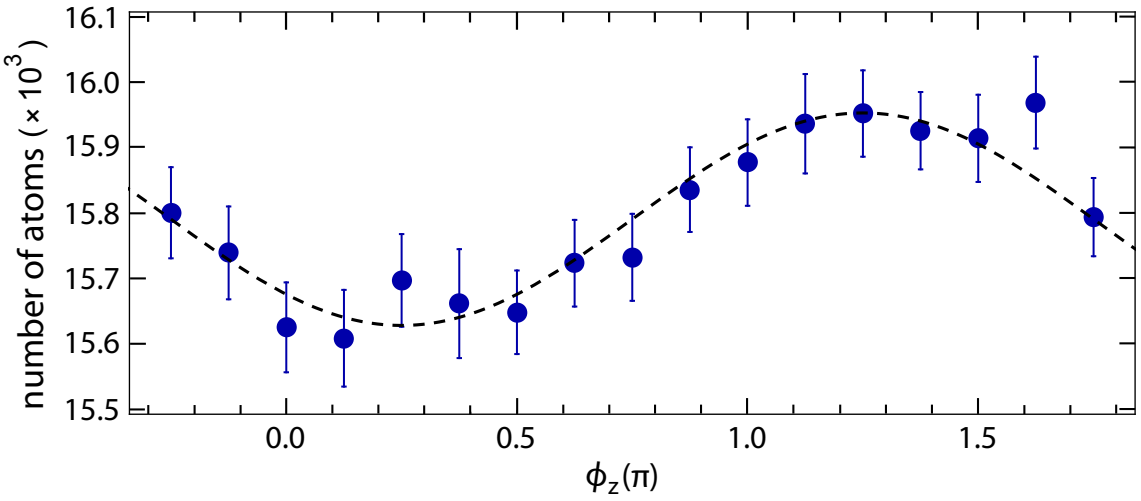

Figure 4.4: Remaining atom number after 500 ms of interaction time with the ion as a function of the phase ϕ_z of the ac-voltage applied on the endcap electrode. Blue dots are the measurements. The error bars indicate the 1σ statistical uncertainty. Each data point is the average value of 140 experimental runs. The dashed curve is a fit of a sine function, $\propto \sin(\phi_z + \Delta\phi_z)$, where $\Delta\phi_z = (-0.77 \pm 0.02)\pi$.

using equation (4.7). In order to ease the comparison between the theory curve and the experimental data, we scaled the initial atom number by a factor 0.98 for the calculations, which is, however, still well within the uncertainty of our atom number calibration. Figure 4.3 shows that after this scaling the agreement between our model calculations and the experimental data is reasonably good.

4.4.2 Compensation of rf-induced axial micromotion

In order to compensate for rf-induced axial excess micromotion, we apply [in accordance with equation (4.3)] an ac-voltage of $V_z = V_{0,z} \sin(\Omega t + \phi_z)$ to one of the endcap electrodes. We search for the optimal amplitude $V_{0,z}$ and phase ϕ_z, again using the scheme of minimizing atomic losses. For this we work with an atom cloud of 1.7×10^4 atoms and with an ion trap where phase micromotion is not compensated, i.e. $V_{\mathrm{c,v}} = V_{\mathrm{c,h}} = 0$. We start by optimizing ϕ_z. The voltage amplitude is set to a fixed value of $V_{0,z} = 1$ V which corresponds to an electric field amplitude of about $\varepsilon_{0,z} = 8\ \mathrm{Vm}^{-1}$ at the position of the ion in the trap center. Figure 4.4 shows the measured remaining number of atoms as a function of the phase ϕ_z for an interaction time of 500 ms with the ion. We can fit a sine function, $\propto \sin(\phi_z + \Delta\phi_z)$, to the data and obtain $\Delta\phi_z = (-0.77 \pm 0.02)\pi$. The atomic losses are minimal for

$\phi_z = -\Delta\phi_z + \pi/2$.

We fix this phase for the search of the optimal voltage amplitude $V_{0,z}$, which is carried out next. This time, we work with a configuration where phase micromotion is already compensated for as discussed in subsection 4.4.1. Now, initial atom densities of about $n_{\mathrm{at}} = 3.6 \times 10^{11}\,\mathrm{cm}^{-3}$ are used. Figure 4.5 shows the remaining atom number for an interaction time of 1 s as a function of the electric field amplitude $\varepsilon_{0,z} = V_{0,z} \times 8\,\mathrm{m}^{-1}$. As in figure 4.3, the top abscissa indicates the electric field amplitude in terms of a corresponding micromotion energy E_z^{kin} according to equation (4.4). To determine the optimum compensation voltage amplitude we fit the cusp function $-\chi|\varepsilon_{0,z} - \varepsilon_{0,z}^{\max}| + N^{\max}$ to the data (see solid lines in figure 4.5) and obtain $\varepsilon_{0,z}^{\max} = 10.4 \pm 0.5\ \mathrm{Vm}^{-1}$. This electric field amplitude corresponds to $V_{0,z} = 1.3 \pm 0.06$ V. Furthermore, the given value for $\varepsilon_{0,z}^{\max}$ corresponds to a decrease in micromotion energy of almost $300\,\mu\mathrm{K} \times k_{\mathrm{B}}$. This is about six times larger than the energy regarding phase micromotion, as discussed in subsection 4.4.1. Again, the red dashed line in figure 4.5 represents the result of model calculations using equation (4.7). Here, we take into account that phase micromotion was already compensated. As before, we applied a 0.98 scale factor to the initial atom number in the calculations. The agreement between the model calculations and the experimental data is again quite good.

4.5 Probing micromotion compensation via reactive atom-ion collisions

We now probe micromotion via reactive collisions instead of elastic ones. For this, we work with large atomic densities of about $n_{\mathrm{at}} = 7 \times 10^{13}\,\mathrm{cm}^{-3}$ where three-body recombination, $\mathrm{Ba}^+ + \mathrm{Rb} + \mathrm{Rb} \rightarrow (\mathrm{BaRb})^+ + \mathrm{Rb}$, is by far the dominant reaction process (see chapter C for more detail). The three-body recombination rate is given by $k_3\, n_{\mathrm{at}}^2$ and the rate constant k_3 scales as (see Appendices C and D)

$$k_3 \propto \widetilde{E}_{\mathrm{col}}^{-3/4}. \tag{4.8}$$

Here, $\widetilde{E}_{\mathrm{col}}$ is the three-body collision energy in the center-of-mass frame. Since the kinetic energies of the atoms can be neglected as compared to the ion energy, the average three-body collision energy is given by

$$\widetilde{E}_{\mathrm{col}} = \left(1 - \frac{m_{\mathrm{Ba}}}{m_{\mathrm{Ba}} + 2m_{\mathrm{Rb}}}\right) E^{\mathrm{kin,a}} = 0.56 E^{\mathrm{kin,a}}. \tag{4.9}$$

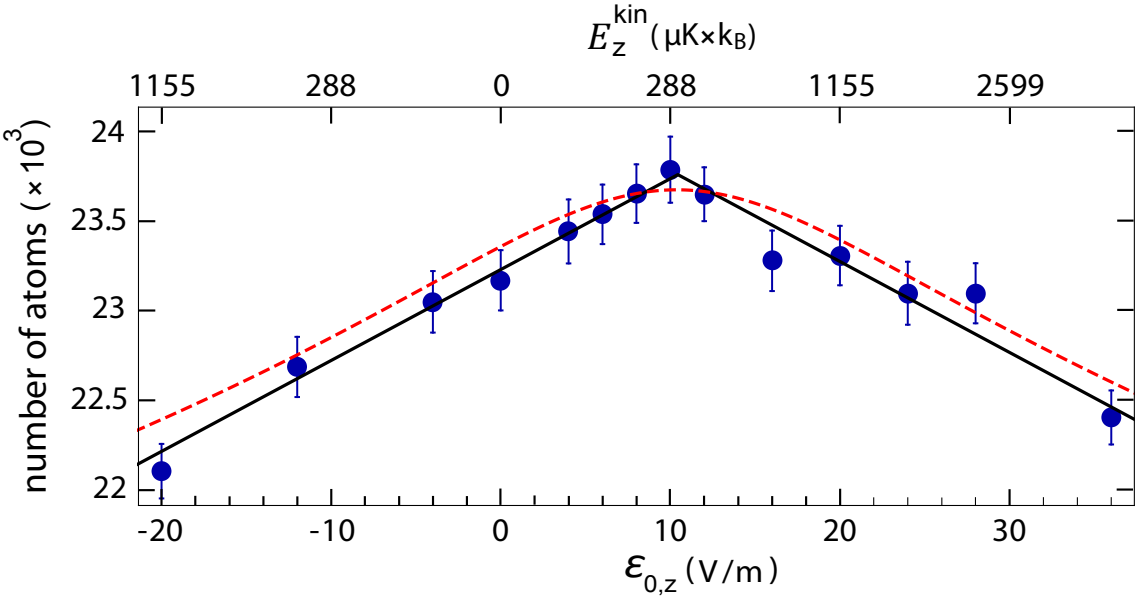

Figure 4.5: Remaining number of atoms after interaction with the ion as a function of the electric field amplitude $\varepsilon_{0,z}$. This field amplitude is produced at the position of the ion by applying an ac voltage to one of the endcap electrodes. Blue data points are measurements and the error bars represent the 1σ statistical uncertainty. The black solid line is a cusp function fit and the red dashed line shows the expected atom number obtained from model calculations.

As stated earlier at $\widetilde{E}_{\mathrm{col}} = 2.2\,\mathrm{mK} \times k_{\mathrm{B}}$ the rate constant is $k_3 = 1.04 \times 10^{-24}\,\mathrm{cm^6 s^{-1}}$. equation (4.8) shows that the reaction rate will strongly scale with the micromotion energy of the ion. We measure the reaction rate as follows. The ion is immersed into the atomic cloud for a variable time t. Afterwards, we use near-resonant fluorescence imaging for a duration of 100 ms to detect the ion. If no cold Ba^+ ion is detected, we infer that a reaction has occurred. After repeating the experiment 90 times we obtain a probability that a reaction has taken place within a given time t. Figure 4.6 shows the probability $P_{\mathrm{Ba^+}}$ that the Ba^+ ion has not reacted as a function of t. The open purple circles correspond to a measurement without compensation of phase and of rf-induced axial excess micromotion. In contrast, the filled blue circles represent a measurement where we have compensated micromotion, as described in sections 4.4.1 and 4.4.2. The inelastic rate clearly increases when micromotion is compensated, as expected.

The decays can be well fit by exponentials $P_{\mathrm{Ba^+}} = \exp(-\Gamma_{\mathrm{inel}} t)$, where $\Gamma_{\mathrm{inel}}^{\mathrm{w}} = (8.0 \pm 0.6) \times 10^3\,\mathrm{s^{-1}}$ and $\Gamma_{\mathrm{inel}}^{\mathrm{wo}} = (5.2 \pm 0.3) \times 10^3\,\mathrm{s^{-1}}$ for the case with (w) and without

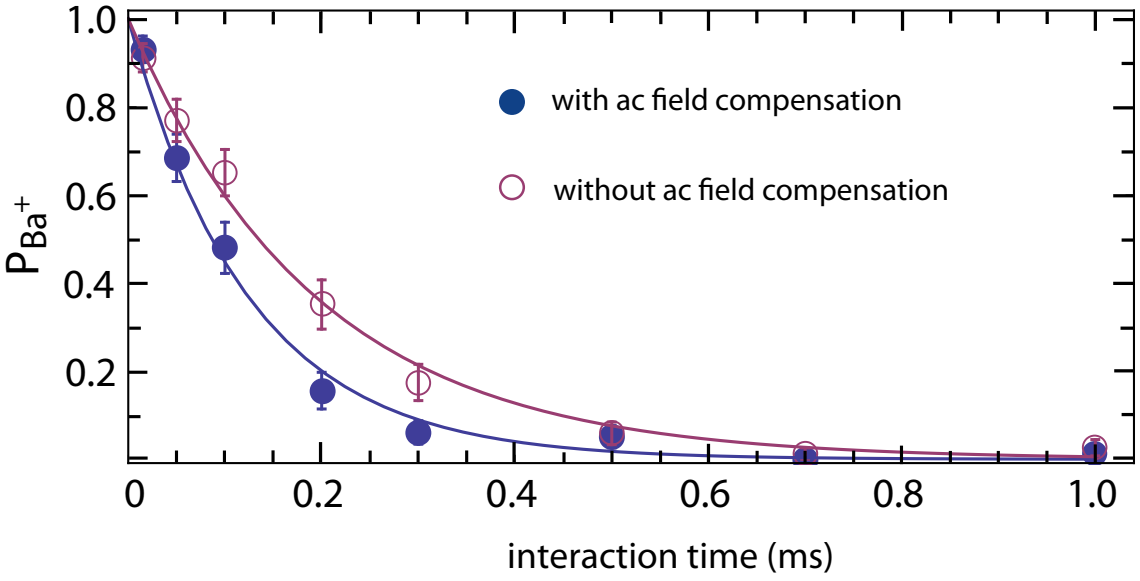

Figure 4.6: Effect of micromotion compensation for three-body recombination. Shown is the probability P_{Ba^+} that a Ba^+ ion has not reacted away after being immersed into an ultracold cloud of atoms for an interaction time t. The purple empty circles (blue filled circles) are measurements carried out without (with) applying the micromotion compensation. The error bars give the 1σ statistical uncertainty. The continuous lines are exponential fits.

(wo) micromotion compensation, respectively. Using equation (4.8) we obtain

$$\frac{\widetilde{E}^{\mathrm{w}}_{\mathrm{col}}}{\widetilde{E}^{\mathrm{wo}}_{\mathrm{col}}} = \left(\frac{\Gamma^{\mathrm{wo}}_{\mathrm{inel}}}{\Gamma^{\mathrm{w}}_{\mathrm{inel}}}\right)^{4/3} = 0.56 \pm 0.07\,. \tag{4.10}$$

Therefore, the compensation of phase and rf-induced axial micromotion in our setup reduces the original kinetic energy $E^{\mathrm{kin,a}}_{\mathrm{wo}}$ of the ion by about $0.44E^{\mathrm{kin,a}}_{\mathrm{wo}}$.

In sections 4.4.1 and 4.4.2 we have determined that this reduction of excess micromotion energy is 350 $\mu\mathrm{K} \times k_{\mathrm{B}}$, which corresponds to a decrease of $\Delta E^{\mathrm{kin,a}} = 5 \times 350\ \mu\mathrm{K} \times k_{\mathrm{B}} = 1.75\ \mathrm{mK} \times k_{\mathrm{B}}$. Since $0.44E^{\mathrm{kin,a}}_{\mathrm{wo}} = 1.75\ \mathrm{mK} \times k_{\mathrm{B}}$, we obtain $E^{\mathrm{kin,a}}_{\mathrm{wo}} \approx 4\,\mathrm{mK} \times k_B$. This is in agreement with the value stated in section 4.4.1. The given comparison demonstrates the good consistency between the two methods.

The remaining kinetic energy $E^{\mathrm{kin,a}}$ of about $2.2\ \mathrm{mK} \times k_{\mathrm{B}}$ after compensation in our setup is still substantial. It can probably only partially be explained by collisionally induced micromotion for which the typical energy scale is expected to be on the order of $40\ \mu\mathrm{K} \times k_{\mathrm{B}}$ for our trap parameters [78]. We are planning to investigate this in detail in the near future.

4.6 Summary and Discussion

In conclusion, we demonstrate how to compensate rf-excess micromotion by studying elastic or reactive collisions of an ion with ultracold neutral atoms. We minimize unwanted rf-electrical fields down to the level of about $1\,\mathrm{Vm}^{-1}$, which is of similar quality as achieved via other conventional compensation schemes [50–54]. In our setup the compensation decreased the ionic excess micromotion energy by about $350\,\mu\mathrm{K} \times k_\mathrm{B}$. Furthermore, we deduce from known scaling laws of collision rates that the ion after full dc- and rf-field compensation still has a substantial amount of kinetic energy of about $2.2\,\mathrm{mK} \times k_\mathrm{B}$ when located inside the cold atomic gas. This residual kinetic energy might be partially explained by collision-induced micromotion. In the future it will be interesting to investigate this fundamental limit in more detail, e.g. by varying trap parameters of the Paul trap such as the q and a parameters. Due to characteristic scaling properties of the relevant energy terms with q and a this will allow for discriminating between different sources of micromotion [49].

The method discussed here is especially convenient for atom-ion hybrid systems since both species are readily available. Compensating excess micromotion allows for reaching low collisional energies between atom and ion. This could be of interest e.g. in the search for shape resonances in atom-ion collisions, see e.g. [86]. Finally, it has been predicted [78] that the s-wave collisional regime can be reached for large atom-ion mass ratios, e.g. as for Yb^++Li [87], since here micromotion-induced heating is comparatively small. For further suppressing micromotion-induced heating, Rydberg dressing of atoms [79] could be applied.

Chapter 5

Life and death of a cold $BaRb^+$ molecule inside an ultracold cloud of Rb atoms

"Life and death of a cold $BaRb^+$ molecule inside an ultracold cloud of Rb atoms"

Amir Mohammadi, Artjom Krükow, Amir Mahdian, Markus Deiß, Jesús Pérez-Ríos, Humberto da Silva Jr., Maurice Raoult, Olivier Dulieu, and Johannes Hecker Denschlag,

arxiv **2005.09338** (2020)

Abstract

We study the evolution of a single $BaRb^+$ molecule while it continuously collides with ultracold Rb atoms. The initially weakly-bound molecule can undergo a sequence of elastic, inelastic, reactive, and radiative processes. We investigate these processes by developing methods for discriminating between different ion species, electronic states, and kinetic ion energy ranges. By comparing the measurements to model calculations we obtain a consistent description of the typical trajectory of the ion through the manifold of available atomic and molecular states. As a further result, we determine rates for collisional and radiative relaxation as well as photodissociation, spin-flip collisions, and chemical reactions.

5.1 Introduction

In recent years, methods have been developed to produce ultracold molecules out of ultracold atoms, e.g. by photoassociation [88–90], sweeping over a Feshbach resonance [91, 92], radiative association in a two-body collision (e.g. [86, 93]), or three-body recombination [94]. Typically, the resulting cold molecules are internally highly-excited and very reactive. Therefore, several questions arise. What are the reaction and relaxation paths that the particles take while they are exposed to light fields and collisions? What are the dynamics?

Investigations on these topics can be conveniently performed in hybrid-atom-ion systems where trapped, cold molecular ions are immersed in a trapped gas of ultracold atoms [34, 71, 72, 95–98]. Ion traps can be very deep so that an ion is still trapped even if large amounts of energy are released in an inelastic or reactive process. Furthermore, it is possible to selectively detect ionic products on the single particle level. Control over the locations of the traps allows for deterministically starting or stopping collisional dynamics between atoms and ion. In addition, low temperatures in the mK regime and below enable a high level of control for the preparation of the initial quantum state of the reactants and of the collision parameters such as the collision energy. A specific property of ion-neutral collisions is the long-range interaction between a charge and an induced dipole, which depends on the interatomic distance as $1/R^4$ [34, 71]. The combination of long-range interaction and low temperature corresponds to an interesting regime where reactions and inelastic processes can already take place at comparatively large inter-particle distances (see, e.g., [99]). This leads to large cross sections and promotes the formation

of weakly-bound molecular states.

The young field of cold hybrid-atom-ion systems has shown tremendous progress studying inelastic collisions and reactions. This includes charge exchange between atoms and atomic ions [40, 100–105], and spin flips [106, 107]. It was possible to observe collisionally induced vibrational or rotational relaxation of a deeply bound molecular ion [16, 108], which is a collision at short internuclear distances. Furthermore, the formation of cold molecular ions from cold neutral and electrically charged atoms has been realized for several species (e.g., [93,109–111]), and reactive behavior of molecular ions has been investigated [112–115].

Here we take a different approach, focussing less on a single, particular physical or chemical process. Instead we study the progression and interplay of the elastic, inelastic and reactive processes which take place. Concretely, we investigate, both experimentally and theoretically, the evolution of a cold, weakly-bound $BaRb^+$ molecular ion as it continuously collides with ultracold Rb atoms. These collisions can be elastic, inelastic, or reactive. Our investigation includes the deterministic birth of the molecular ion inside the atom cloud, its typical life undergoing changes in the electronic and vibrational states, and its death as it reacts away. We find that the evolution of the $BaRb^+$ ion directly after its formation is mainly dominated by vibrational relaxation collisions with Rb atoms at large internuclear distance. With increasing binding energy, radiative processes become progressively important until they are dominant. We observe Ba^+, Rb_2^+ and Rb^+ ions as reaction products, resulting from a range of photo- or collisionally-induced processes which are discussed in detail. Interestingly, in the experiments of Ref. [110] where the formation of $BaRb^+$ molecules from cold Ba^+ ions and Rb atoms was studied, also Rb^+ and Rb_2^+ as final products were detected. How these products came about, however, remained unclear. The results of our work, presented here, may be a key to also explain these findings.

This chapter is organized as follows. In sections 5.2 to 5.9, we study the elastic, inelastic and reactive processes of the $BaRb^+$ ion for different phases of its evolution. A detailed discussion of experimental parameters and detection methods is provided in sections B1 to B3 of the Appendix. Finally, in sections B4 and B5 of the Appendix we give additional infromation on the theoretical models, calculations, and Monte-Carlo (MC) simulations.

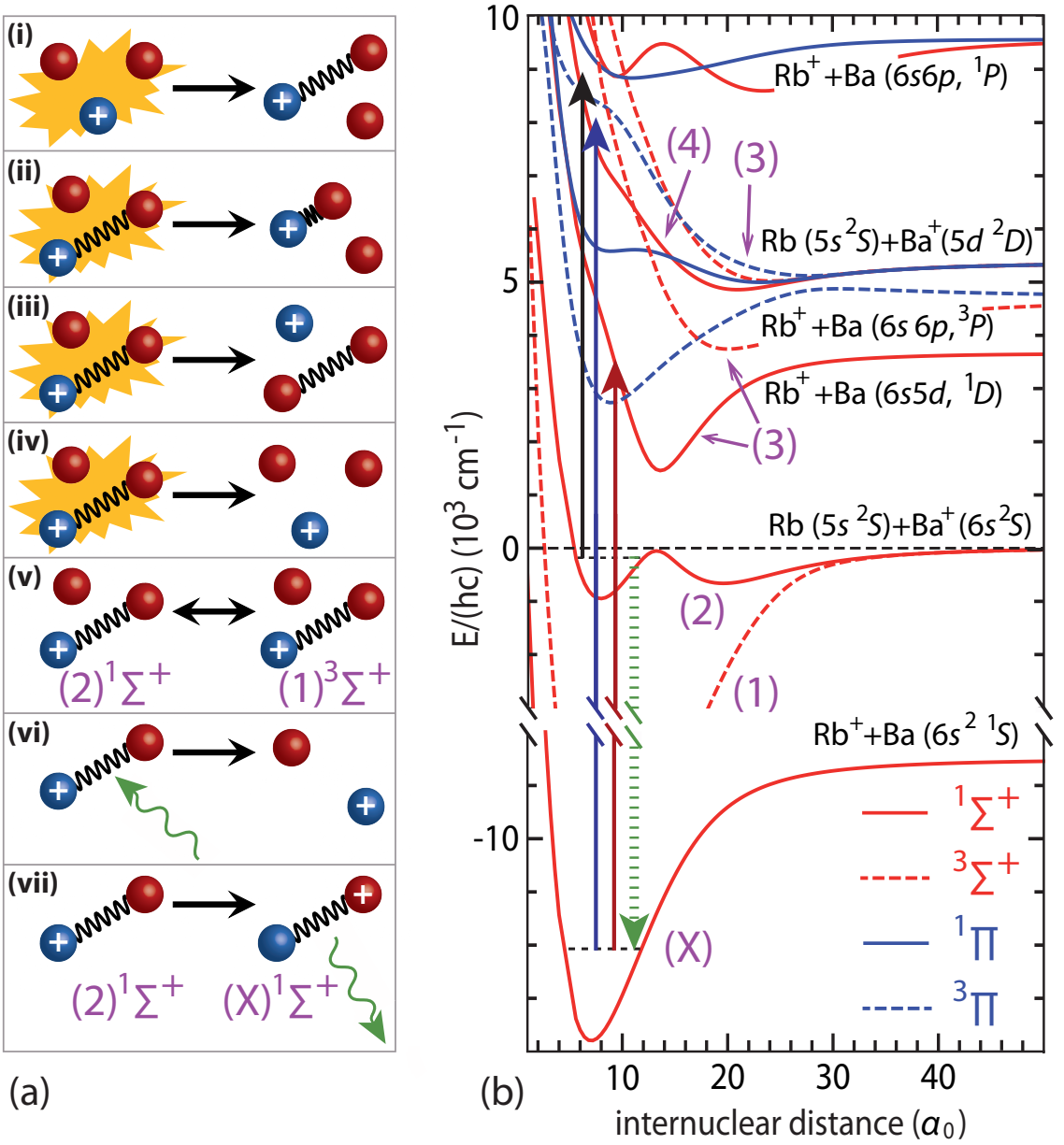

Figure 5.1: (a) Illustration of various inelastic and reactive processes. (i) Formation of a $BaRb^+$ molecule via three-body recombination, (ii) collisional relaxation of a $BaRb^+$, (iii) substitution reaction, (iv) collisional dissociation, (v) collisional spin exchange, (vi) photodissociation, and (vii) radiative relaxation. (b) PECs for $BaRb^+$, taken from [110]. The entrance channel $Rb(5s\,^2S) + Ba^+(6s\,^2S)$ marks zero energy. Solid black, blue, and red arrows show possible photodissociation transitions for 1064 nm, 493 nm, and 650 nm light, respectively. The dashed green arrow indicates radiative relaxation to the electronic ground state.

5.2 Experimental setup and production of molecular ion

Our experiments are carried out in a hybrid atom-ion apparatus. The basic setup is described in detail in [48]. For the investigations presented here, we produce a single $BaRb^+$ molecule which is trapped in a linear Paul trap with trap frequencies of $2\pi \times (80,\ 30)$ kHz in radial and axial direction, respectively. The $BaRb^+$ ion is in contact with a cloud of 6×10^6 ultracold ^{87}Rb atoms with a temperature of $T = 750$ nK. The atoms are prepared in the electronic ground state $5S_{1/2}$ and are spin-polarized, having a total angular momentum $F = 1$ and $m_F = -1$. The atomic cloud is held in a far off-resonant crossed optical dipole trap (ODT) at 1064 nm with a trap depth of approximately $20\,\mu\mathrm{K} \times \mathrm{k_B}$, where k_B is the Boltzmann constant. The density distribution of the cigar-shaped cloud can be described by a Gaussian with root mean square widths of 9 and 60 μm in radial and axial direction, respectively (see Appendix B1).

Initially, the cold $BaRb^+$ molecule is produced via three-body recombination $Ba^+ + Rb + Rb \rightarrow BaRb^+ + Rb$, typically at large internuclear distances, see Appendices C and D for more detail, and see (i) in figure 5.1(a). For this, we prepare in the Paul trap a single, laser-cooled $^{138}Ba^+$ ion in the electronic ground state $6S_{1/2}$, and a dense Rb atom cloud in the ODT. At that time the two traps are separated by about 100 μm. Right before we start our experiments with the single Ba^+ ion we remove unwanted Rb^+ and Rb_2^+ ions, which can form spontaneously in our trapped atom cloud, with a mass-filter scheme, see Appendix B2. After this purification step the 493 nm and 650 nm laser-cooling beams for the Ba^+ ion are switched off and the Ba^+ ion is moved into the atom cloud center. This is done within 100 μs by abruptly changing the voltage on one of the endcap electrodes of the Paul trap by 1.5 V.

Once the Ba^+ ion is in the atom cloud the $Ba^+ + Rb + Rb \rightarrow BaRb^+ + Rb$ three-body recombination leads to the formation of $BaRb^+$ molecules with a rate $\Gamma_\mathrm{tbr} = k_3 n(t)^2$, where $k_3 = 1.04(4) \times 10^{-24}\,\mathrm{cm^6 s^{-1}}$ is the three-body rate constant (see Appendix C), and $n(t)$ is the density of the atom cloud at a given time t at the ion trap center. For the central atomic density of $8.1 \times 10^{13}\mathrm{cm^{-3}}$ we obtain $\Gamma_\mathrm{tbr} \approx 6.8 \times 10^3\ \mathrm{s^{-1}}$. Three-body recombination is by orders of magnitude the leading reaction process of the Ba^+ ion, and $BaRb^+$ is the main product, as it is discussed in Appendices C and D. Initially, the $BaRb^+$ molecule is weakly-bound below the atomic $\mathrm{Rb}(5s\,^2S) + \mathrm{Ba}^+(6s\,^2S)$ asymptote [see figure 5.1(b)]. Its binding energy is expected to be $\sim 2\mathrm{mK} \times k_\mathrm{B}$ corresponding to the typical atom-ion collision

energy in our Paul trap, see Appendices C and D. Furthermore, according to simple statistical arguments, we expect the $BaRb^+$ molecular ion to be produced in the singlet state $(2)^1\Sigma^+$ and triplet state $(1)^3\Sigma^+$ with a probability of 25% and 75%, respectively. For both of them the initial binding energy of $\sim 2\text{mK} \times k_\text{B}$ corresponds to a vibrational state $v = -5$ (see also figure B1 of Appendix B4.1). The negative vibrational quantum number v indicates that it is counted downwards from the atomic asymptote, starting with $v = -1$ for the most weakly bound vibrational state. When v has a positive value, it is counted upwards from the most deeply bound vibrational state $v = 0$.

5.3 Experimental Investigation of the evolution of the molecular ion

As will become clear later, we can learn a lot about the evolution of the $BaRb^+$ molecule by monitoring the presence of the Ba^+ ion and its state in the trap. Figure 5.2(a) shows data for the measured probability P_{Ba^+} for detecting a Ba^+ ion as a function of time for four different experiments. After immersing the cold Ba^+ ion into the cloud for a variable time τ we quickly (within 20 μs) pull out the remaining ion and take two fluorescence images (see Appendix B3.1 for details). For the first image the imaging parameters are chosen such, that only a cold Ba^+ ion with a temperature of about 100 mK or below can be detected. The filled blue circles in figure 5.2(a) show these measurements for various immersion times τ. We essentially observe here the three-body recombination of Ba^+ towards $BaRb^+$. Next, we take a second fluorescence image which is preceded by a long laser cooling stage (for details see Appendix B3.1). This retrieves almost 60% of the Ba^+ ions that had reacted away [filled red circles in figure 5.2(a)]. We can explain this retrieval by the following scenario. There is a sizable probability for a freshly formed $BaRb^+$ molecular ion to break up via photodissociation. The break up produces a hot Ba^+ ion which is subsequently cooled down to below ≈ 100 mK by the long laser cooling stage so that it can be detected by fluorescence imaging (see Appendix B3.1). Photodissociation can occur, e.g., by the ODT laser at 1064 nm. Figure 5.1(b) shows indeed that 1064 nm photons can excite weakly-bound $BaRb^+$ ions below the $\text{Rb}(5s\,^2S) + \text{Ba}^+(6s\,^2S)$ asymptote to repulsive potential energy curves (PECs). The most relevant transitions to produce a hot Ba^+ ion are $(2)^1\Sigma^+ \rightarrow (4)^1\Sigma^+$ and $(1)^3\Sigma^+ \rightarrow (3)^3\Pi$. After the excitation, the Ba^+ ion and the Rb atom are accelerated away from each other, following the repulsive molecular potential. The Ba^+ ion will

obtain a high kinetic energy of up to 0.2 eV. As a consequence, it will afterwards orbit most of the time outside the atom cloud, having a small probability for collisions with Rb atoms. Therefore, sympathetic cooling and three-body recombination are strongly suppressed and the hot Ba^+ ion remains hot until it is cooled down during the long laser cooling stage. We have direct evidence for this photodissociation process, since we detect a fraction of the Ba^+ ions in the electronically excited $5D_{5/2}$ state which corresponds to one of the asymptotic states of the $(4)^1\Sigma^+$ and $(3)^3\Pi$ potentials [see figure 5.1(b)]. Concretely, we find that about half of the retrieved hot Ba^+ ions populate the metastable $5D_{5/2}$ state with its natural lifetime of $\sim$ 30 s. As the $Rb(5s) + Ba^+(5d\,D_{3/2,5/2})$ asymptotes are located more than 5000 cm^{-1} above the initially formed $BaRb^+$ molecular states, they only can be reached by photodissocation. We discriminate the population of the Ba^+ $5D_{5/2}$ state from the population in the other Ba^+ states by using the fact, that a Ba^+ ion in state $5D_{5/2}$ can only be laser-cooled and detected after pumping it out of this metastable level with a 614 nm laser. Thus, when we switch off the 614 nm laser we lose the signal from the metastable $5D_{5/2}$ Ba^+ ion.

To double check whether it is really the 1064 nm ODT laser which is responsible for photodissociation we carry out a second set of measurements, where the ODT is turned off 250 μs before the Ba^+ ion is immersed into the cold atom cloud. As a consequence the atomic cloud is now free falling and ballistically expanding. The calculated time evolution of the atomic density at the center of the ion trap is shown in figure 5.2(b) (see also Appendix B1). When we detect cold Ba^+ ions via fluorescence imaging [hollow blue circles in figure 5.2(a)] there is essentially no change in signal as compared to the case with the ODT being on. This is expected since the atomic density is nearly constant on the time scale of the three-body recombination. However, the signal solely for the hot Ba^+ ion, which is obtained by subtracting the signal for cold Ba^+ from the signal for both cold+hot Ba^+, is significantly smaller compared to when the ODT laser is on. Thus, this indeed shows that 1064 nm light photodissociates $BaRb^+$ molecules into hot Ba^+ ions and Rb atoms. Nevertheless, the signal for the hot Ba^+ ion is still on the order of 10% for sufficiently large times τ. Therefore, also light with a different wavelength than 1064 nm must contribute to the production of hot Ba^+ ions. As we will show in section 5.8 the remaining signal for hot Ba^+ can be explained due to photodissociation of ground state $(X)^1\Sigma^+$ molecules via the laser cooling light at 493 nm.

We note that photodissociation by 1064 nm light can also produce a hot Rb^+ ion, instead of a hot Ba^+ ion. This occurs in the transition $(1)^3\Sigma^+ \rightarrow (3)^3\Sigma^+$. So far, we

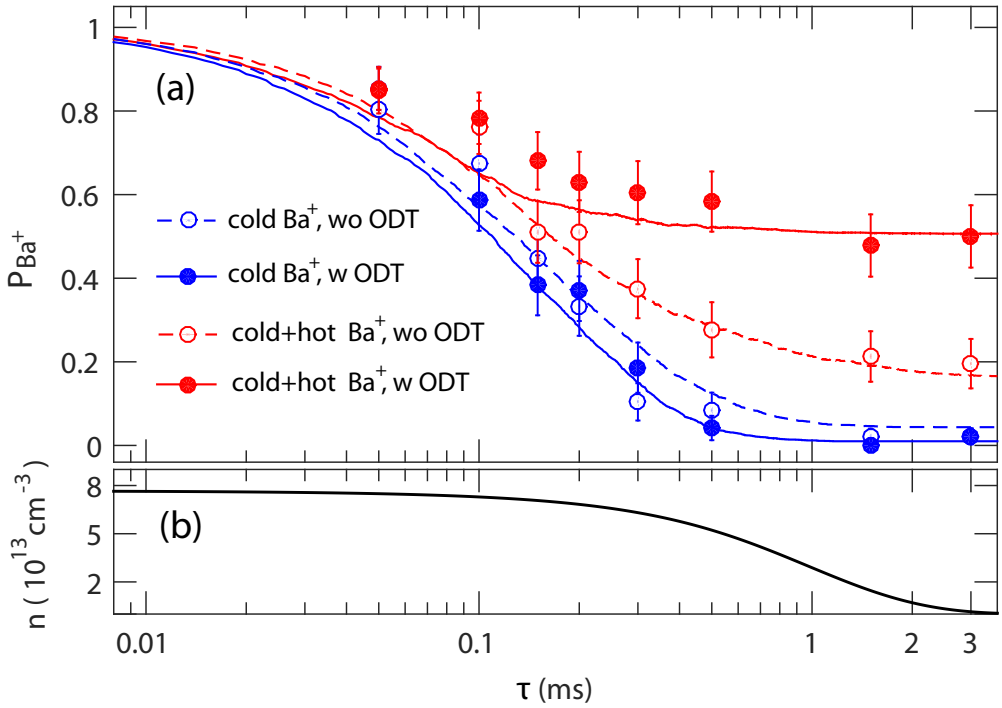

Figure 5.2: (a) Probability P_{Ba^+} of detecting a Ba^+ ion as a function of time τ after immersion into a Rb atomic cloud. Circles are measured data. Each data point is the mean value of 50 repetitions of the experiment and the error bars represent the 1σ statistical uncertainty. Curves are the results of MC simulations (see Appendix B5). (b) Time evolution of the atomic density n at the ion trap center after the ODT beams have been switched off at $\tau = -250\,\mu$s.

have not experimentally studied this process in detail.

5.4 Insights from calculations

We now combine the information from our experimental data with insights from theoretical calculations. This sets strong constraints on possible scenarios for the evolution of the BaRb^+ molecule and essentially fixes all free parameters of our theoretical model. Our analysis mainly involves electronic and vibrational states, while rotational and hyperfine degrees of freedom are not taken into account to a large part.

For example, we have carried out calculations for photodissociation cross sections which are based on computed PECs and transition dipole moments for highly-excited electronic states [86, 110] (for details see Appendix B4.3). In the calculations we find that the photodissociation cross section for the $v = -5$ BaRb^+ molecule with

1064 nm light is about two orders of magnitude too small to explain the hot Ba^+ signal. However, the calculations also show that the photodissociation cross section increases approximately as $\propto E_b^{0.75}$ for both singlet $(2)^1\Sigma^+$ and triplet $(1)^3\Sigma^+$ $BaRb^+$ molecules, where E_b is the binding energy (see figure B4 of Appendix B4.3). Apparently, shortly after production, while it is still immersed in the Rb cloud, the weakly-bound $BaRb^+$ molecule must vibrationally relax by a number of vibrational levels before it is photodissociated. A theoretical treatment shows that the vibrational relaxation is due to inelastic atom-molecule collisions, for which we have derived cross sections in Appendix B4.1 via quasi-classical trajectory (QCT) calculations. Furthermore, our calculations predict that while photodissociation of singlet $(2)^1\Sigma^+$ molecules via the 1064 nm laser indeed dominantly produces hot Ba^+ ions, photodissociation of triplet $(1)^3\Sigma^+$ molecules mainly leads to hot Rb^+ ions. Thus, in order to explain the measured substantial percentage of hot Ba^+ ions, there has to be a mechanism which converts triplet molecules into singlet molecules. This spin-flip mechanism is provided by inelastic atom-molecule collisions, for which the cross section is estimated to be a fraction of the Langevin cross section (see Appendix B4.2). Finally, our theoretical treatment reveals that radiative relaxation of the $(2)^1\Sigma^+$ molecules towards the electronic ground state $(X)^1\Sigma^+$ due to spontaneous emission [as illustrated by the green downward arrow in figure 5.1(b)] needs to be taken into account. According to our calculations we obtain a broad population distribution of final vibrational levels in the ground state, ranging from about $v = 10$ to above $v = 200$, with a peak at $v = 55$, see figure B8 in Appendix B4.3. For a relaxation towards the $v = 55$ level a photon at a wavelength of about 850 nm is emitted. The relaxation rate is predicted to scale as $\propto E_b^{0.75}$, which is the same power law as for photodissociation, see figure B7 in Appendix B4.3. Hence, there is a constant competition between photodissociation and radiative relaxation for the singlet state $(2)^1\Sigma^+$. Once in the ground state the molecule is immune to photodissociation by 1064 nm light, because the photon energy is not sufficient. Photodissociation via laser cooling light, however, is possible.

We note that triplet $(1)^3\Sigma^+$ molecules cannot radiatively relax to $(X)^1\Sigma^+$ according to the selection rules for electric dipole transitions. Therefore, in the absence of any collisional or light-induced processes, these molecules remain within the triplet state $(1)^3\Sigma^+$.

Besides the already mentioned inelastic and reactive processes also collisional dissociation, substitution reactions and elastic collisions play a role for the evolution of the $BaRb^+$ molecule. In order to theoretically model the evolution of the

$BaRb^+$ molecular ion in the atom cloud we carry out MC simulations and compare them to the measured data. In the simulations we take into account the most relevant processes shown in figure 5.1(a), as well as additional ones. Details on the simulations, the various processes, and their respective cross sections can be found in the Appendices B4 and B5. The simulations produce the lines in figure 5.2(a), showing reasonable agreement with the experimental data. Additional results of the calculations can be found in figure B13 in Appendix B5.2.

5.5 Evolution of the molecular ion

In the following, we discuss the results of our analysis. Our theoretical investigations show that the evolution of the $BaRb^+$ molecule both for the singlet state $(2)^1\Sigma^+$ and the triplet state $(1)^3\Sigma^+$ will at first be dominated by vibrational relaxation collisions, which occur approximately with the Langevin rate $\Gamma_L = 164\,\mathrm{ms}^{-1}$ for the peak atomic density of $8.1 \times 10^{13}\mathrm{cm}^{-3}$ in our cloud (see Appendix B4.1). Typically, these collisions lead to vibrational relaxation in steps of one or two vibrational quanta, with an average of 1.4 vibrational quanta per Langevin collision (see Appendix B5.1). Vibrational relaxation heats up the ion since binding energy is released in form of kinetic energy. This is counteracted by sympathetic cooling due to elastic collisions with Rb atoms, which occur at an average rate of about one elastic collision (with sizable momentum exchange) per vibrational relaxation step (see Appendix B5.1). As a consequence the typical temperature of the $BaRb^+$ ion is below 15 mK during the initial, collision-dominated phase of the evolution. In general, when the collision energy is larger than the binding energy of the $BaRb^+$ molecule, the molecule can also dissociate into a (cold) Ba^+ ion and a Rb atom. For the initial vibrational level $v = -5$ with its binding energy of $2\,\mathrm{mK} \times k_\mathrm{B}$ this process occurs, however, only with a comparatively small rate of about $\Gamma_L/7$ (see Appendix B4.1), and is negligible for deeper vibrational levels. Furthermore, our calculations reveal that for weakly-bound $BaRb^+$ ions in the states $(2)^1\Sigma^+$ and $(1)^3\Sigma^+$ the rate for the substitution reaction $BaRb^+ + Rb \rightarrow Rb_2 + Ba^+$ is negligible. This is a consequence of the fact that the interaction between the Rb atoms is much more short range than between a Rb atom and the Ba^+ ion, see also Appendix B4.1. Concerning the spin-flip collisions we obtain good agreement with the experimental data when using a spin-flip rate of $\Gamma_L/42$ for flips from triplet to singlet (see Appendix B4.2).

Our calculations predict that for the experiments with ODT, which is operated at an intensity of $18\,\mathrm{kW\,cm}^{-2}$, the $(2)^1\Sigma^+$ molecules vibrationally relax typically to

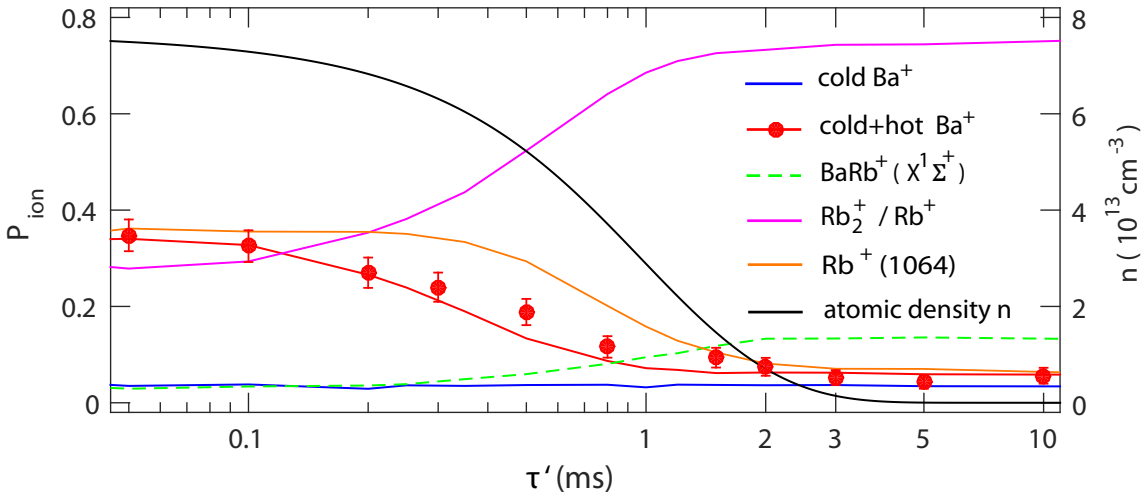

Figure 5.3: Observation of radiative relaxation. The data points give the measured probability P_{Ba^+} of detecting a Ba^+ ion after an extensive laser cooling stage as a function of the time τ' after which a 300 ms long 1064 nm light pulse is applied. For formation of a BaRb^+ molecule, a cold Ba^+ ion is immersed into the atom cloud at $\tau' = 0$. The solid black line represents the time evolution of the atomic density n at the ion trap center (see Appendix B1). All other lines are results of MC calculations for the probabilities of finding the species as denoted in the legend.

a level $v = -12$ ($E_b \approx 50\,\mathrm{mK} \times k_\mathrm{B}$) before either photodissociation or radiative relaxation to the ground state. By contrast, $(1)^3\Sigma^+$ molecules, which cannot radiatively relax to the ground state, typically reach a deeper vibrational level of $v = -21$ ($E_b \approx 460\,\mathrm{mK} \times k_\mathrm{B}$). The photodissociation rates are given by $\Gamma_\mathrm{PD} = \sigma_\mathrm{PD} I/(h\nu)$, where I, h, and ν are the laser intensity, the Planck constant, and the laser frequency, respectively, and σ_PD is the photodissociation cross section. Calculations for σ_PD are presented in Appendix B4.3. For the experiments without ODT (and thus without corresponding photodissociation channel) $(2)^1\Sigma^+$ molecules are expected to relax typically to $v = -18$ ($E_b \approx 230\,\mathrm{mK} \times k_\mathrm{B}$) before radiative relaxation to the ground state takes place.

5.6 Radiative relaxation

Since radiative relaxation to the ground state is predicted to be a central process in the evolution of the BaRb^+ ion, we now test for it experimentally. The idea is to measure for how long BaRb^+ molecules remain in the excited states $(2)^1\Sigma^+$ or $(1)^3\Sigma^+$ before they radiatively relax to the ground state $(X)^1\Sigma^+$. We probe the presence of a BaRb^+ molecule in the states $(2)^1\Sigma^+$ or $(1)^3\Sigma^+$ by photodissociating

it into a Ba^+ ion and a Rb atom with the 1064 nm laser, and then detecting the hot Ba^+ ion. $BaRb^+$ molecules in the ground state $(X)^1\Sigma^+$ cannot be photodissociated by the 1064 nm laser because the photon energy is not sufficient. We start this experiment by moving a single and cold Ba^+ ion into the atom cloud 250 μs after the 1064 nm ODT laser has been switched off. As before, a $BaRb^+$ molecule will form on a time scale of $\Gamma_{\mathrm{tbr}}^{-1} = 0.15$ ms. After the immersion of the Ba^+ ion, we wait for a time τ' before we switch on again the 1064 nm laser [116] to photodissociate the molecule. Before applying the detection scheme for the released hot Ba^+ ion, i.e. long laser cooling and subsequent fluorescence imaging, we remove any remaining $BaRb^+$ molecule by mass-filtering (see Appendix B2). The removal is done, because a remaining $BaRb^+$ molecule can give rise to a spurious hot Ba^+ signal as the laser cooling step can also photodissociate a $BaRb^+$ molecule into a Ba^+ ion and a Rb atom. This is discussed in detail later in section 5.8.

The red data points in figure 5.3 show the probability P_{Ba^+} to detect a Ba^+ ion (hot or cold) at the end of the given experimental sequence for various times τ'. As expected, the Ba^+ signal decreases as τ' increases because the $BaRb^+$ molecule has more time to relax to the $(X)^1\Sigma^+$ state. The decrease to about 1/3 of the initial value takes place within about $\tau' = 0.5$ ms, which represents an approximate time scale for the lifetime of the $(2)^1\Sigma^+$ and $(1)^3\Sigma^+$ $BaRb^+$ molecule, respectively, in the cloud of Rb atoms. For times longer than 2 ms an almost constant value of $P_{\mathrm{Ba}^+} \approx 6\%$ is observed. This remaining population is composed of the following contributions: 4% are cold Ba^+ ions (blue solid line) that have not reacted at all [117] or that have been released again as a result of collisional dissociation. 2% arise probably from $BaRb^+$ molecules that are stuck in the triplet state $(1)^3\Sigma^+$ after the collisional phase when all neutral atoms have left for $\tau' > 2$ ms, and are photodissociated from there by the 1064 nm light. The green dashed curve gives the probability for ending up with a $BaRb^+$ molecule in the electronic ground state. This probability nearly reaches $P_{\mathrm{BaRb}^+} = 20\%$. In principle, this fraction would be about four times as large, if the substitution reaction $BaRb^+(X) + \mathrm{Rb} \rightarrow \mathrm{Ba} + \mathrm{Rb}_2^+$, which depletes electronic ground state $BaRb^+$(X) molecules, were absent [118]. The corresponding reaction rate is expected to be on the order of the Langevin rate (see Appendix B4.1). We note that a Rb_2^+ molecular ion can also decay in the collision $\mathrm{Rb}_2^+ + \mathrm{Rb} \rightarrow \mathrm{Rb}^+ + \mathrm{Rb}_2$, if it is not too deeply bound [119]. In our simulations, however, we do not further pursue this process, and therefore give here the joint probability for finding a Rb_2^+ ion or its Rb^+ decay product (magenta line in figure 5.3). The orange curve, in contrast, gives the probability for Rb^+ ions which are produced via photodissociation by the

1064 nm laser.

5.7 Product ion species

Our discussion so far already indicates that we expect to find a range of ionic products in our experiments, each with a respective abundance. We test this prediction by performing mass spectrometry in the Paul trap after the reactions. As described in more detail in Appendix B2, this is done as follows. When probing for a given ionic product, we use the mass-filter to remove the ion from the Paul trap if it has the corresponding mass. Afterwards, we check whether the Paul trap is now empty (see Appendix B3), knowing that before the mass-filtering a single ion of some species was present. For the experiments without ODT we observe the following abundances after an interaction time $\tau = 10\,\text{ms}$: Ba^+: $4 \pm 2\%$, $BaRb^+$: $29 \pm 5\%$, Rb_2^+: $22 \pm 5\%$, Rb^+: $45 \pm 6\%$. Here, Rb^+ ions are probably created via the aforementioned reaction $Rb_2^+ + Rb \rightarrow Rb^+ + Rb_2$ as the direct process $BaRb^+ + Rb \rightarrow Rb^+ + BaRb$ is slow and even energetically closed for most vibrational states in the ground state $(X)^1\Sigma^+$ (see Appendix B4.1). We expect the detected Ba^+ ions to be cold because there is no photodissociation light present in the given measurement scheme. Our MC simulations are in good agreement with these abundances. From figure B13 we can read off the following values for $\tau > 3\,\text{ms}$: cold Ba^+: $\sim 4\%$, $BaRb^+$: $\sim 26\%$, Rb_2^+/Rb^+: $\sim 70\%$, According to our simulations about 8% of the initial Ba^+ ions end up as a $BaRb^+$ ion in the triplet state $(1)^3\Sigma^+$ while there are no molecules remaining in the singlet state $(2)^1\Sigma^+$ at $\tau = 10\,\text{ms}$. Therefore, the measured $BaRb^+$ fraction of 29% mainly consists of $(X)^1\Sigma^+$ electronic ground state molecules.

5.8 Photodissociation of electronic ground state molecules

Finally, we investigate photodissociation of the $(X)^1\Sigma^+$ state molecules. Once a $BaRb^+$ molecule has relaxed towards $(X)^1\Sigma^+$ it is stable with respect to 1064 nm light, however, photons from the cooling lasers for Ba^+ at the wavelengths of 650 nm or 493 nm can still photodissociate it, see blue and red arrows in figure 5.1(b) [120]. Figure 5.4 shows photodissociation as a function of exposure time Δt for light at 493 nm (a) and at 650 nm (b), respectively. The filled circles represent the fraction of experimental runs where we detect a $BaRb^+$ ion. We probe the presence of a $BaRb^+$

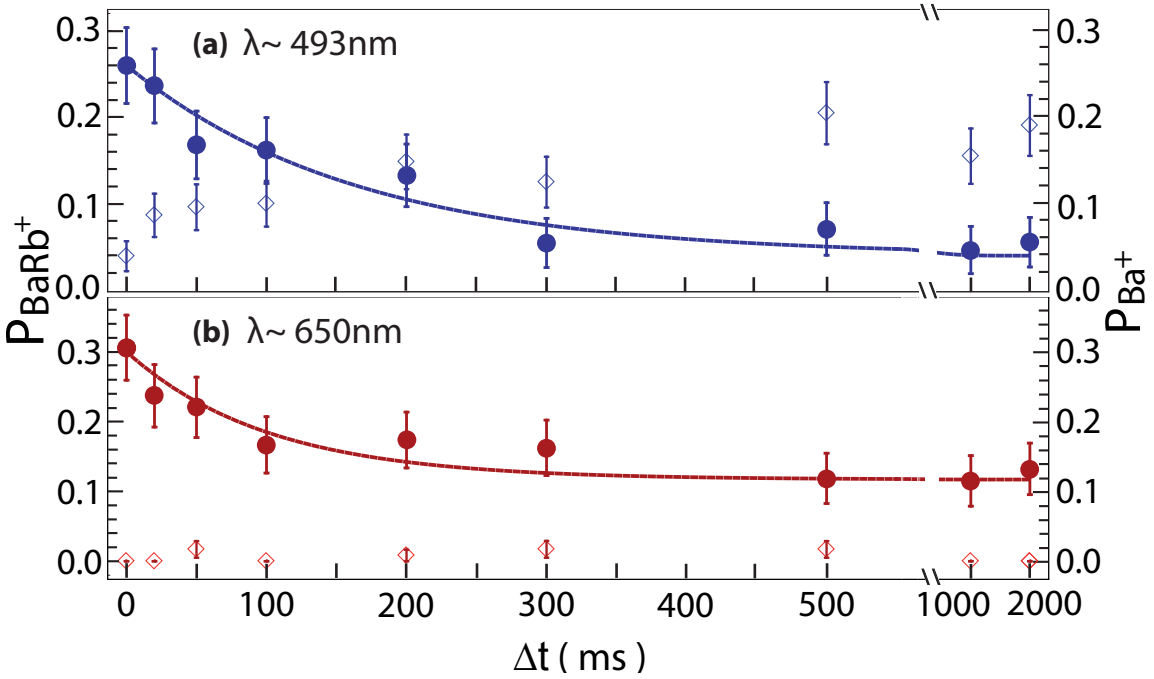

Figure 5.4: Photodissociation of ground state $BaRb^+$ molecules by 493 nm (a) and 650 nm (b) laser light as a function of exposure time Δt. Filled circles show the probability of detecting a $BaRb^+$ molecule. Hollow diamonds give the probability of detecting a Ba^+ ion. The solid lines are fits of an exponential decay plus offset.

ion by measuring whether a corresponding mass-filter removes the ion from the Paul trap, see Appendix B2. The photodissociation laser is switched on $\tau = 10$ ms after immersing the Ba^+ ion into the atom cloud without ODT. The observed decay of the $BaRb^+$ fraction can be approximately described by an exponential plus offset, $P_0 \exp(-\Gamma \Delta t) + P_\infty$ (see solid lines in figure 5.4). The offset P_∞ may stem from $BaRb^+$ ions in certain vibrational levels of the states $(1)^3\Sigma^+$ or $(X)^1\Sigma^+$ which happen to have rather small photodissociation cross sections. As mentioned before, we expect the vibrational distributions in both states to be quite broad. In addition, the PECs indicate that the photodissociation cross sections for both the states $(1)^3\Sigma^+$ and $(2)^1\Sigma^+$ by 493 nm and 650 nm light might be extremely small, because of a missing Condon point at short range for the relevant transitions, see also Appendix B4.3.

From the measured laser intensities of $I_{493} = (180 \pm 40)\,\mathrm{mW\,cm^{-2}}$ and $I_{650} = (260 \pm 50)\,\mathrm{mW\,cm^{-2}}$, we can determine effective, average photodissociation cross sections for the given $(X)^1\Sigma^+$ $BaRb^+$ molecule population distribution over the vibrational states, using $\sigma = \Gamma h\nu / I$. We obtain $\sigma_{493} = (1.2 \pm 0.3) \times 10^{-17}\,\mathrm{cm^2}$ and $\sigma_{650} = (1.0 \pm 0.2) \times 10^{-17}\,\mathrm{cm^2}$.

We now test whether a Ba^+ ion has been produced during photodissociation, see

hollow diamonds in figure 5.4. For the detection of the Ba^+ ion the mass-filtering scheme is used to remove a possibly remaining $BaRb^+$ ion, before long laser cooling and subsequent fluorescence imaging are carried out. For light at 650 nm we do not find any Ba^+ signal. This can be explained with the help of figure 5.1(b). The 650 nm laser couples the $(X)^1\Sigma^+$ state essentially only to the $(3)^1\Sigma^+$ state which, however, dissociates into $Rb^+ + Ba$. In contrast, for light at 493 nm the production of Ba^+ ions is expected, and indeed the loss of $BaRb^+$ signal in figure 5.4(a) directly correlates with an increase of Ba^+ signal. Furthermore, we observe that about half of the produced Ba^+ ions end up in the metastable state $5D_{5/2}$, since their signal is lost as soon as we switch off the 614 nm repump laser. Besides serving as a consistency check, this measurement also demonstrates that single ground state $BaRb^+$ molecules can be detected with high efficiency via fluorescence imaging.

From the experimentally determined cross sections we can estimate that when applying fluorescence imaging photodissociation of a $(X)^1\Sigma^+$ state molecule will on average result in a (hot) Ba^+ ion with a probability of about 70%, and in a Rb^+ ion with a probability of about 30%.

5.9 Conclusions and outlook

In conclusion, we have studied the evolution of a $BaRb^+$ molecule in a gas of ultracold Rb atoms. We find that due to the high predictive power of the theory for the collisional and radiative processes of the $BaRb^+$ molecule only a comparatively small amount of experimental input is necessary to qualitatively pin down the evolution of the molecular ion. In order to experimentally probe the current state of the ion we have developed novel methods which are based on the coordinated concatenation of mass spectrometry, controlled photodissociation, timing of atom-ion interaction, laser cooling, and fluorescence imaging. We find that while the molecular evolution is dominated by vibrational relaxation for the most weakly-bound levels, radiative processes become increasingly important for more deeply bound levels. Furthermore, our work shows how differently the molecules behave depending on their electronic state. The holistic view of the molecular evolution presented here, opens up many new perspectives for future experiments, as it lays out how to prepare and manipulate specific molecular states and how to probe them. In the future, it will be interesting to extend the work presented here to resolve the vibrational and rotational states of the $BaRb^+$ ion. This will allow for investigating collisional and radiative processes and reaction paths so that our understanding can be tested on the quantum level.

Some of the methods presented here are very general and can be directly adopted for studies of a broad range of other atomic and molecular species. These can be, e.g. of interest for research in astrochemistry where reaction chains in the cold interstellar medium are investigated [121–124].

Acknowledgments

This work was supported by the German Research Foundation (DFG, Deutsche Forschungsgemeinschaft) within SFB/TRR21 and by the COMIQ-Network of the European Commission. We would like to acknowledge support in the lab from Joschka Wolf.

Chapter 6

Summary and Outlook

Summary

In this thesis, I have presented results from essentially two experimental projects;

1. In the first project, I minimize excess micromotion due to rf-electrical stray fields in a linear Paul trap with the help of collisions that occur between a single trapped ion and ultracold neutral atoms. We minimize unwanted rf-electrical fields down to the level of about $1\,\mathrm{Vm}^{-1}$. By this minimization, we reduce the ion kinetic energy by a factor of 0.44. The ion kinetic energy after the compensation of dc- and rf-electrical stray fields is about $2.2\,\mathrm{mK} \times k_\mathrm{B}$ when the ion is located inside the cold atomic gas. This residual kinetic energy might be partially explained by collision-induced micromotion. The method discussed here is especially convenient for atom-ion hybrid systems since both species are readily available. Compensating excess micromotion allows for reaching low collisional energies between the atom and ion which is of interest e.g., in the search for shape resonances in atom-ion collisions, see e.g. Ref [86].

2. We have studied the evolution of a BaRb^+ molecule in a gas of ultracold Rb atoms. We have developed novel methods that are based on the coordinated concatenation of mass spectrometry, controlled photodissociation, the timing of atom-ion interaction, laser cooling, and fluorescence imaging to experimentally probe the state of the ion. We find that while the molecular evolution is dominated by vibrational relaxation for the most weakly-bound levels, radiative processes become increasingly important for more deeply bound levels. Furthermore, our work shows how differently the molecules behave depending on their electronic state. The holistic view of the molecular evolution presented

here, opens up many new perspectives for future experiments, as it lays out how to prepare and manipulate specific molecular states and how to probe them. Some of the methods presented in this thesis are very general and can be directly adopted for studies of a broad range of other atomic and molecular species. These can be, e.g. of interest for research in astrochemistry where reaction chains in the cold interstellar medium are investigated [121–124].

Outlook

We will be able to learn more about the evolution of the $BaRb^+$ ion in the gas of ultracold Rb atoms by performing precise spectroscopy on the external and the internal states of the molecule. And, e.g., by putting a $BaRb^+$ ion into a dilute cloud of Rb atoms, one can study whether the reactive collision rate of the molecule is independent of the collision energy as our models predict. Working with a dilute gas of Rb atoms (i..e, $n_{\mathrm{at}} \sim 10^{11} - 10^{12}\,\mathrm{cm}^{-3}$) suppresses the three-body collisions and provides a platform for investigating only two-body collisions in the molecular ion-atom system. The collision energy in our ion trap can be tuned by steps of a few $\mu\mathrm{K} \times k_{\mathrm{B}}$ via adding dc-stray electric fields to the Paul trap which essentially increases the ion micromotion energy.
In the following, I discuss a few of these experiments which can be done in our hybrid atom-ion experiment.

Study on the reactive collision rate of the $BaRb^+$ ion

We expect the vibrational quenching and the substitution reaction of the $BaRb^+$ ion inside the ensemble of very cold Rb atoms to take place roughly at the Langevin rate. This can be experimentally checked in our $BaRb^+$-Rb system by immersing the $BaRb^+$ ions into another new dilute cloud of Rb atoms. I propose to measure the reactive rate of the $BaRb^+$ ion as a function of the collision energy and the atomic density. In the first experiment, the Ba^+ ion is inserted inside of very dense Rb atoms where there is no dipole trap beam. It results in the formation of the $BaRb^+$ ions which are used as inputs for the second experiment in which the molecular ions can be inserted into a new and relatively dilute Rb atomic cloud. Here, the interaction time and the collision energy are experimental parameters that can be adjusted for the second experiment. By measuring the probability of observing the $BaRb^+$ ion after different interaction times and collision energies, one can check whether the reactive

collision rate of the $BaRb^+$ ion is independent of the collision energy, the feature that we expect from the Langevin rate. Yet another thing which can be studied in the above experiments is the type of collisions that can happen in the $BaRb^+$-Rb system. This can be figured out by inserting the molecular ion into the Rb atomic clouds with various densities in the second experiment. While the two-body collision results in a linear change in the reaction rate, any non-linear scaling of the reaction rate by the atomic density can be taken as a signal of few-body collisions between the cold molecular ion and ultracold Rb atoms which can be a very interesting topic for further research.

Study on the reactive collision rate of the Rb_2^+ ion

The study on the reaction rate of the molecular ion can also be done by Rb_2^+ ions which are produced via the substitution reaction $BaRb^+(X) + Rb \rightarrow Ba + Rb_2^+$ in our experiments. Similar to the $BaRb^+$-Rb system, we can insert the Rb_2^+ ion into a new cloud of Rb atoms with different atomic densities, various interaction times and, collision energies so one can determine how the reactive rate of Rb_2^+ ions depends on the collision energy and the atomic density. Here, the reaction $Rb_2^+ + Rb \rightarrow Rb^+ + Rb_2$ can take place for the Rb_2^+ molecular ion provided that it's not too deeply bound.

Toward very cold atom-ion collisions

To reach beyond the limits imposed by collisional induced micromotion (e.g. see Ref [78]) for an atom-ion system, particles should collide when the Paul trap is not in use. There is at least one solution for this in our hybrid system for very short interaction times (i.e., a few tens of μs) as I will explain in the following.

Release and recapture method

Experiments show that the Ba^+ ion can be recaptured in the Paul trap even after 30 μs of turning off the Paul trap. After this time, the probability of finding the Ba^+ drops quickly. Figure 6.1 shows preliminary data of a release and recapture experiment in which the Paul trap was completely switched off at $\tau = 0$ and the ion was released. The trap stays off for a short time scale and then it is switched on again to recapture the ion. A few ms after running the Paul trap, we image the ion to check if the ion still can be re-trapped in the Paul trap. As the data show, there is time τ^* so that for all $\tau < \tau^*$, $P_{\text{rcp}} \approx 1$ where P_{rcp} is the probability of

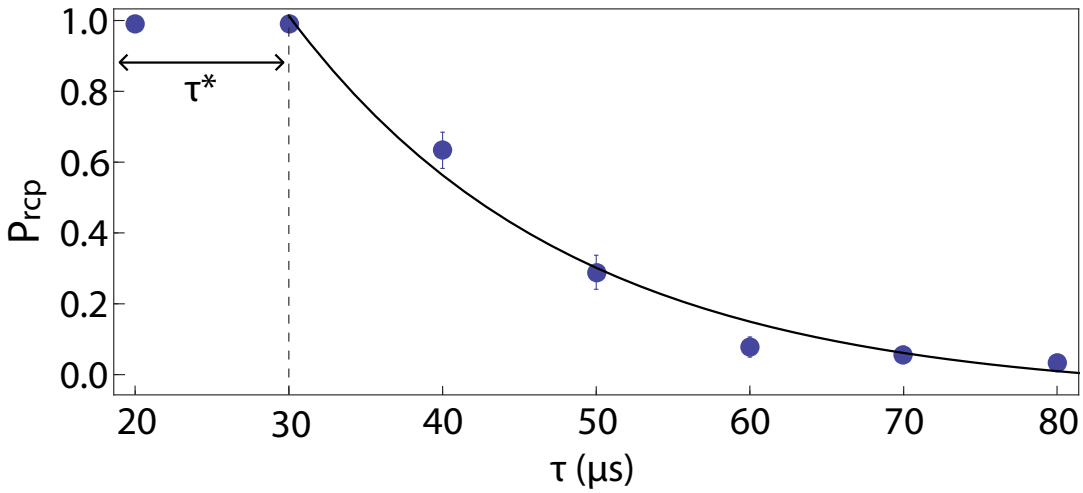

Figure 6.1: The probability of recapturing a well compensated Ba^+ ion in our linear Paul trap after a release time τ. During release, the rf electrodes are switched off and the Ba^+ has no micromotion. For $\tau \leqslant \tau^*$, the Ba^+ can be fully recaptured which make it suitable for micromotion free atom-ion interactions. For $\tau > \tau^*$, $P_{\rm rcp}$ decays with τ. The curve is an exponential fit to experimental data points.

recapturing the Ba^+ ion. In the experiment of figure 6.1, stray dc-electric fields at the trap center have been compensated to better than $0.02\,\mathrm{Vm}^{-1}$ whereas there is no compensation for rf-induced micromotion. Thus, one can check whether minimizing ion micromotion due to the rf-electric fields increases τ^* to more than 30μs or not. For all recapturing times smaller than τ^*, the Ba^+ collides with Rb atoms without any micromotion providing that the collision rate of the ion is greater than $1/\tau^*$. For dense Rb clouds that we use in our experiments with typical atomic density of $n_{\rm at} = 8 \times 10^{13}\mathrm{cm}^{-3}$, the Langevin rate $\Gamma_{\rm Lng}$ is about $165\,\mathrm{ms}^{-1}$ meaning about 5 Langevin collisions can occur within the interaction time τ^*.

The way the ion is released or recaptured is very important since the process can easily heat the ion. As an interesting work for the future, one can find a way to ramp down the oscillating electric fields of the rf electrodes in the Paul trap such that we keep the ion heating rate at minimum.

Appendix

Chapter 7

Appendices

Reprint with permission

Material from:'Amir Mohammadi, Joschka Wolf, Artjom Krükow, Markus Deiß, and Johannes Hecker Denschlag, Minimizing rf-induced excess micromotion of a trapped ion, Applied Physics B: Lasers and Optics, published 2019, Springer-Verlag GmbH Germany'

A Some general considerations on compensating excess micromotion

To compensate excess micromotion, the Paul trap does not have to exhibit perfect rotational symmetry. The motion of a confined ion is determined by the exposure to constant and rf-electrical fields[1]. Concretely, we consider the three electrical fields $\vec{\mathcal{E}}_c, \vec{\mathcal{E}}_{\cos}, \vec{\mathcal{E}}_{\sin}$, characteristic for a Paul trap. $\vec{\mathcal{E}}_c(\vec{r})$ is time-independent, while $\vec{\mathcal{E}}_{\cos}(\vec{r}) \propto \cos(\Omega t)$ and $\vec{\mathcal{E}}_{\sin}(\vec{r}) \propto \sin(\Omega t)$ are quadrature components of the rf-field. The electrical fields $\vec{\mathcal{E}}_c$, $\vec{\mathcal{E}}_{\cos}, \vec{\mathcal{E}}_{\sin}$ can each be Taylor expanded around the trap center position $\vec{r}_0$. For each expansion the first term is a homogeneous offset field and the second term is a quadrupole field, followed by higher multipole terms such as the

[1]We restrict the discussion to the quasi-static regime where dynamical coupling of $\vec{\mathcal{E}}$- and $\vec{\mathcal{B}}$-fields (e.g. induction) can be neglected.

octupole field. In the Paul trap it is the quadrupole field which is used for trapping. For excess micromotion to vanish at $\vec{r}_0$, we need $\vec{\mathcal{E}}_c(\vec{r}_0) = \vec{\mathcal{E}}_{\cos}(\vec{r}_0) = \vec{\mathcal{E}}_{\sin}(\vec{r}_0) = 0$, which is equivalent to the vanishing of the respective offset field terms of the Taylor expansions. The remaining quadrupole fields at location $\vec{r}$ in the direct vicinity of $\vec{r}_0$ will generally dominate over the higher multipole fields, as long as $\vec{r} - \vec{r}_0$ is much smaller than the distance to any of the trap electrodes. The total quadrupole field $\vec{\mathcal{E}}_{\mathrm{qp}}(\vec{r})$ (i.e. the sum of the three quadrupole fields) is fully determined by the second derivatives of the corresponding electrostatic potential ϕ, i.e. $\vec{\mathcal{E}}_{\mathrm{qp}}(\vec{r}) = H(\phi)(\vec{r} - \vec{r}_0)$. Here, $H(\phi)$ is the Hessian matrix of ϕ, i.e. $H_{i,j}(\phi) = \frac{\partial^2 \phi}{\partial x_i \partial x_j}$, where $x_i, x_j \in \{x, y, z\}$. Since $H(\phi)$ is symmetric it can be diagonalized. In the corresponding coordinate system $\{x', y', z'\}$ the electrical quadrupole field can be written as $\vec{\mathcal{E}}_{\mathrm{qp}} = ax'\hat{x}' + by'\hat{y}' + cz'\hat{z}'$, similarly as in Eq. (4.1). Here, a, b, c are time-dependent coefficients. Therefore, the motions of the ion along directions $\hat{x}', \hat{y}', \hat{z}'$ are decoupled and can be described by Mathieu equations. Thus, the main requirements for a Paul trap are fulfilled.

In order to cancel the offset field components of each of the $\vec{\mathcal{E}}_c, \vec{\mathcal{E}}_{\cos}, \vec{\mathcal{E}}_{\sin}$ fields at location $\vec{r}_0$ we can use three compensation electrodes to which we apply suitable dc- and rf-voltages. These electrodes produce electrical fields at $\vec{r}_0$ which are preferentially (but not necessarily) mutually perpendicular to each other.

B

"Life and death of a cold $BaRb^+$ molecule inside an ultracold cloud of Rb atoms"

Amir Mohammadi, Artjom Krükow, Amir Mahdian, Markus Deiß, Jesús Pérez-Ríos, Humberto da Silva Jr., Maurice Raoult, Olivier Dulieu, and Johannes Hecker Denschlag,

arxiv **2005.09338** (2020)

B1 Density evolution of atom cloud

Initially, the prepared ^{87}Rb atom cloud consists of about $N = 6 \times 10^6$ atoms [125] and has a temperature of $T = 750\,\mathrm{nK}$. It is confined in a crossed ODT using laser light at 1064 nm. One ODT beam has a power of 1.6 W and a beam waist of 230 μm at the location of the atoms. The other one has a power of 2.1 W and a waist of 96 μm. Dipole trap frequencies are $(\omega_x, \omega_y, \omega_z) = 2\pi \times (145, 145, 22)\,\mathrm{Hz}$ for the three directions of space $i \in \{x, y, z\}$. Here, the y-axis corresponds to the vertical axis, which is along the direction of the acceleration of gravity g. The initial widths $\sigma_{i,0}$ of the atomic cloud are $\sigma_{i,0} = \omega_i^{-1}\sqrt{k_\mathrm{B}T/m_\mathrm{Rb}}$, where m_Rb is the atomic mass of ^{87}Rb. We obtain $\sigma_{x,0} = \sigma_{y,0} = 9\,\mu$m, and $\sigma_{z,0} = 60\,\mu$m.

When switching off the ODT at a time $t = 0$, the evolution of the density $n(t)$ of the atomic cloud at the position of the ion can be expressed by

$$n(t) = \frac{N(2\pi)^{-3/2}}{\sigma_x(t)\sigma_y(t)\sigma_z(t)} \exp\left(-\frac{g^2t^4}{8\sigma_y^2(t)}\right), \tag{B1}$$

using the atom cloud widths $\sigma_i(t) = \sqrt{\sigma_{i,0}^2 + k_\mathrm{B}Tt^2/m_\mathrm{Rb}}$. In figure 5.2(b) we show the density evolution of the atom cloud at the location of the ion trap center. We note that the interaction time τ is given by $\tau = t - 250\,\mu$s, since the atoms are released 250 μs before the ion is immersed into the atom cloud at $\tau = 0$. In figure 5.3 we have essentially the same density evolution despite the fact that at τ' some laser light at 1064 nm is switched on. We have checked numerically that due to the low intensity of $1.8\,\mathrm{kW\,cm^{-2}}$ used for these measurements the effect of the optical trapping potential is negligible.

B2 Mass filtering

We can selectively remove an ion of a pre-chosen mass from the Paul trap by resonantly heating the ion out of the trap. For this we modulate the voltages on electrodes which are normally used for the compensation of radial stray electric fields at the ion trap center, see Ref. [49] and chapter 4. This modulation shifts the trap center periodically about the axial symmetry axis of the Paul trap. The frequency of the modulation is set to be the mass-dependent trap frequency of the chosen ion species. We typically modulate the trap for a duration of 3 s. We have performed test measurements for deterministically prepared Ba^+, Rb^+, and Rb_2^+ ions. In these cases we observed an efficiency of almost 100% for removing the ion by resonant modulation. We therefore also expect a similar efficiency for a $BaRb^+$ ion. A modulation with

the resonance frequency for a particular ion species does not affect the trapping of an ion of a different species relevant for the present work.

B3 Detection of the ion

In order to detect a single, trapped ion in the Paul trap we have two methods which we describe in the following.

B3.1 Fluorescence detection of a single Ba^+ ion

In order to detect a Ba^+ ion we first separate the ion trap center from the atom trap center by a distance of 100 μm which is much larger than the size of the atomic cloud in order to suppress unwanted collisions. This is done by applying appropriate dc voltages on the Paul trap endcap electrodes. Afterwards, the atoms are released from the ODT by switching it off. After 20 ms, when all atoms have left, we move the ion back to its former position, since this position corresponds to the centers of the cooling laser beams for the Ba^+ ion. Here, the lasers have beam waists ($1/e^2$ radii) of about 20 μm. The cooling laser beams consist of one beam at a wavelength of 493 nm for driving the $6S_{1/2}$ to $6P_{1/2}$ Doppler cooling transition, and one beam at a wavelength of 650 nm for repumping the Ba^+ ion from the metastable $5D_{3/2}$ state towards $6P_{1/2}$. During a laser-cooling time of 100 ms an electron multiplying CCD camera takes a first fluorescence image of the Ba^+ ion. This method allows for detection of a cold Ba^+ ion with a temperature of $T \approx 100$ mK or below, due to the short duration of the laser cooling. A hotter Ba^+ ion, e.g. resulting from photodissociation with a kinetic energy on the order of 0.2 eV, can be detected by taking a second image after long laser cooling. For this, the 493 nm laser beam frequency is red-detuned by 1 GHz and swept back towards resonance within three seconds. Afterwards, we take another fluorescence image, again for a duration of 100 ms. From the two images we can discriminate a hot ion from a cold one. For example, if a fluorescing Ba^+ ion is found in the second image but not in the first one, then this Ba^+ ion was hot at the time of the first image. Furthermore, we can detect whether a Ba^+ ion is in the metastable state $5D_{5/2}$. Such an ion will only appear in the fluorescence image, if we previously pump it out of the $5D_{5/2}$ state, e.g. with a 614 nm laser via the $6P_{3/2}$ level. Therefore, in order to probe for a $5D_{5/2}$ ion, we take two sets of fluorescence images. The first set is without the 614 nm repump laser and the second set is with the 614 nm repump laser. If we only obtain a fluorescence signal in the second set of the images, then the Ba^+ ion was in the

metastable state $5D_{5/2}$.

B3.2 Detection of the ion via atom loss and discrimination of ion species

In our setup only the Ba^+ ion can be detected directly via fluorescence imaging. In order to detect a different ion species such as $BaRb^+$, Rb^+, Rb_2^+ we use a scheme where the ion inflicts atom loss in a cold atom cloud [49, 126]. For this, the ion is kept in the ion trap while a new cloud of neutral atoms is prepared. Then, the ion is immersed into this new atom cloud. Elastic collisions of the ion with the ultracold atoms lead to loss of atoms as they are kicked out of the ODT, which is much shallower than the ion trap. After a given interaction time the remaining number of atoms is measured via absorption imaging. If this number is significantly lower than for a reference measurement using a pure atom cloud an ion is present. Typically we already know from the preparation procedure (and, because all relevant ion species cannot escape from the deep Paul trap potential), that a single ion must be trapped in the Paul trap, but we would like to discriminate between the ion species $BaRb^+$, Rb^+, and Rb_2^+. For this, we carry out mass-filtering in the Paul trap (see Appendix B2), where we remove selectively the ion from the trap if it has a specific, pre-chosen mass. Subsequently, we test whether the ion has been removed from the Paul trap with the ion detection scheme based on inflicted atom loss.

B4 Calculation of cross sections

B4.1 Cross sections from QCT calculations

Model

We use QCT calculations [127] to determine cross sections for elastic collisions, vibrational relaxation, collisional dissociation and substitution reactions in collisions of a $BaRb^+$ ion with an ultracold Rb atom.

Since the three-body process occurs at large internuclear distances we assume that the three-body potential energy surface can be described by pair-wise additive ground-state potentials according to $V(\vec{R}_1, \vec{R}_2, \vec{R}_3) = V(\vec{R}_{12}) + V(\vec{R}_{13}) + V(\vec{R}_{23})$. Here, the Rb-Rb interaction is taken from [128], while the Ba^+-Rb and Ba-Rb^+ interactions are modeled by means of the generalized Lennard-Jones potential $V(R) = -C_4[1 - (R_m/R)^4/2]/R^4$, where $C_4 = 160$ a.u., R is the internuclear distance, $R_m = 9.27\, a_0$, and a_0 is the Bohr radius. We note in passing that $C_4 = \alpha_{\mathrm{Rb}} e^2/[2(4\pi\varepsilon_0)^2]$ is proportional to the static dipolar polarizability $\alpha_{\mathrm{Rb}} = 4\pi\varepsilon_0 \times 4.739(8) \times 10^{-29}\mathrm{m}^3$

of the Rb atom [129]. e is the elementary charge and ε_0 is the vacuum permittivity. The Lennard-Jones type potential describes the long-range interaction correctly and leads to a manageable computational time. We note that the C_4 coefficient for a Ba atom is 134 ± 10.8 a.u. [130]. Nevertheless, for saving computational time we simply use the same coefficient for the Ba atom as for the Rb atom in our model. This introduces small quantitative errors of about 5% but does not change the qualitative interpretation.

Using the QCT approach, we study the collisional behavior of $BaRb^+$ molecules in the states $(2)^1\Sigma^+$, $(1)^3\Sigma^+$ as well as $(X)^1\Sigma^+$. We ignore any spin degrees of freedom, which means that the results are the same for both $(2)^1\Sigma^+$ and $(1)^3\Sigma^+$ $BaRb^+$ molecules. Furthermore, we only consider collisions where $BaRb^+$ molecules are initially nonrotating, i.e. $j = 0$. We have numerically checked that for other low j-states the results will not be significantly different at the level of our approximations. In order to determine cross sections and rates for a given electronic and vibrational state we sum over the corresponding rotational distribution of the final products.

In figure B1, the energetically uppermost vibrational levels as derived from the Lennard-Jones potential are shown down to binding energies of about $1\,\mathrm{K}\times k_\mathrm{B}$. For comparison, we also present the results from the PEC calculations for the $(2)^1\Sigma^+$ and $(1)^3\Sigma^+$ electronic states (see Appendix B4.3).

We have carried out QCT calculations for the vibrational levels $v = (-1, -2, ..., -16)$ and for a collisional energy range of $E_\mathrm{c} = 1 - 100\,\mathrm{mK}\times k_\mathrm{B}$. This range for E_c corresponds to a range of the kinetic energy of the $BaRb^+$ ion of $E_\mathrm{c}(1 - \mu/m_\mathrm{Rb})^{-1} = 3.6 - 360\,\mathrm{mK} \times k_\mathrm{B}$, when assuming zero kinetic energy for the atoms. Here, μ is the reduced mass of the Rb-$BaRb^+$ system. For a given set of v and E_c, we determine a suitable maximum impact parameter b_max beyond which no reactions/inelastic processes occur anymore. b_max is typically on the order of the Langevin radius $b_\mathrm{L} = (4C_4/E_c)^{1/4}$. We run batches of 10^4 trajectories, effectively sampling the configuration space including different impact parameters $b < b_\mathrm{max}$ and molecular orientations. As a result we obtain a probability distribution for the different collisional processes. The cross section for a specific collision process κ can be calculated as $\sigma_\kappa = \pi\, b_\mathrm{max}^2\, P_\kappa$, where P_κ is the probability for a trajectory undergoing this process.

Results

- *Vibrational relaxation:* Figure B2 shows the cross sections for vibrational relaxation for the states $(2)^1\Sigma^+$ and $(1)^3\Sigma^+$ for different collision energies. The calculations clearly reveal that in general the vibrational relaxation cross sec-

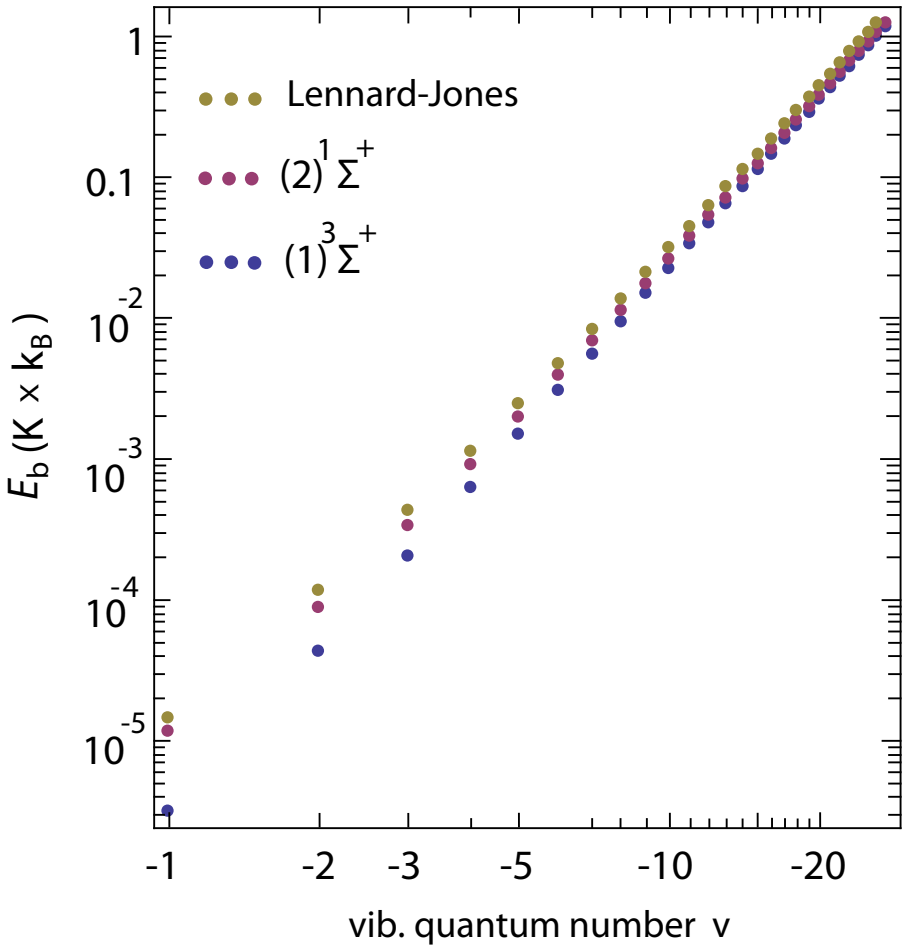

Figure B1: Vibrational binding energies of a $BaRb^+$ molecule for the electronic states $(1)^3\Sigma^+$ and $(2)^1\Sigma^+$. The rotation is in the ground state, i.e. $j = 0$. The brown data points result from the Lennard-Jones potential which is used for the QCT calculations. The purple and blue data points are the results from our calculated $(1)^3\Sigma^+$ and $(2)^1\Sigma^+$ PECs, as described in Appendix B4.3.

tion is well approximated by the Langevin cross section $\sigma_{\mathrm{L}}(E_{\mathrm{c}}) = \pi\sqrt{4C_4/E_{\mathrm{c}}}$. The corresponding Langevin rate $\Gamma_{\mathrm{L}}(t) = \sigma_{\mathrm{L}} v_{\mathrm{ion}} n(t) = K_{\mathrm{L}} n(t)$ is independent of the collision energy. Here, $v_{\mathrm{ion}} = \sqrt{2E_{\mathrm{c}}/\mu}$ is the velocity of the $BaRb^+$ ion and $K_{\mathrm{L}} = 2\pi\sqrt{2C_4/\mu} = 2.03 \times 10^{-9}\,\mathrm{cm^3 s^{-1}}$ is the Langevin rate constant. We note that in our calculations vibrational relaxation typically leads to a change in the vibrational quantum number v by one or two units, i.e. $v' = v-1, v-2$. The average change is 1.4 units, as discussed later in Appendix B5.1. Since these results are quite independent of the initial vibrational quantum number (see figure B2), we adopt them for levels which are more deeply-bound than $v = -16$. Furthermore, we use them also for vibrational relaxation in the

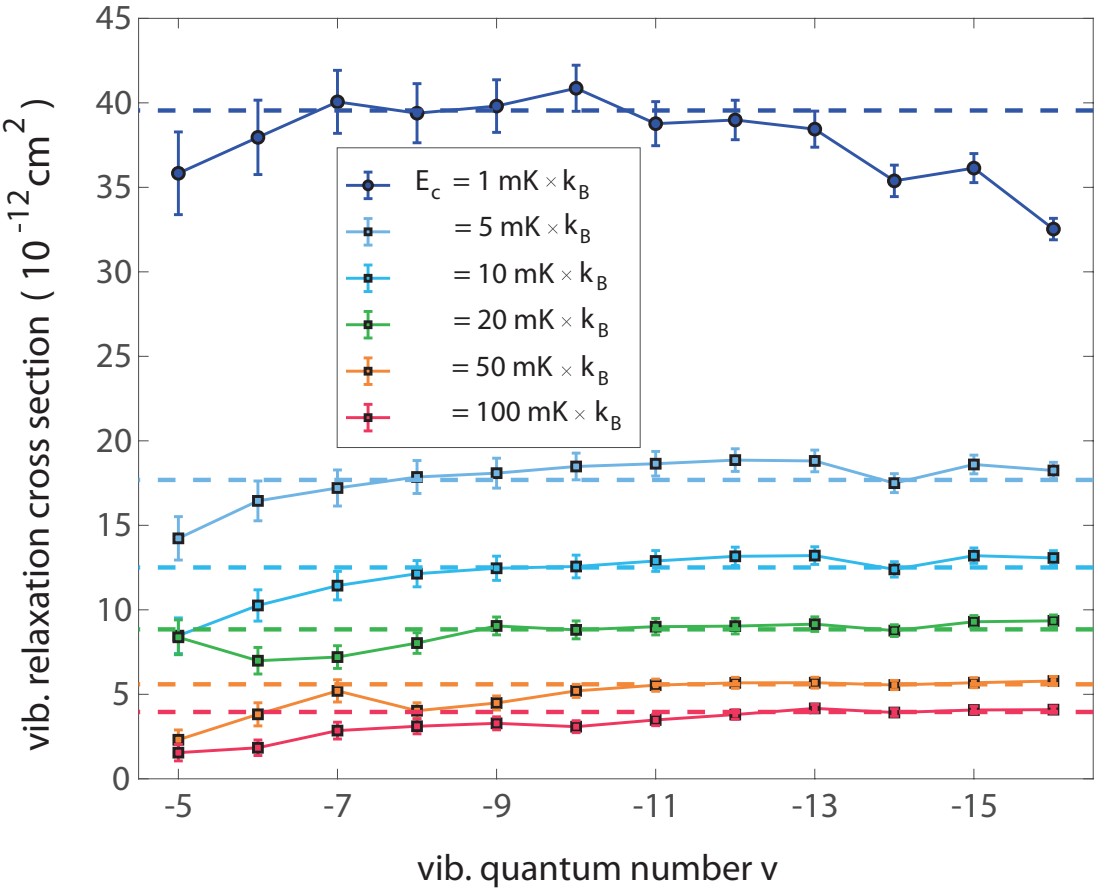

Figure B2: Vibrational relaxation cross section as a function of the vibrational quantum number v, for various collision energies E_c. Shown are results of QCT calculations. The error bars represent 1σ standard deviation obtained by evaluating the numbers of trajectories leading to the same outcomes. The dashed lines are the Langevin cross sections.

ground state $(X)^1\Sigma^+$. If the collision energy is large enough, in principle, also vibrational excitation could occur, but for our settings the calculations show that this is quite negligible.

- *Substitution reaction* $BaRb^+ + Rb \rightarrow Rb_2 + Ba^+$: For the weakly-bound levels of the $(2)^1\Sigma^+$ and $(1)^3\Sigma^+$ electronic states this reaction is in general so rare that it can be neglected. This can be explained as follows in a simple classical picture. The Ba^+ ion and the Rb atom of the weakly-bound $BaRb^+$ molecule are generally well separated. The colliding free Rb atom mainly interacts with the Ba^+ ion via the long-range polarization potential while the interaction between the two Rb atoms is essentially negligible. Hence, the formation of

the neutral Rb_2 molecule is unlikely. For the ground state $(X)^1\Sigma^+$ the reaction is energetically closed.

- *Substitution reaction* $BaRb^+ + Rb \rightarrow BaRb + Rb^+$: For the weakly-bound levels of the $(2)^1\Sigma^+$, $(1)^3\Sigma^+$ and $(X)^1\Sigma^+$ electronic states this reaction is rare because it entails the formation of a neutral molecule, following similar arguments as for the previously discussed reaction $BaRb^+ + Rb \rightarrow Rb_2 + Ba^+$. In addition, for the weakly-bound levels of $(2)^1\Sigma^+$ and $(1)^3\Sigma^+$ the reaction would require a charge transfer between the Rb atom and the Ba^+ ion, since for these electronic states and long binding lengths the positive charge is almost completely located on the Ba atom within the $BaRb^+$ molecule. For deeply-bound levels in the ground state $(X)^1\Sigma^+$ with $v \lesssim 90$ the reaction is energetically closed. This covers about 70% of the produced ground state molecules, as discussed in Appendix B4.3. For these reasons we ignore this substitution reaction in our model.

- *Substitution reaction* $BaRb^+ + Rb \rightarrow Rb_2^+ + Ba$: For the weakly-bound levels of the states $(2)^1\Sigma^+$ and $(1)^3\Sigma^+$ this reaction involves a charge exchange and is therefore negligible. For the weakly-bound levels of the ground state $(X)^1\Sigma^+$, where the positive charge of the $BaRb^+$ molecule is located on the Rb atom, the substitution reaction can have a sizable probability. From numerical QCT calculations for the most weakly-bound levels we can extrapolate roughly the scaling law $\sigma \approx a_0^2\, E_b/(\mathrm{mK} \times k_B)$ for the cross section. Thus, the cross section increases linearly with the binding energy. We expect this to be approximately valid up to a binding energy of about $1000\,\mathrm{K} \times k_B$, where the expression should smoothly go over to the Langevin cross section.

- *Elastic collisions:* Due to the restriction $b < b_{\max}$ we do in general not take into account all elastic collisions. In particular those with very little energy transfer are omitted since they are irrelevant for sympathetic cooling. To a first approximation, the elastic cross section for which sizable amounts of kinetic energy are transferred between the collision partners is the Langevin cross section. This is valid for all states, i.e. $(2)^1\Sigma^+$, $(1)^3\Sigma^+$, and $(X)^1\Sigma^+$.

- *Collisional dissociation:* A $BaRb^+$ molecule can dissociate in a collision with a Rb atom, if the collision energy E_c is large enough. For a weakly-bound $BaRb^+$ molecule in the state $(1)^3\Sigma^+$ or $(2)^1\Sigma^+$ this would lead to a release of a Ba^+ ion and a Rb atom. In our experiments, however, the typical collision

energy is too small. Therefore, this process is relevant only for the most weakly-bound $BaRb^+$ molecules. In our simulation this only concerns the vibrational level $v = -5$ in the states $(2)^1\Sigma^+$ and $(1)^3\Sigma^+$. It has a binding energy of $\approx 2\,\mathrm{mK} \times k_\mathrm{B}$. For a collision energy of $E_\mathrm{c} = 2\,\mathrm{mK} \times k_\mathrm{B}$, which is typical in the beginning of our experiments, the calculated dissociation cross section is then $4 \times 10^{-12}\,\mathrm{cm}^2$ [127]. This is about a factor of seven smaller than the Langevin cross section.

B4.2 Spin-flip cross section

If the $BaRb^+$ ion is in the triplet $(1)^3\Sigma^+$ (singlet $(2)^1\Sigma^+$) state it may undergo an electronic spin-flip towards the singlet $(2)^1\Sigma^+$ (triplet $(1)^3\Sigma^+$) state in a close-range collision with a Rb atom. Discussions of spin-flip processes for molecules can be found in the literature, see, e.g., [30, 131, 132].

We estimate the spin-flip cross section in the following way. In the collision between a Rb atom and a $BaRb^+$ molecular ion we only consider the interaction between the free Rb atom and the Ba^+ ion which is loosely bound in the $BaRb^+$ molecule. Spin-flips can occur when the two electron spins of the Ba^+ ion and the free Rb atom are opposite to each other, e.g. $m_s(\mathrm{Ba}^+) = 1/2$ and $m_s(\mathrm{Rb})$ = -1/2, such that after the collision the spins are $m_s(\mathrm{Ba}^+) = -1/2$ and $m_s(\mathrm{Rb}) = 1/2$. Here, m_s is the magnetic quantum number of the electron spin. Taken by itself, the state $m_s(\mathrm{Ba}^+) = 1/2$, $m_s(\mathrm{Rb})$ = -1/2 is a 50% / 50% superposition state of spin singlet and spin triplet. In the following we estimate the spin-flip cross section for such a superposition state. The actual spin-flip cross section for our experiment should be a fraction of this, because the statistical factors of the total spin-decomposition need to be taken into account. This requires an analysis, in how far a spin-flip of the bound Ba^+ ion leads to a flip of the total electron spin in the $BaRb^+$ molecule. Such an analysis is, however, beyond the scope of the present work.
The spin-exchange cross section for the 50% / 50% superposition state can be estimated using a partial-wave approach [59, 133] as

$$\sigma_\mathrm{sf}(E_c) = \frac{\pi}{k^2} \sum_l (2l+1) \sin^2\left(\delta_l^S(E_\mathrm{c}) - \delta_l^T(E_\mathrm{c})\right), \tag{B2}$$

where $\delta_l^S(E_\mathrm{c})$ and $\delta_l^T(E_\mathrm{c})$ are the energy dependent phase-shifts of the partial wave l for the singlet and triplet atom-ion potential energy curves, respectively. Here, k is the wave number of the relative momentum in the center-of-mass frame. Next, we determine an angular momentum l_max such that for $l > l_\mathrm{max}$ the phase-shift

$\delta_l^S(E_\mathrm{c}) \approx \delta_l^T(E_\mathrm{c})$. This is possible, because for large enough l the particles only probe the long-range tail of the ion-atom potential and this tail is essentially the same for singlet and triplet states. Therefore, only trajectories with $l \leq l_\mathrm{max}$ contribute to the cross section. For $l \leq l_\mathrm{max}$ we estimate the contribution of each partial wave term in equation (B2) by using the random phase approximation for the phase-shifts, $\sin^2\left(\delta_l^S(E_\mathrm{c}) - \delta_l^T(E_\mathrm{c})\right) = 1/2$ [59]. The partial wave l_max can be estimated [134] using the critical impact parameter (Langevin radius) via $l_\mathrm{max} = b_\mathrm{L} k = (2C_4/E_\mathrm{c})^{1/4} k$, as for impact parameters $b > b_\mathrm{L}$ the inelastic cross section vanishes in the classical regime. Carrying out the sum in equation (B2) up to l_max we obtain

$$\sigma_\mathrm{sf}(E_\mathrm{c}) = \frac{\pi l_\mathrm{max}^2}{2k^2} = \frac{\pi}{2}\left(\frac{2C_4}{E_\mathrm{c}}\right)^{1/2} = \frac{\sigma_\mathrm{L}(E_\mathrm{c})}{2}\,. \tag{B3}$$

The spin-flip rate is then simply proportional to the Langevin rate Γ_L. We stress again, that equation (B3) is only an estimate. Therefore, for our simulations we allow for another constant fit parameter γ such that the spin-flip rate for a transition from the singlet state to the triplet state is given by

$$\Gamma_\mathrm{sf} = \gamma\,\Gamma_\mathrm{L}\,. \tag{B4}$$

For determining γ we use experimental data for which the ODT is off. When setting $\gamma = 1/14$ we obtain good agreement with our measurements.

Finally, we note that the spin-flip rate for a transition from a triplet state to a singlet state is not Γ_sf but $\Gamma_\mathrm{sf}/3$. This is because a spin-flip process between the bound Ba^+ ion and the free Rb atom does not necessarily change a triplet $BaRb^+$ molecule into a singlet one. Collisions with an unpolarized sample of Rb will in general shuffle around the total spin S of the molecule equally between the four levels $S = 0, m_S = 0$ and $S = 1, m_S = -1, 0, 1$. Thus, on average only 1 in 3 spin-exchange collisions of a triplet $BaRb^+$ molecule will produce a singlet $BaRb^+$ molecule.

B4.3 Radiative relaxation and photodissociation cross sections

In the following we calculate cross sections for radiative relaxation and photodissociation. For this, we first calculate PECs, wave functions and transition dipole moments. Table B1 shows electronic states for relevant transitions. In the following discussion, the spin-orbit interaction will be neglected.

Table B1: List of the relevant electronic states, Λ, for the $BaRb^+$ molecule that can be reached from the entrance channel upon absorption of a photon of 1064 nm wavelength. The entrance channel is spanned by the electronic states $(2)^1\Sigma^+$ and $(1)^3\Sigma^+$ which correlate in the asymptotic limit to $\mathrm{Rb}\,(5s\,^2S) + \mathrm{Ba}^+\,(6s\,^2S)$. $E_{\mathrm{k,max}}$ is the atom-ion relative kinetic energy released after photodissociation when the initial molecule is weakly bound. σ_{max} is the largest estimate for the state-to-state absorption cross section for a $BaRb^+$ molecule with binding energy $E_b = 1\,\mathrm{K}\times k_{\mathrm{B}}$ (see also Appendix B4.3).

Λ	Asymptotic limit	$E_{\mathrm{k,max}}$ (cm^{-1})	σ_{max} (cm^2)
$(2)^3\,\Sigma^+$	$\mathrm{Rb}^+ + \mathrm{Ba}\,(6s5d\,^3D)$	≈ 8240	negligible
$(1)^3\,\Pi$			negligible
$(3)^1\,\Sigma^+$	$\mathrm{Rb}^+ + \mathrm{Ba}\,(6s5d\,^1D)$	≈ 5927	$\approx 10^{-25}$
$(1)^1\,\Pi$			$\approx 10^{-27}$
$(3)^3\,\Sigma^+$	$\mathrm{Rb}^+ + \mathrm{Ba}\,(6s6p\,^3P)$	≈ 4778	$\approx 9\times 10^{-20}$
$(2)^3\,\Pi$			$\approx 4\times 10^{-20}$
$(4)^1\,\Sigma^+$	$\mathrm{Rb}\,(5s\,^2S) + \mathrm{Ba}^+\,(5d\,^2D)$	≈ 4045	$\approx 4\times 10^{-19}$
$(2)^1\,\Pi$			$\approx 2\times 10^{-27}$
$(4)^3\,\Sigma^+$			$\approx 4\times 10^{-21}$
$(3)^3\,\Pi$			$\approx 2\times 10^{-21}$

Potential energy curves

The PECs displayed in figure 5.1(b), the permanent electric dipole moments (PEDMs), and the transition electric dipole moments (TEDMs) for the $BaRb^+$ molecule are obtained by the methodology described, e.g., in [135–137]. Briefly, the calculations are carried out using the Configuration Interaction by Perturbation of a Multiconfiguration Wave Function Selected Iteratively (CIPSI) package [138]. The electronic structure is modeled as an effective system with two valence electrons moving in the field of the Rb^+ and Ba^{2+} ions represented by effective core potentials (ECP), including relativistic scalar effects, taken from Refs. [139,140] for Rb^+ and Refs. [141,142] for Ba^{2+}. The ECPs are complemented with core polarization potentials (CPP) depending on the orbital angular momentum of the valence electron [143, 144], and parametrized with the Rb^+ and Ba^{2+} static dipole polarizabilities and two sets of three cut-off radii [145, 146]. Only the remaining two valence electrons are used to calculate the Hartree-Fock and the excitation determinants, in atom-centered Gaussian basis sets, through the usual self-consistent field (SCF) methodology. The basis

set used for the Rb atoms is from Refs. [135, 136], and the one for Ba is from Refs. [146, 147]. A full configuration interaction (FCI) is finally achieved to obtain all relevant PECs, PEDMs, and TEDMs. In Ref. [86] a comparison between these calculations for several systems, including $BaRb^+$, and the ones available in the literature is given for the $(X)^1\Sigma^+$ and $(2)^1\Sigma^+$ electronic states.

Since for the states $(1)^3\Sigma^+$ and $(2)^1\Sigma^+$ we need to consider extremely weakly bound vibrational levels, PECs have to be calculated up to large inter-particle distances. For this, we analytically extend the existing short-range PECs by matching them to the atom-ion long-range interaction behavior

$$\lim_{R\to\infty} V(\Lambda;\, R) = D_e - \frac{C_4}{R^4}\,, \tag{B5}$$

where D_e is the dissociation energy of the electronic state Λ. From fits of equation (B5) to our *ab initio* PECs at around $25\,a_0$, we obtain a C_4 value of about $C_4 = 171$ a.u., which is close to the known value $C_4 = 160$ a.u. for Rb atoms.

We note that the asymptotic energies ($R \to \infty$) for our PECs are in reasonable agreement with experimental values. There is virtually no error regarding those asymptotes for which each valence electron is localized on one atomic core [e.g., for the asymptotes $\mathrm{Rb}\,(5s\,^2S) + \mathrm{Ba}^+\,(6s\,^2S)$ and $\mathrm{Rb}\,(5s\,^2S) + \mathrm{Ba}^+\,(5d\,^2D)$]. However, if both valence electrons are localized on the Ba atom we obtain deviations from experimental values of $-180\,\mathrm{cm}^{-1}$ for the $\mathrm{Rb}^+ + \mathrm{Ba}\,(6s^2\,^1S)$ asymptote, $-120\,\mathrm{cm}^{-1}$ for the $\mathrm{Rb}^+ + \mathrm{Ba}\,(6s6p\,^3P)$ asymptote, and $420\,\mathrm{cm}^{-1}$ for the $\mathrm{Rb}^+ + \mathrm{Ba}\,(6s5d\,^1D)$ asymptote, respectively [146].

Calculation of wave functions

The diatomic eigenvalue problem is solved for each PEC $V(\Lambda;\, R)$ by means of the mapped Fourier grid Hamiltonian (MFGH) method [148], which diagonalizes a discrete variable representation (DVR) matrix of the Hamiltonian. We use a fairly large internuclear distance range, $R_{\max} \approx 5000\,a_0$, in order to even accommodate small binding energies E_b on the order of $E_b \approx 10\,\mu\mathrm{K} \times k_\mathrm{B}$.

The energy-normalized continuum wave functions $|\Lambda' j';\, k\rangle$ are computed using a standard Numerov method [149]. Here, j' is the rotational quantum number. Since the kinetic energies at long range for the exit channels correspond to several thousands of wave numbers the calculations are performed on a fairly dense and large grid (between 90,000 and 150,000 grid points) so that there are at least 20 points per wave function oscillation.

Transition electric dipole moments

The TEDMs $D_{\Lambda',\Lambda}(R)$ between relevant electronic states Λ and Λ' are shown in figure B3 as functions of the internuclear distance R. The plots show that Σ–Σ transitions are generally stronger than Σ–Π transitions. Furthermore, the TEDMs vanish at large distances. Such a behavior is expected, since the $Ba^+ + Rb$ asymptote cannot be addressed from the $Rb^+ + Ba$ asymptote by optically exciting one of the atoms [see figure 5.1(b)]. Therefore, for weakly bound rovibrational states all outer turning points can be disregarded, i.e. radiative processes are driven at short range.

Photodissociation

In order to determine the photodissociation cross sections, we calculate the absorption cross sections $\sigma_{\Lambda' j' k,\,\Lambda \upsilon j}(E')$ for the transitions between rovibrational levels (v, j) in the electronic state Λ towards the continuum of an electronic state Λ' [150, 151]

$$\sigma_{\Lambda' j' k,\,\Lambda \upsilon j}(E') = \frac{4\pi^2}{3c}\frac{E'}{2j+1} S(j', j) \left|\langle \Lambda';\, k|\, D_{\Lambda',\Lambda}(R)\, |\Lambda \upsilon\rangle\right|^2 . \tag{B6}$$

Here, $E' = h\nu - E_b$ is the final energy obtained for a given optical frequency ν and binding energy E_b. Furthermore, c is the speed of light, and j' represents the rotational quantum number of the final level. We note that the transition moment $\langle \Lambda';\, k|D_{\Lambda',\Lambda}(R)\,|\Lambda \upsilon\rangle$ is essentially independent of j and j' for the low values of j relevant here. From QCT calculations we estimate a typical range of rotational quantum numbers of $j < 20$ for the $BaRb^+$ ion in our experiments. $S(j', j)$ denotes the Hönl-London factor [152]. In principle, transitions can be grouped into the three branches Q ($j' = j$, Σ–Π transitions only), R ($j' = j + 1$), and P ($j' = j - 1$). In our experiments we drive each of these transitions, if allowed by selection rules. Summing over the P, Q, R contributions one obtains a total cross section which is independent of j. Therefore it is sufficient to present in the following only total cross sections obtained for $j = 0$.

Figure B4 shows the predictions for photodissociation cross sections for 1064 nm light as functions of the binding energy E_b of the initial rovibrational state. Here, the three dominant transitions are presented. We checked numerically that the cross sections follow a $E_b^{0.75}$ scaling law within the shown range of E_b [153]. This can be explained by the increasing localization of the vibrational wave function with

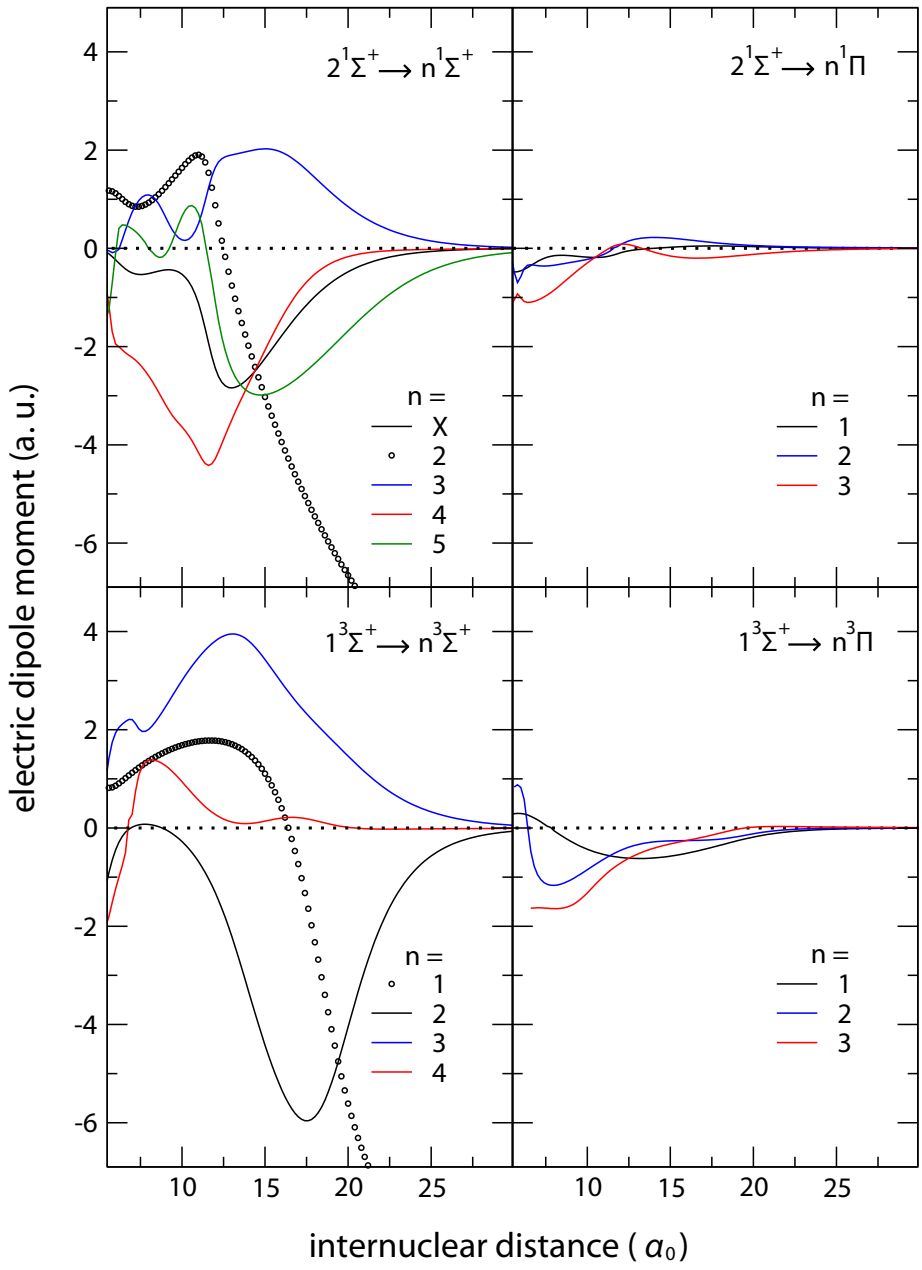

Figure B3: PEDMs (circles) and TEDMs (solid lines) as functions of the internuclear distance of the $BaRb^+$ molecule. Initial and final states are given in the plot. For Σ–Σ transitions the dipole moment along the internuclear axis is shown, whereas for Σ–Π transitions the dipole moment in transverse direction is shown.

increasing binding energy E_b. Our calculations reveal that the transitions are mostly determined by the wave functions at the inner turning points of the PECs.

We note that because of an uncertainty in the calculation of the absolute energy position of the PECs of up to a few hundred $\mathrm{cm}^{-1} \times (hc)$ there are corresponding

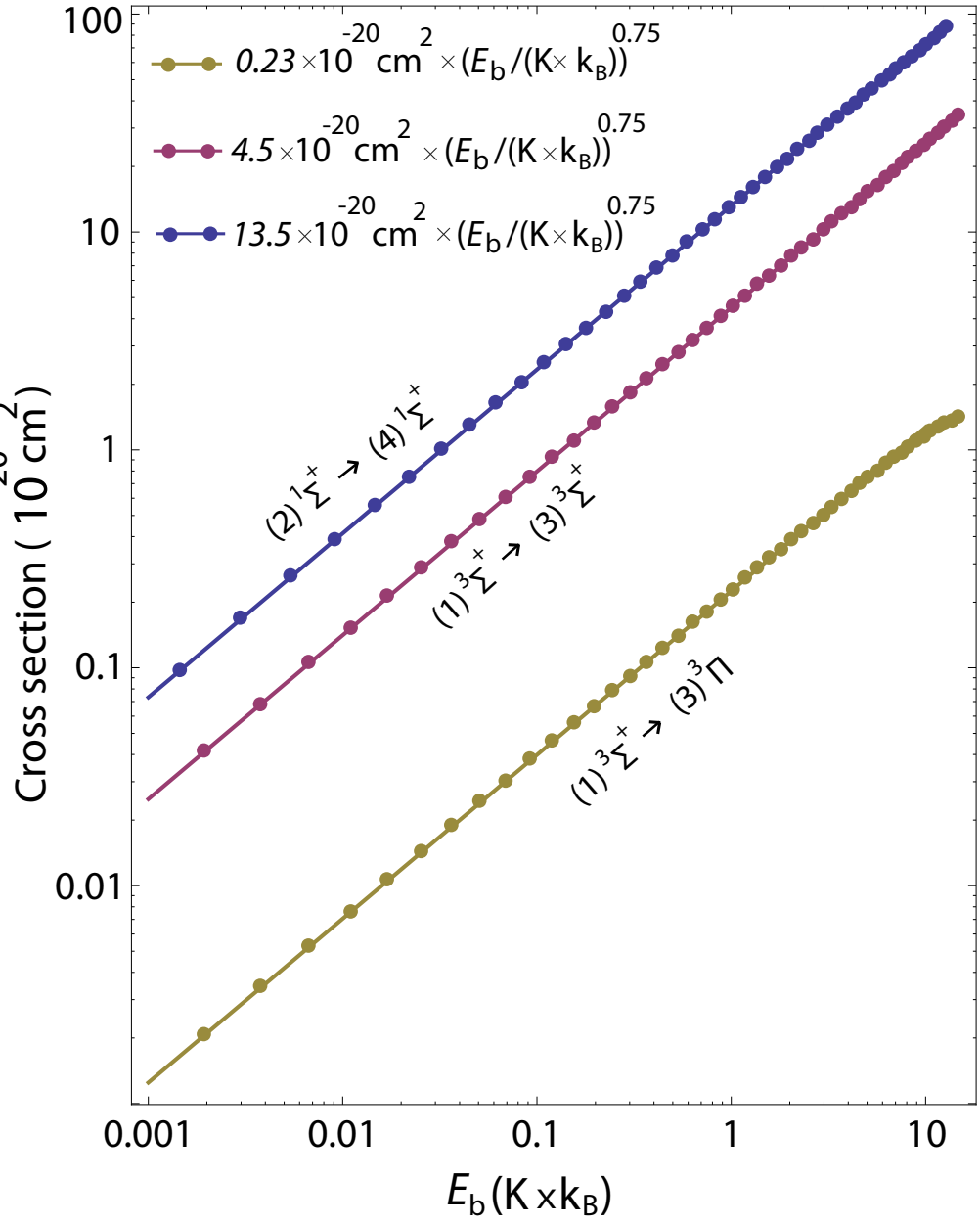

Figure B4: Photodissociation cross sections as functions of the binding energy for an excited state $BaRb^+$ ion exposed to 1064 nm light. Shown are the results for the most relevant transitions in our experiments. Data points are calculations. Solid lines represent fits $\propto E_b^{0.75}$ to the data points (see legend).

uncertainties in the photodissociation cross sections. The possible range of cross sections is investigated in figureB5. Here, $E'/(hc)$ is varied between 8800 and 9800cm^{-1}, i.e. around typical values corresponding to final states addressed via light at 1064nm and starting from initial states with rather small binding energies (see dashed vertical

lines). These calculations are carried out for several binding energies.

The cross sections in figure B5 exhibit oscillations. For a fixed binding energy, the energy interval $\Delta E'$ for a full oscillation between a minimum and a maximum is smaller than about $500\,\mathrm{cm}^{-1} \times (hc)$ for all three presented transitions. This is about the uncertainty of the absolute energy positions of the PECs and therefore the true cross section can actually lie in the range between calculated minimum and maximum values.

The oscillations of the cross sections in figure B5 are associated with the spatial oscillations of the initial rovibrational wave functions. For the sake of clarity, this is illustrated in detail in figure B6. Wherever an anti-node of the initial wave function coincides with the anti-node of the scattering wave function at the inner turning point of the excited PEC, the cross section has a local maximum. This is known as the reflection principle (see, e.g., [154]). The frequency separation of the local cross section maxima clearly depends on the slope of the PEC and the wavelength of the initial wave function.

In order to describe the experimentally measured data (see Appendix B5.2), we use photodissociation cross sections in our MC simulations of the form $\sigma_e \times (E_b/(\mathrm{K} \times k_\mathrm{B}))^{0.75}$. Thus, they exhibit the $E_b^{0.75}$ scaling, which our calculations predict. The pre-factor σ_e, however, is used as free parameter which is determined via fits to the data. In Table B2 we compare the obtained values for σ_e to the theoretically predicted maximal values. We find that the experimental cross section for the transition $(2 \rightarrow 4)^1\Sigma^+$ (for the transition $(1)^3\Sigma^+ \rightarrow (3)^3\Pi$) is by a factor of 13.5 (by a factor of 7) larger than the predicted maximal value. At this point it is not clear how to explain these discrepancies. In contrast, for the transition $(1 \rightarrow 3)^3\Sigma^+$ we find consistency between theory and experiment.

Having discussed in detail the photodissociation by 1064 nm light, we now briefly comment on the photodissociation by 493 nm and 650 nm light. Calculated PECs for highly excited electronic states (not shown here) indicate that the photodissociation of weakly-bound molecules in the $(2)^1\Sigma^+$ and $(1)^3\Sigma^+$ states might be quite strongly suppressed because Condon points might not exist for the relevant transition. This agrees with the experiment, from which we do not have any evidence for this photodissociation process either. Concerning photodissociation of ground state $(X)^1\Sigma^+$ molecules via the laser cooling light, for which we do have experimental evidence (see section 5.8), a theoretical analysis has not been carried out yet.

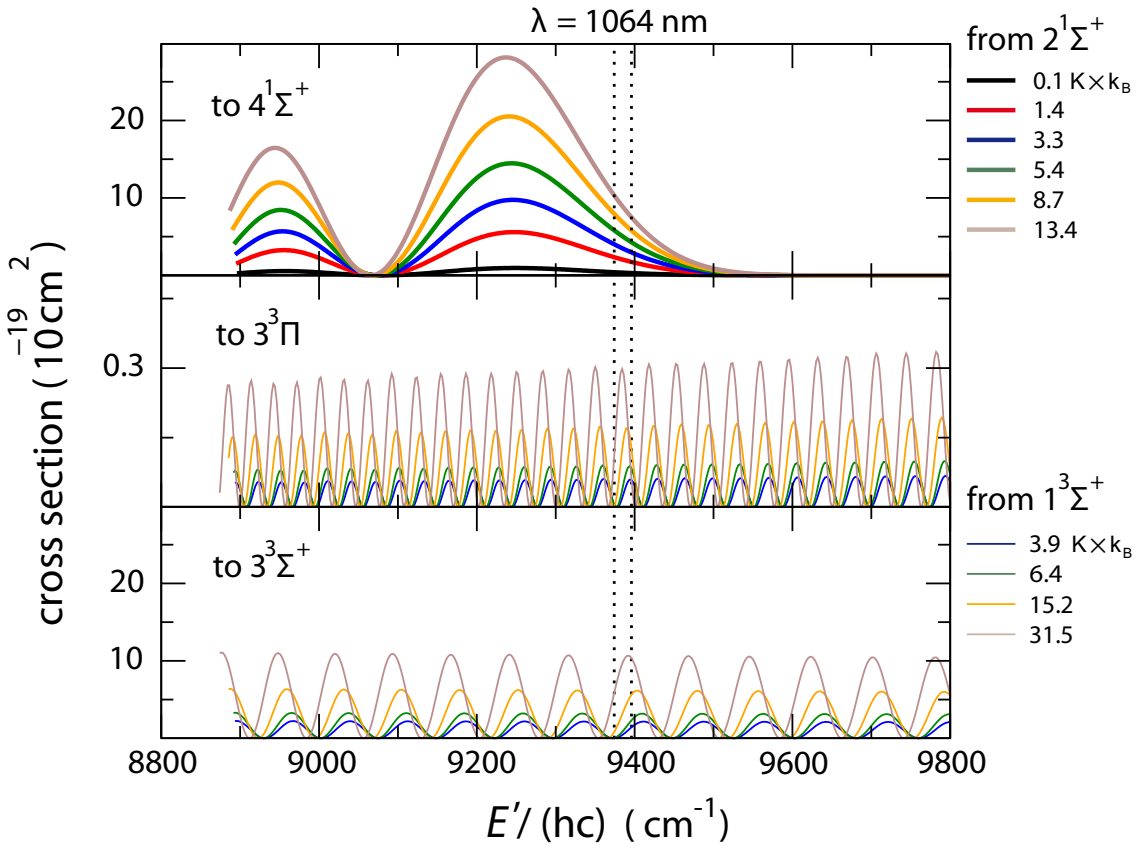

Figure B5: Photodissociation cross sections as functions of the final energy $E' = h\nu - E_b$. Upper panel: $(2)^1\Sigma^+ \rightarrow (4)^1\Sigma^+$. Middle panel: $(1)^3\Sigma^+ \rightarrow (3)^3\Pi$. Lower panel: $(1)^3\Sigma^+ \rightarrow (3)^3\Sigma^+$. The color coding of the lines corresponds to the binding energy of the initial state as indicated on the right. The right (left) vertical dashed line marks the energy E' when a 1064 nm photon excites a molecule with $E_b = 0.1\,\mathrm{K} \times k_\mathrm{B}$ ($E_b = 31.5\,\mathrm{K} \times k_\mathrm{B}$).

Radiative relaxation to the electronic ground state

The excited state $(2)^1\Sigma^+$ can decay radiatively to the ground state $(X)^1\Sigma^+$ by spontaneous emission of a photon. The corresponding radiative lifetime of the $(2)^1\Sigma^+$ molecule is shown in figure B7 as a function of the binding energy E_b, as previously discussed in [86]. The relaxation can in principle lead to dissociation of the $BaRb^+$ molecule into a Rb^+ ion and a Ba atom. However, our calculations of the Franck-Condon factors show that it will dominantly produce a $BaRb^+$ molecule in the $(X)^1\Sigma^+$ state. Figure B8 shows the predicted broad distribution of vibrational levels which are populated. During such a relaxation the kinetic energy of the $BaRb^+$ molecule essentially does not change, because the photon recoil is very small. The radiative relaxation rate is the inverse of the lifetime, i.e. $0.34\times(E_\mathrm{b}/(\mathrm{mK}\times k_\mathrm{B}))^{0.75}\,\mathrm{ms}^{-1}$

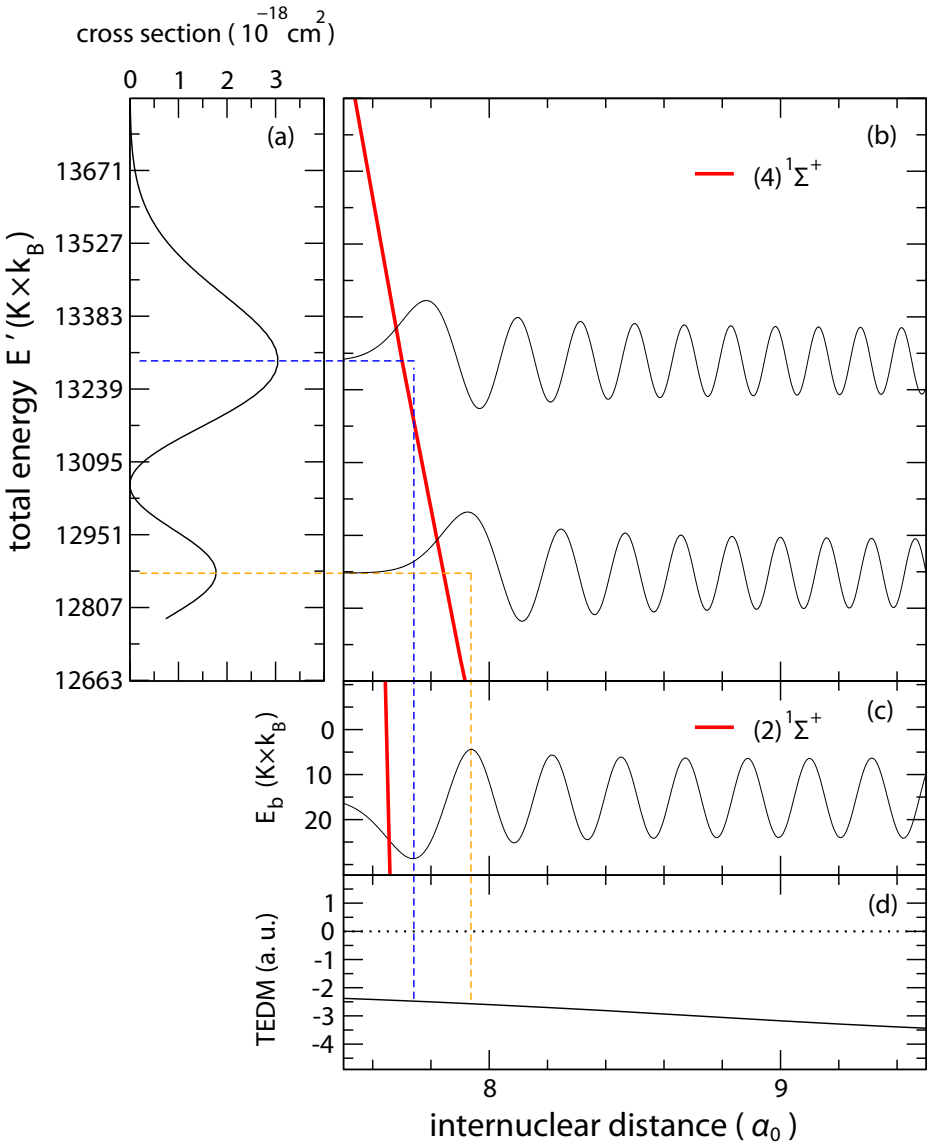

Figure B6: (a) Photodissociation cross section as a function of final energy $E' = h\nu - E_b$ for the transition $(2)\,^1\Sigma^+ \rightarrow (4)\,^1\Sigma^+$. (b) The $(4)\,^1\Sigma^+$ PEC (red curve) and two energy-normalized continuum wave functions (black curves). (c) The $(2)\,^1\Sigma^+$ PEC (red curve) and the rovibrational wave function (black curve) for the binding energy of $E_b = 10.5\,\mathrm{cm}^{-1}$. Blue and orange dashed lines help to illustrate that a good wave function overlap at the inner turning point of the excited PEC leads to a large cross section. (d) The respective TEDM as a function of the internuclear distance R.

(see figure B7). We use this relaxation rate in our MC simulations. The physics behind the scaling $\propto E_b^{0.75}$ is that for an increasing binding energy the wave function becomes more localized at short range where radiative relaxation dominantly occurs.

Table B2: Cross sections σ_e for the three transitions that are taken into account in our MC simulation. The predicted maximal values are given beside the values resulting from fits to the experimental data in our MC simulation. In the last column the released ion for each transition is given.

Transition	max. σ_e (theor.) (10^{-20} cm^2)	σ_e (exp.) (10^{-20} cm^2)	rel. ion
$(2 \rightarrow 4)^1\Sigma^+$	40	540	Ba^+
$(1 \rightarrow 3)^3\Sigma^+$	9	7	Rb^+
$(1)^3\Sigma^+ \rightarrow (3)^3\Pi$	0.23	1.61	Ba^+

For the sake of completeness, we note that radiative relaxation within a given PEC (such as $(2)^1\Sigma^+$ or $(1)^3\Sigma^+$) is negligible in our experiments. As already discussed in [86] these relaxation rates are on the order of seconds.

B5 Monte Carlo Simulations

In this section we describe how we simulate the evolution of a $BaRb^+$ molecule in a Rb atom cloud by means of MC trajectory calculations. For this, we make use of the cross sections we have determined in Appendix B4. In order to reduce the complexity we carry out the calculations in two steps. In a first step we only consider a subset of collision processes. A main finding of these calculations is that the average kinetic energy of the $BaRb^+$ ion only slightly increases as it relaxes down to more deeply bound vibrational states. We use this information in the second step of the MC calculations, where we now include all inelastic and reactive processes but for which we ignore elastic collisions and simply assume that the molecular ion has a constant kinetic energy.

B5.1 Restricted model

Here, we simulate trajectories of a spinless $BaRb^+$ molecule. During each trajectory the molecule can undergo multiple collisions within the gas of Rb atoms. We consider elastic collisions, vibrational relaxation collisions, and collisional dissociation.

The simulation starts with the molecular ion in the vibrational state $v = -5$ below the $Ba^+ + Rb$ asymptote. An example of the evolution of the vibrational state as a function of the collision number for a single trajectory is shown in figure B9. The calculations reveal that vibrational relaxation typically takes place in steps of one or two vibrational quanta. The molecular kinetic energy increases after each vibrational relaxation step and decreases due to sympathetic cooling in elastic collisions.

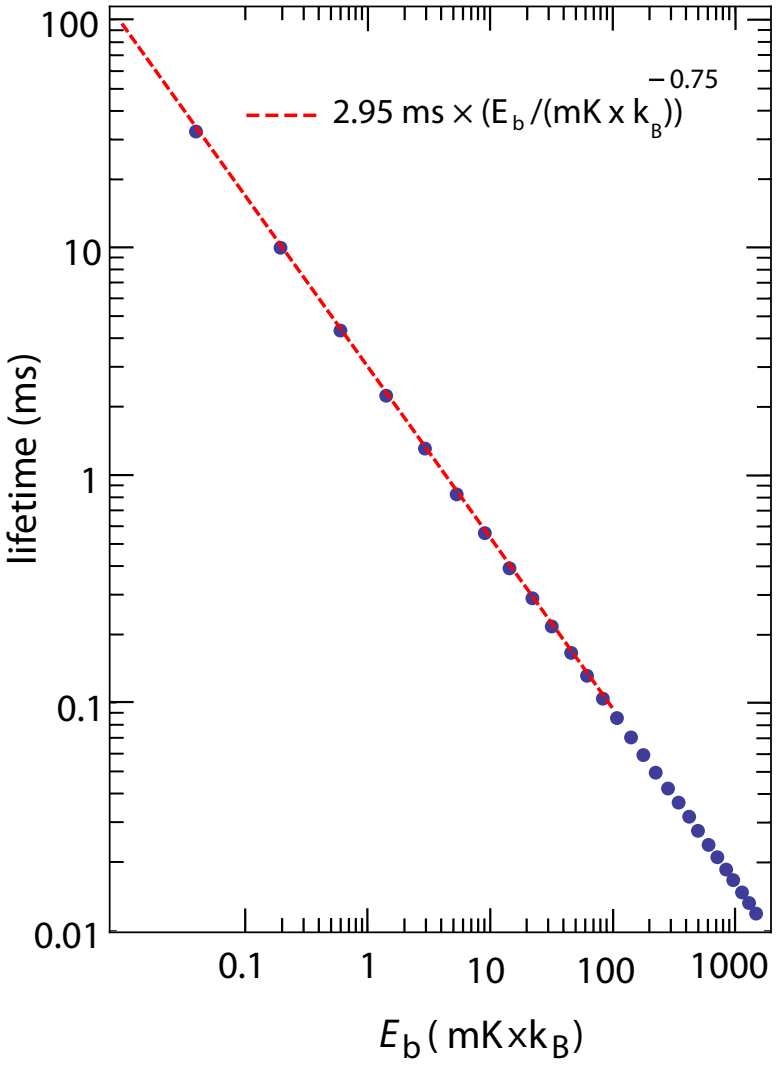

Figure B7: Radiative lifetime (blue dots) for the highest rovibrational levels $(v, j = 0)$ of the $(2)^1\,\Sigma^+$ electronic state, as a function of the binding energy E_b. The red dashed line is a fit $\propto E_b^{-0.75}$ to the data.

Precisely, how much energy is released in a vibrational relaxation step or carried away in an elastic collision depends on the scattering angle of the atom-molecule collision [155]. In the simulations we choose random values for the scattering angle in the center-of-mass frame, which are uniformly distributed.

After analyzing 10^4 calculated trajectories we obtain the following results. Between two vibrational relaxation processes there is on average approximately one elastic collision (see figure B10). Although, overall, the kinetic energy of the molecule increases as it relaxes to more deeply bound states, within the range of interest the

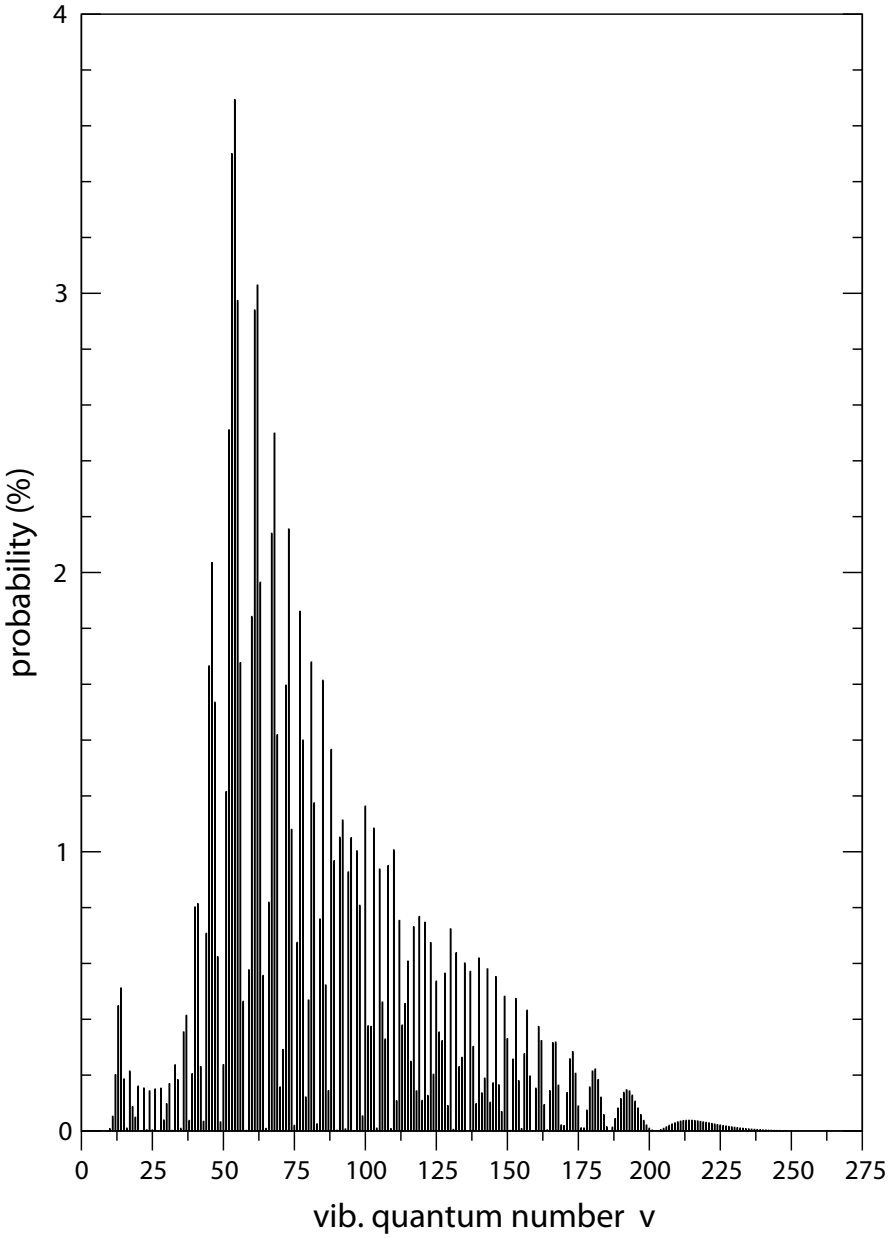

Figure B8: Calculated population distribution for vibrational levels v of the electronic ground state $(X)^1\Sigma^+$ of the $BaRb^+$ molecule after radiative relaxation from a weakly-bound level in the $(2)^1\Sigma^+$ state with $j = 1$. Here, the same approach is used as described in [86].

molecular collision energies are typically only a few mK $\times\, k_\mathrm{B}$ (see figure B11). On average, the molecular ion requires 17.5 ± 4.2 collisions to relax from $v = -5$ down to $v = -17$ of which 9.0 ± 3.8 collisions are elastic. Figure B12 shows the average vibrational quantum number v as a function of the number of vibrational relaxation

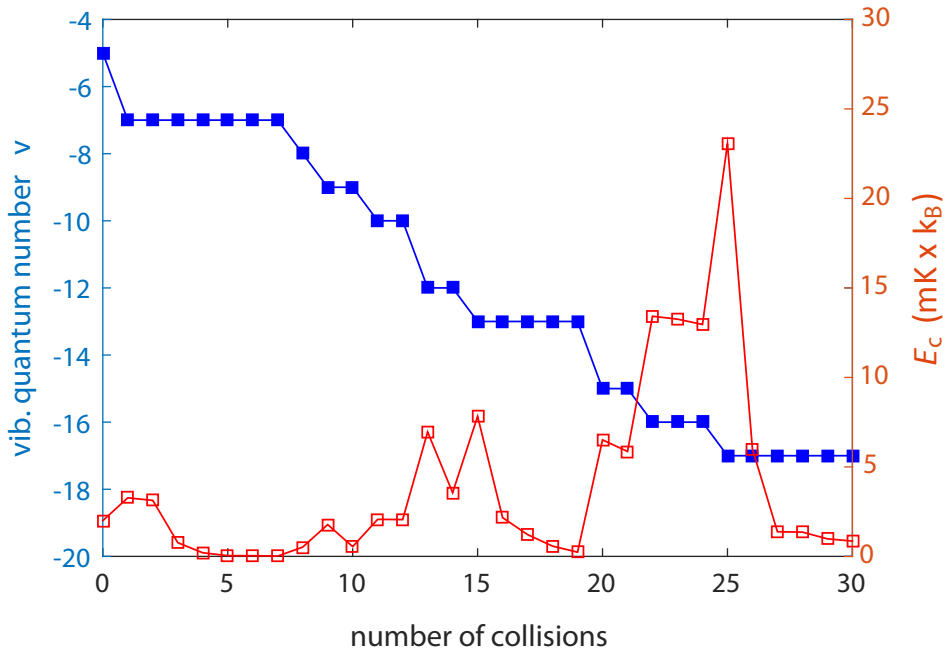

Figure B9: Evolution of the vibrational quantum number of a $BaRb^+$ molecule in collisions with Rb atoms. We only consider the "relevant" collisions which have impact parameters $b < b_{max}$, as discussed in Appendix B4.1. The y-axis on the left shows the vibrational quantum number v and the y-axis on the right shows the collision energy E_c. The data correspond to a single MC trajectory.

collisions. We find that v decreases nearly linearly. On average about 1.4 vibrational quanta are lost per relaxation collision, independent of the initial vibrational quantum number. Since the vibrational relaxation cross section is well approximated by the Langevin cross section (see figure B2) the vibrational quantum number will on average be lowered by one unit at a rate of $1.4 \times \Gamma_L$. We note that also in a recent theoretical investigation of vibrational quenching collisions of weakly-bound Rb_2^+ molecular ions with Rb atoms the changes in the vibrational quantum number are predicted to be small [99].

B5.2 Full model

In the second set of MC trajectory calculations we take into account all the processes discussed in Appendix B4. Furthermore, we also include the formation of the weakly-bound $BaRb^+$ molecule with vibrational quantum number $v = -5$ via three-body recombination. Adopting simple statistical arguments and considering that the Ba^+ ion is initially unpolarized, the probability for the freshly formed molecule to be in

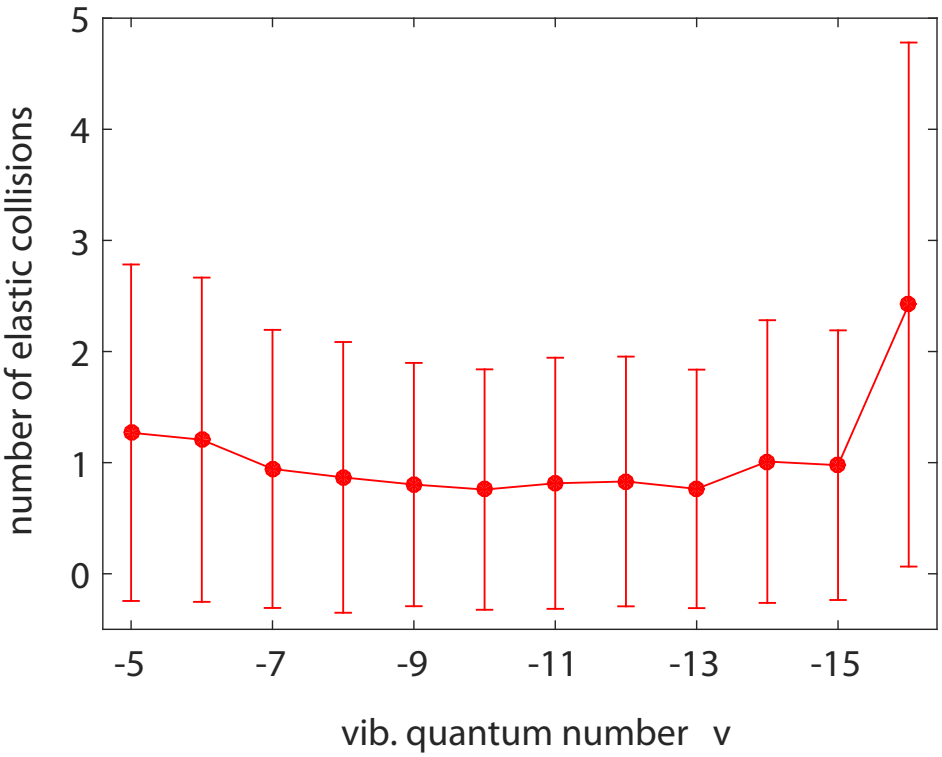

Figure B10: Average number of elastic collisions of Rb atoms with a $BaRb^+$ ion in the vibrational state v before a relaxation (excitation) to another vibrational state occurs. Data points are from MC simulations. The error bars represent 1σ standard deviations.

state $(2)^1\Sigma^+$ ($(1)^3\Sigma^+$) is 1/4 (3/4), respectively.

Motivated by the results in Appendix B5.1 we generally assume a collision energy E_c for the $BaRb^+$ molecule of a few $\mathrm{mK}\times k_\mathrm{B}$. For the collisional dissociation regarding the $v = -5$ level we assume $E_c = 2\,\mathrm{mK} \times k_\mathrm{B}$. Actually, for all other collisional processes the precise value for the collision energy is not relevant since their rates are proportional to the Langevin rate, which is independent of E_c. For the ground state $(X)^1\Sigma^+$, however, the assumption of low collision energy is in general not justified. This is because a vibrational relaxation from a deeply-bound vibrational level to the next one releases a large amount of energy. This puts the ion on an orbit through the Paul trap which is much larger than the size of the atom cloud. As a consequence the rate for further elastic, inelastic, or reactive collisions is significantly reduced. For example, when the $BaRb^+$ molecule in state $(X)^1\Sigma^+$ relaxes from $v = 55$ to $v = 54$ the motional energy of the $BaRb^+$ molecule increases by about $16\,\mathrm{K} \times k_\mathrm{B}$. In order to get cooled back into the atom cloud, the energy has to be lowered to about

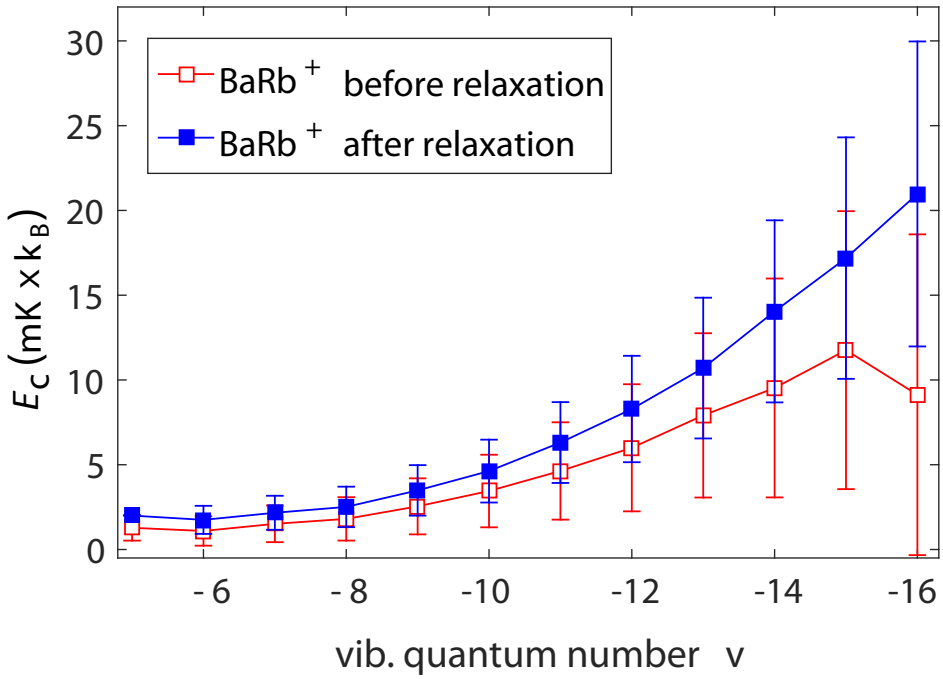

Figure B11: Average collision energy of the $BaRb^+$ ion right after (blue filled squares) and directly before (red open squares) vibrational relaxation as a function of the vibrational quantum number. Data points are results from the MC simulation. The error bars represent 1σ standard deviations. Here, the difference between the curves describes the effect of cooling due to elastic collisions.

$1\,\mathrm{K} \times k_\mathrm{B}$. On average, 44% of the energy is cooled away in a single elastic Langevin collision. Therefore, five elastic Langevin collisions are needed on average, to cool the $BaRb^+$ ion back down into the Rb gas. When we take this cooling time to be $130\,\mu$s long we find good agreement with the data.

Once a highly energetic Ba^+, or a Rb^+, or a Rb_2^+ ion is produced after photodissociation or a substitution reaction, no further reaction takes place in our simulation. However, if a cold Ba^+ ion is created it can again undergo a three-body recombination event with the respective rate and a new evolution starts. Time is typically incremented in steps of $\Delta t = 1\,\mu$s. We typically carry out 2000 trajectories in a MC simulation for a given experimental procedure.

The results of the MC simulations are presented as lines in Figs. 5.2(a), 5.3, and B13. In fact, figure B13 is an extension of figure 5.2(a), showing additional evolution traces for various ion states. The measurements and predictions are shown separately for the case with dipole trap (wODT) and the case without dipole trap (woODT) in figure B13(a) and (b), respectively. The data points are the same as in

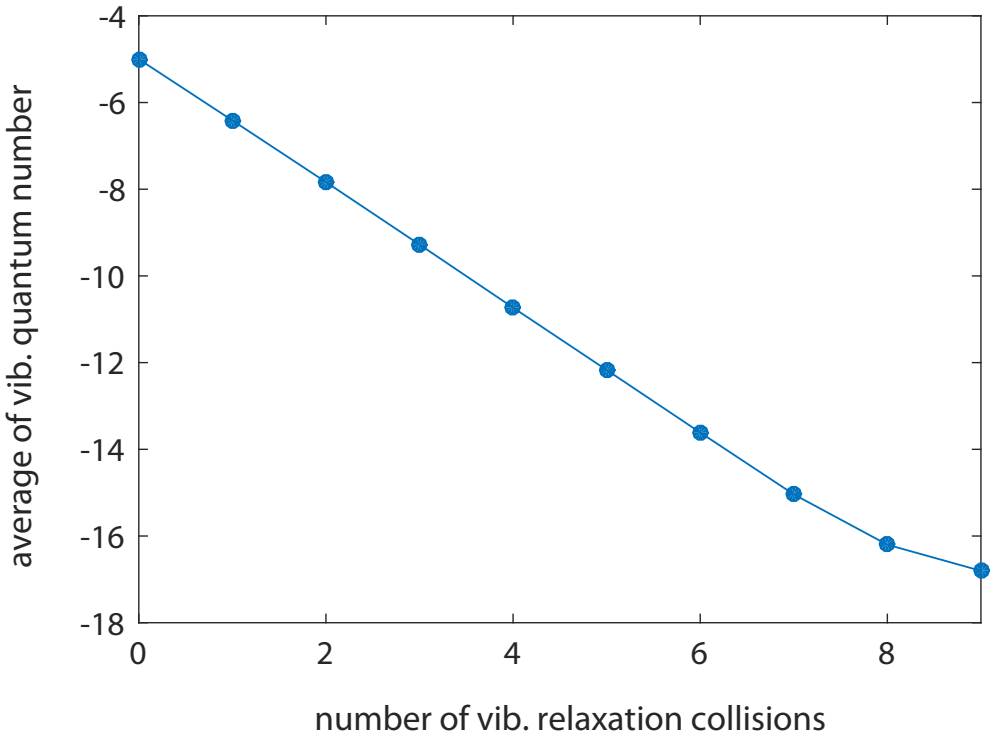

Figure B12: Average vibrational quantum number for a $BaRb^+$ ion as a function of the number of vibrational relaxation collisions with Rb atoms. The data points represent the results of MC calculations.

figure 5.2(a). The plots clearly show how initially the populations of the $(2)^1\Sigma^+$ and $(1)^3\Sigma^+$ states increase due to formation of the $BaRb^+$ ion via three-body recombination. At some point later these populations peak and decrease due to radiative relaxation to the ground state $(X)^1\Sigma^+$ and, in the presence of 1064 nm light, due to photodissociation. The calculations for the creation of either a hot Ba^+ or a Rb^+ ion via this photodissociation are given by the curves denoted by hot Ba^+ (1064) and Rb^+ (1064), respectively. Radiative relaxation leads at first to a growing population of the $(X)^1\Sigma^+$ ground state $BaRb^+$ molecule which, in secondary reactions, is converted into a Rb_2^+ or a Rb^+ ion. Here, we only consider the sum of the Rb_2^+ and Rb^+ populations, denoted Rb_2^+ / Rb^+. When the 1064 nm ODT is on, photodissociation is a dominant process for $(2)^1\Sigma^+$ and $(1)^3\Sigma^+$ molecules. Furthermore, the small fraction of molecules that relax to the ground state $(X)^1\Sigma^+$ are quickly removed in the trapped, dense atom cloud due to secondary reactions with Rb atoms. In contrast, when the ODT is off, almost the whole ion population is first converted into ground state $BaRb^+$ molecules, apart from a small fraction remaining in the state $(1)^3\Sigma^+$. A sizable fraction of the ground state molecules do not undergo sec-

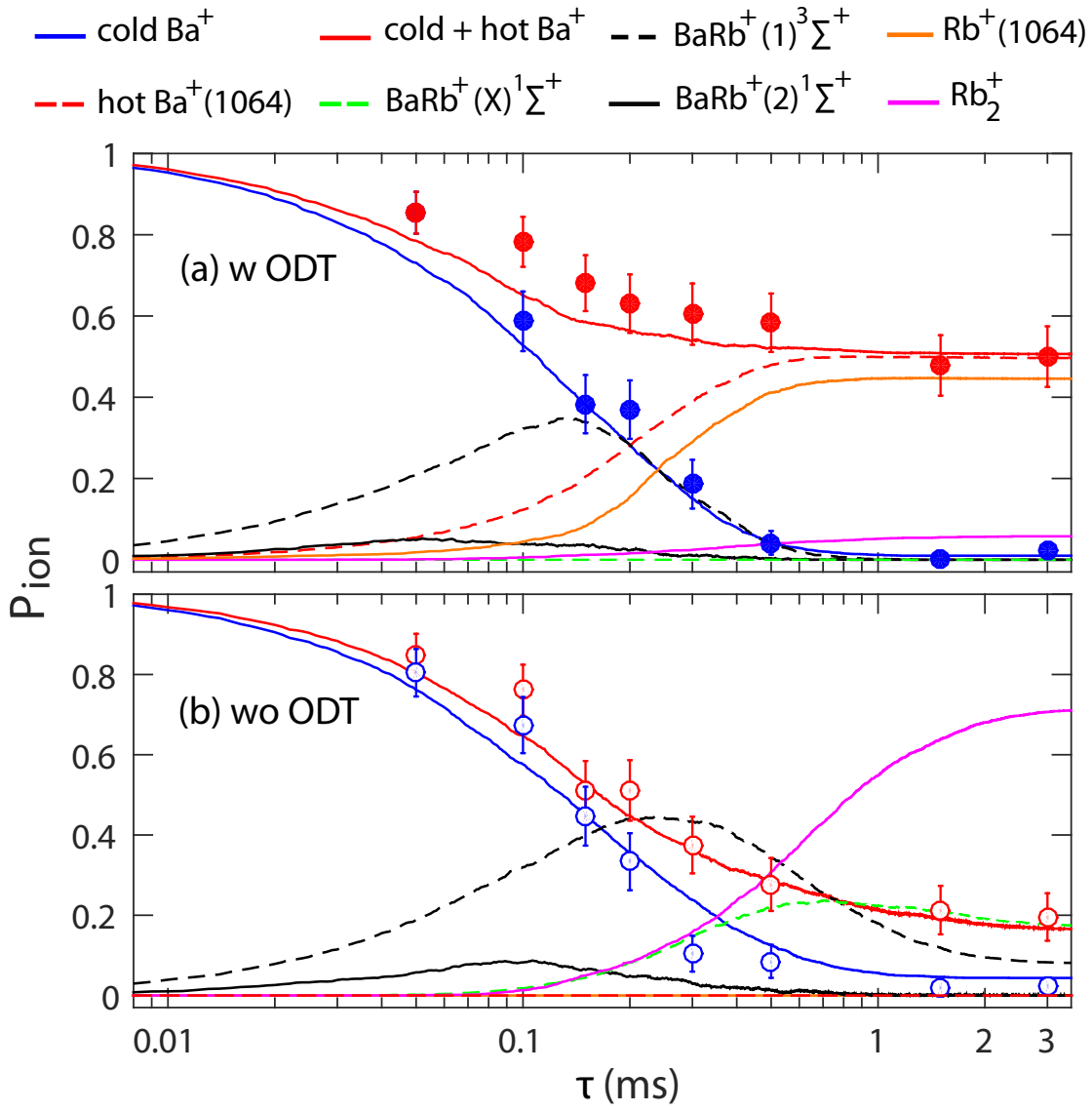

Figure B13: Calculations (lines) for ion signals together with measured data (filled and open circles) of figure 5.2(a). Shown are the probabilities for finding different ion states or species as given in the legend. In (a) the case with ODT is considered while in (b) the case without ODT is considered. "hot Ba^+(PD)" and "Rb^+(PD)" are populations due to photodissociation with 1064nm light. The population "Rb_2^+ / Rb^+" is due to secondary collisional reactions of $BaRb^+$ $(X)^1\Sigma^+$ molecules with Rb atoms.

ondary reactions and therefore persist, as the released Rb atom cloud quickly falls away. In order to describe the experimental signal for "cold+hot Ba^+" we add the populations for "cold Ba^+" and "hot Ba^+(1064)" as well as 70% of the population of

$BaRb^+$ molecules in the states $(X)^1\Sigma^+$ and $(2)^1\Sigma^+$. This last contribution is due to photodissociation of ground state molecules. The scenario is the following. During the imaging all $(2)^1\Sigma^+$ singlet molecules will relax to the ground state $(X)^1\Sigma^+$. The cooling lasers will then dissociate these and the previously produced $(X)^1\Sigma^+$ ground state molecules. This photodissociation generates in 70% (30%) of the cases a hot Ba^+ (Rb^+) ion, as discussed in section 5.8.

C Notes on reactive collisions of the Ba^+-Rb system

This section is a publication where I am second author. The first author is Artjom Krükow who has used this work as a main part of his PhD thesis (published by university of Ulm, 2016). The publication is inserted here because it is closely related to my own PhD topic.

Reactive two-body and three-body collisions of Ba^+ in ultracold Rb

Physical Review A **94**, 030701 (R) (2016)
Rapid Communication ©2016 American Physical Society

Artjom Krükow, Amir Mohammadi, Arne Härter and Johannes Hecker Denschlag

Institut für Quantenmaterie und Center for Integrated Quantum Science and Technology IQ^{ST}, Universität Ulm, 89069 Ulm, Germany

We analyze reactive collisions of a single ion in contact with an ultracold gas of Rb atoms at low three-body collision energies of 2.2(9) mK$\times k_B$. Mapping out the loss rate dependence on the Rb atom density we can discern two-body reactive collisions from three-body ones and determine both rate coefficients which are $k_2 = 3.1(6)(6) \times 10^{-13}\mathrm{cm}^3\mathrm{s}^{-1}$ and $k_3 = 1.04(4)(45) \times 10^{-24}\mathrm{cm}^6\mathrm{s}^{-1}$, respectively (statistical and systematic errors in parentheses). Thus, the measured ternary recombination dominates over binary reactions even at moderate atom densities of $n \approx 10^{12}\ \mathrm{cm}^{-3}$. The results for and Rb are representative for a wide range of cold ion-atom systems and can serve as guidance for the future development of the field of hybrid atom-ion research.

C1 Introduction

Cold atom-ion physics in hybrid traps is a young, developing field [71,156,157], which builds on the relatively long-range r^{-4} polarization potential between an atom and an ion. In general, this potential promises large cross sections and therefore strong interactions between particles. As a consequence, a number of interesting research proposals have been brought forward ranging from sympathetic cooling down to ultracold temperatures [158], to studying the physics of strongly correlated many-body systems, e.g., ultracold charge transport [45], novel many-body bound states [47] and strong-coupling polarons [46], quantum information processing [159], and quantum simulation [160]. Most of these ideas rely on interactions mediated by elastic atom-ion collisions, while inelastic collisions and chemical reactions are undesired as they represent a time limit for the suggested experiments. Therefore it is important to identify and investigate possible reactions and to eventually gain control over them. Inelastic processes can be divided up into classes such as two-body or three-body collisions. In general, binary collisions are dominant at low enough atomic densities, while ternary collisions will eventually take over with increasing density. This knowledge has been extensively applied in the field of ultracold neutral atoms by typically working with low enough atomic densities (e.g. smaller than about 10^{14}cm^{-3} for ^{87}Rb) in order to keep three-body losses negligible [161]. Considering the low-density limit, theoretical predictions for cold hybrid atom-ion systems have been focusing on binary inelastic/reactive atom-ion collisions (e.g. [59, 86]) which were discussed as the limiting factors for proposed atom-ion experiments [43, 158, 162, 163]. Along the same lines, measurements on atom-ion reactions in the low mK regime were, until recently, unanimously interpreted in terms of pure two-body decay [93, 100, 101, 104, 164, 165].

In this Rapid Communication we show, however, that in general the decay analysis requires the simultaneous consideration of both two- and three-body reactions. Our measurements reveal that at mK temperatures inelastic three-body collisions of the ion can dominate over its two-body reactions, even at moderate atomic densities down to $3\times10^{11}\text{cm}^{-3}$. Indeed, the main focus of this work lies on how to clearly distinguish two-body from three-body processes and extract the corresponding rate coefficients. One could in principle argue that in order to study only two-body reactions the atomic density simply needs to be lowered sufficiently. This is, however, not practical in standard set-ups with magnetic or dipole traps because the resulting reaction rate can be so small that the ion lifetime exceeds the atomic cloud lifetime. Alternatively, one could consider working with a magneto-optical trap (MOT) which

allows for both, low densities and long lifetimes due to continuous loading. However, in a MOT the reaction rate measurements of the ground-state atoms are swamped beneath a background of reactions of electronically excited atoms occurring at much higher rates.

For our investigations we use a heteronuclear combination of $Ba^+ + Rb$, where both two-body and three-body collisions lead to reactions and hence to ion loss in the experiment. This complements a recent experiment of ours with homonuclear $Rb^+ + Rb + Rb$ [109] for which reactive and inelastic two-body collisions are either forbidden or irrelevant. Furthermore, we note that in parallel to the work discussed here, we have studied the energy scaling of atom-ion three-body recombination [166].

We measure the density dependence of the reaction rate $\Gamma = k_2 n + k_3 n^2$ and extract the binary and ternary loss rate coefficients k_2 and k_3. Here, n is the peak atom density at the cloud center where the ion is located. For the analysis the evolution of $n(t)$ needs to be included, as the atom cloud is decaying during the time t due to elastic atom-ion collisions. We experimentally determine $n(t)$ by excluding experimental runs where the ion has undergone a reaction during the interaction time t in order to avoid systematic errors introduced by reactive collisions.

C2 Experimental setup

The experiments are performed in a hybrid apparatus that has already been described in detail elsewhere [48]. We prepare a single in a linear Paul trap and bring it into contact with an ultracold cloud of spin-polarized ($F = 1, m_F = -1$). The atoms are prepared at a separate location from which they are transported to the Paul trap and loaded into a far off-resonant crossed optical dipole trap. During the final preparation stage for the atoms, the cloud and the ion are separated by about 100 μm along the Paul trap axis to avoid unwanted atom-ion interactions. By ramping one endcap voltage of the linear Paul trap to its final value, we shift the ion into the center of the atom cloud within 10ms and start the atom-ion interaction. We use thermal atom clouds consisting of typically $N \approx 40-135\times10^3$ atoms at temperatures of $T \approx 330$nK with peak densities between $n \approx 6$ and $84 \times 10^{11}\,\mathrm{cm}^{-3}$. The Ba^+ ion is confined in a linear Paul trap which is operated at a frequency of 4.21 MHz with radial and axial trapping frequencies of $(\omega_r;\omega_a) = 2\pi\times(59.5;38.4)\,\mathrm{kHz}$. Single $^{138}Ba^+$ ions are loaded by isotope selective, resonant two-photon ionization. Using standard laser cooling techniques these are cooled to Doppler temperatures of $\approx 0.5\,\mathrm{mK}$. Before immersing the into the atomic bath we switch off the laser cooling, which guarantees that the ion is in the electronic ground state during the atom-ion interaction. The average

kinetic energy $\overline{E}_{\mathrm{kin}}$ of the ion is determined by the interplay of elastic collisions and the driven micromotion [61, 78, 164, 167, 168]. $\overline{E}_{\mathrm{kin}}$ is adjusted by tuning the excess micromotion of the ion and sets the average three-body collision energy $\overline{E}_{\mathrm{col}}$, through the relation $\overline{E}_{\mathrm{col}} \approx 0.55\ \overline{E}_{\mathrm{kin}}$ [166]. For the experiments discussed in the following we work either at an energy of $\overline{E}_{\mathrm{kin}} \approx 4$ or of 70 mK$\times k_{\mathrm{B}}$.

C3 Measuring and modeling the time dependent ion loss rate

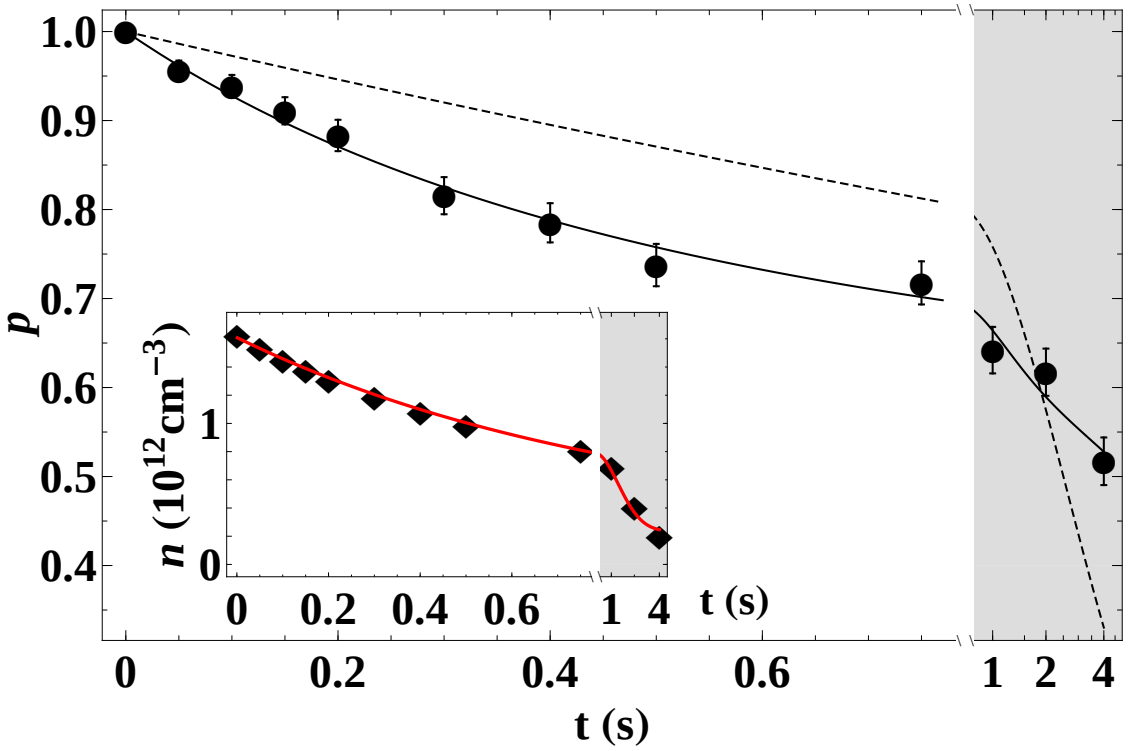

Figure C1: Probability p to detect the ion after the interaction time t with a Rb atom cloud at an average ion kinetic energy of $\overline{E}_{\mathrm{kin}} \approx 67\,\mathrm{mK}\times k_{\mathrm{B}}$. One data point is the average of the binary result over roughly 330 single-ion experiments. A fit (solid line) taking into account the decay of the atom density during the interaction reproduces this behavior while a simple exponential fit (dashed line) does not. The inset shows the corresponding atom density evolution, which is well described by an exponential decay with an offset (solid line). Note the time-scale change at 0.8 s, as indicated by the shaded background. All error bars represent the 1σ statistical uncertainty of the measurements.

We start our investigations by measuring the lifetime of a single in contact with a thermal cloud of Rb atoms. For this, we immerse the ion ($\overline{E}_{kin} \approx 67\,\mathrm{mK}\times k_{\mathrm{B}}$) into

the atom cloud (density $n \approx 16 \times 10^{11}\,\mathrm{cm}^{-3}$) for various periods of time t. After the interaction, we check if the is still present by switching on the laser cooling for 100 ms and collecting its fluorescence on a EMCCD camera. If no is detected, we conclude that a reaction must have taken place. If we apply additional laser cooling with a red detuning of 2 GHz for several seconds, typically 50% of the initially undetected ions can be recovered. These ions have gained high kinetic energies in a chemical reaction, which will be discussed later. Figure C1 shows the measured probability p to detect the ion as a function of the interaction time t (please note the time scale change after 0.8 s). We model the decay using the rate equation $\dot{p} = -\Gamma(t) \cdot p$, with the loss rate $\Gamma(t) = k_2 \cdot n(t) + k_3 \cdot n(t)^2$, where $n(t)$ is the time-dependent atom density at the location of the ion. Integrating the equation yields

$$p(t) = \exp(-\int_0^t \Gamma(t')dt'). \tag{C1}$$

A constant density $n(t)$ would lead to an exponential decay, $p(t) = \exp(-\Gamma t)$, which does not describe the observed loss very well (Fig. C1, dashed line). As the inset of Fig. C1 shows, the density decreases during the interaction time. This is because elastic atom-ion collisions either remove atoms from the shallow atom trap or heat up the atomic ensemble. If we take into account the decay of $n(t)$, a fit of Eq (C1) (solid line) describes the data very well.

C4 Accessing the atom density evolution

In other words, for a proper description of the ion loss Γ and to determine the rate constants k_2 and k_3, the evolution of the density $n(t)$ has to be accurately determined. This, however, is somewhat involved and will be discussed in the following.

To determine $n(t)$, we measure the remaining atom number N and temperature T of the cloud via absorption imaging after 15 ms time of flight. Figure C2(a) shows histograms of the atom number distributions for various interaction times t. Initially the distribution is Gaussian. As time goes on, elastic atom-ion collisions shift this distribution towards lower atom numbers. In addition, a broad tail develops. This tail can be explained as a consequence of reactive atom-ion collisions that release substantial amounts of energy which eject the product ion out of the atom cloud onto a large orbit trajectory in the Paul trap. This is consistent with the recovery of hot ions when additional far red-detuned laser cooling is applied, as mentioned in the previous paragraph. Although two-body and three-body reactions at mK temperatures are predicted to dominantly produce translationally cold molecular

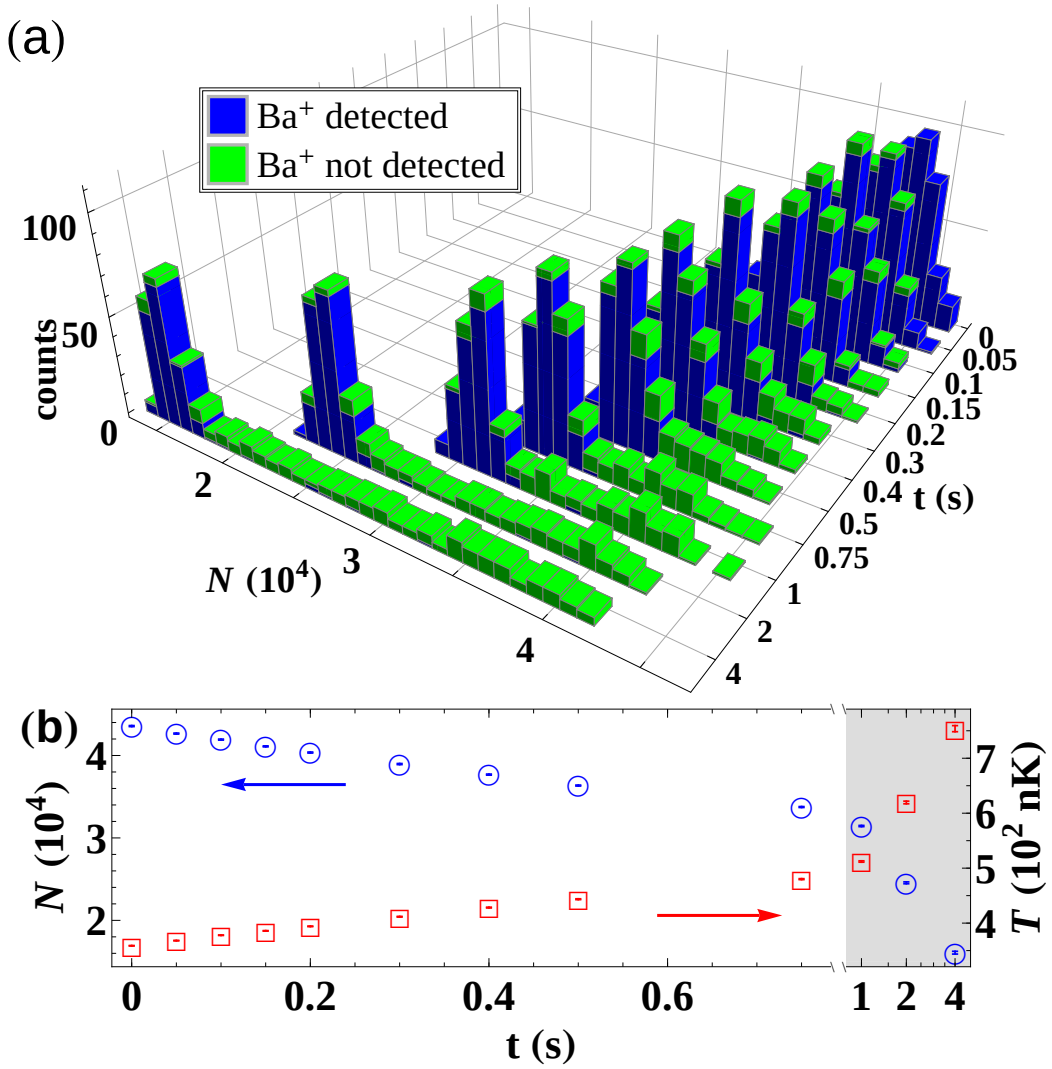

Figure C2: (a) Histogram of the atom numbers N belonging to the measurement in Fig. C1. A Gaussian atom number distribution develops a broad tail with increasing interaction times. Experimental runs where the ion was detected (not detected) after the interaction are marked in blue (green), respectively. Atom numbers within the tail (Gaussian peak) of the distribution correspond to runs with (without) a reactive collision, respectively. (b) Average atom number N (circles) and temperature T (squares) over all runs without reactions, corresponding to the blue colored counts in (a).

$BaRb^+$ ions [110, 169], additional kinetic energy can be released in fast secondary processes such as photo dissociation or collisional relaxation. Once the ion is on the large orbit, the atom-ion collision rate is significantly reduced, essentially stopping the continuous atom loss [109]. From Fig. C2(a) we find that the counts in the tail almost exclusively correspond to experimental runs where a reaction with occurred (green color), whereas the counts in the Gaussian dominantly correspond to runs without reactions (blue color).

For our analysis we only consider system trajectories without reactions, making sure that the ion has been constantly exposed to the central density $n(t)$. The average atom number N and temperature T of these post selected trajectories are plotted in Fig. C2(b). We then calculate the peak atom density (shown in Fig. C1 inset) $n = (\frac{m}{2\pi k_\mathrm{B}})^{3/2} \cdot \frac{\omega_x \omega_y \omega_z N}{T^{3/2}}$, with the mass m, using separately measured trap frequencies $(\omega_x, \omega_y, \omega_z)$ of the atom dipole trap. From these sampling points we extract the time-dependent density $n(t)$.

C5 Extracting the binary and ternary reaction rate constants

We are now ready to quantitatively analyze the reaction rate and to extract binary and ternary reaction rate constants. In order to obtain a high accuracy (and as a check for consistency) we perform lifetime measurements at 10 different initial peak densities [Fig. C3(a)]. Atom clouds with different densities are prepared by varying the trap frequencies and the atom number but keeping the atom temperature T at a constant value of $T \approx 330\text{nK}$. This temperature was chosen in order to be sufficiently above the critical temperature T_c for Bose-Einstein condensation and to have negligible losses due to evaporative cooling. The trap depths are between 5 to 10 $\mu\text{K}\times k_\text{B}$ resulting in trap frequencies of $(\omega_x, \omega_y, \omega_z) \approx 2\pi\times(16 \text{ to } 27; 97 \text{ to } 151; 107 \text{ to } 161)\text{Hz}$. The mean ion kinetic energy is 4.0 (1.6) mK $\times k_\text{B}$, as determined in [166]. The densities between $n \approx 6$ and 22×10^{11} cm^{-3} are prepared with $N \approx 40 \times 10^3$ atoms, while densities between $n \approx 24$ and 84×10^{11} cm^{-3} are prepared with $N \approx 135 \times 10^3$ atoms.

In a first simple analysis we do not include the density evolution and fit exponential decays (dashed lines) to each data set in Fig. C3(a). The resulting loss rates Γ are then plotted as a function of their respective initial atom densities $n(t = 0)$ in Fig. C3(b). By fitting $\Gamma = k_2 \cdot n + k_3 \cdot n^2$ (blue dashed line) we obtain a quasi pure quadratic density dependence, where $k_3 = 1.03(2)(45) \times 10^{-24}\text{cm}^6\text{s}^{-1}$ and k_2 is consistent with zero. For comparison, if we try to describe the data only by two-body reactions, $\Gamma \propto n$, no agreement is found (red dashed line).

Now, we perform a more rigorous analysis, where we account for the density decay during the interaction time, which can be as much as 20 % for the experimental runs in Fig. C3. This will enable us to also extract a reliable k_2 rate constant from the data. With the previously described method we determine $n(t)$ for each lifetime curve. We then fit Eq. (C1) to all of the 10 measured decays in Fig. C3(a) (solid lines) simultaneously, with only two free fit parameters, the binary and ternary rate coefficients k_2 and k_3, which amount to $k_2 = 3.1(6)(6) \times 10^{-13}\text{cm}^3\text{s}^{-1}$ and $k_3 = 1.04(4)(45) \times 10^{-24}\text{cm}^6\text{s}^{-1}$. The first parentheses denotes the $1\,\sigma$ statistical uncertainty of the fitted values. The second one gives the $1\,\sigma$ systematic error due to the atom density uncertainty of 20 %, which translates linearly into k_2 and quadratically to k_3.

Notably, both approaches yield the same k_3 within their uncertainties, but only the latter provides a non zero k_2, which emphasizes the necessity to include the atom cloud decay. We plot $\Gamma = k_2 \cdot n + k_3 \cdot n^2$, using the extracted k_2 and k_3 coefficients

in Fig. C3(b) (green curve). Even at low densities $n < 10^{12}\mathrm{cm}^{-3}$ the green curve deviates only slightly from the pure three-body loss (blue dashed line), highlighting the small contribution of binary reactions to the total ion loss.

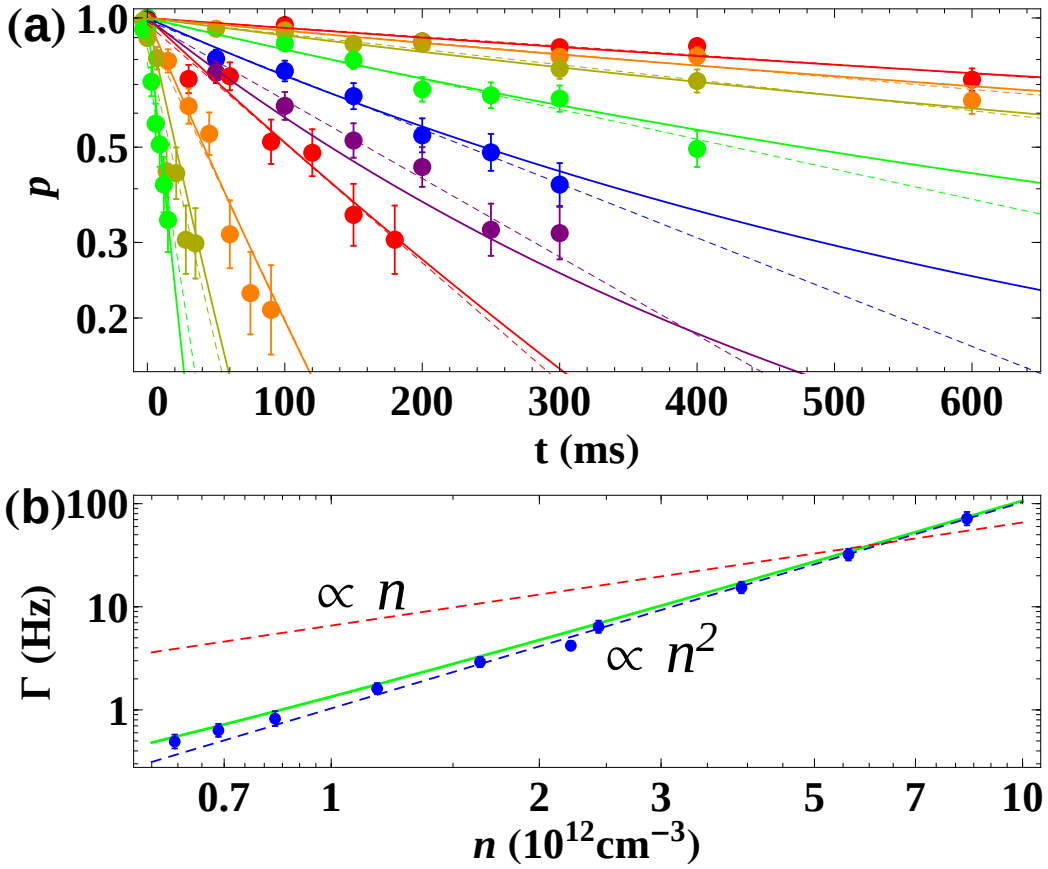

Figure C3: (color online) (a) Logarithmic plot of p as a function of the interaction time t for 10 different initial atom peak densities. Each data point corresponds to an average of roughly 100 single ion experiments. The dashed curves are simple exponential fits, while the solid curves originate from a simultaneous fit of Eq. C1 to the full data set with two free parameters, the two-body rate coefficient k_2 and the three-body rate coefficient k_3 (see text for details). (b) Double-logarithmic plot of the Ba^+ loss rates Γ extracted from an exponential fit to each individual data set in (a) over the respective initial peak densities (solid circles). A fit of the form $\Gamma = k_2 \cdot n + k_3 \cdot n^2$ to the loss rates yields a pure quadratic density dependence (blue dashed curve). For comparison, this function was also plotted using k_2 and k_3 from (a) (green curve). A pure linear dependence ($\Gamma \propto n$) does not describe the data (red dashed curve).

C6 Comparison to previous results

We now compare the obtained rate coefficients to the results of other groups in the field. Our extracted two-body charge-transfer rate coefficient k_2 for the + Rb system is compatible with a MOT measurement from Ref. [110] where an upper bound of $k_2 < 5 \times 10^{-13}\,\mathrm{cm^3 s^{-1}}$ is given for ground state charge-transfer. An *ab-initio* calculation within [110] predicts $k_2 \approx 1 \times 10^{-14}\,\mathrm{cm^3 s^{-1}}$ which is a factor of 30 smaller compared to our present k_2. A possible explanation for this large discrepancy is an additional two-body loss channel that might appear in our experiment. Indeed, calculated Ba^+ + Rb molecular potential energy curves (see, e.g., Ref. [110]) indicate that the 1064 nm dipole laser can near-resonantly photo-excite a colliding atom-ion pair to a repulsive molecular potential energy curve. For the potential curves that correlate with ionized Rb^+ and electronically excited neutral Ba, this process is experimentally indistinguishable from charge transfer.

We note that the three-body rate coefficient k_3, determined in this work for + Rb + Rb is of similar magnitude as the one for + Rb + Rb [109], which is only by a factor of 3 smaller. This can be understood as a consequence of the same long-range atom-ion interaction potential of both systems, as it only depends on the polarizability of the Rb atom. Indeed, a theoretical classical trajectory study predicted very similar three-body cross sections for and [169]. Furthermore, since in cold reactive ternary collisions typically large, weakly bound molecules should be formed [166], the short-range details of the molecular interaction potential do not contribute. This suggests a universal behavior of cold atom-atom-ion three-body recombination, leading to similar reaction-rate coefficients for a variety of hybrid atom-ion systems.

C7 Conclusion

In conclusion, we have studied reactive collisions of a cold, single ion in contact with an ultracold cloud of Rb atoms. Mapping out the loss dependence on the Rb atom density enabled us to extract both the binary (k_2) and ternary (k_3) reaction-rate coefficients at $\mathrm{mK}\times k_\mathrm{B}$ ion energies. The Ba^+ + Rb + Rb three-body rate coefficient k_3 is comparatively large, about four orders of magnitude larger than the one for ultracold neutral Rb + Rb + Rb collisions [170]. Moreover, it dominates over the two-body loss down to comparatively low densities of $k_2/k_3 \approx 3 \times 10^{11}\mathrm{cm^{-3}}$. If working with degenerate quantum gases such as Bose-Einstein condensates with typical densities around $10^{14}\,\mathrm{cm^{-3}}$, three-body recombination will occur on the sub-

ms time scale, limiting the time for atom-ion experiments. As shown in parallel work of ours [166], this time scale gets even shorter when lowering the collision energy E_{col}, as k_3 scales as $k_3 \propto E_{\mathrm{col}}^{-3/4}$. In view of the number of proposed experiments where reactive collisions are unwanted, we expect a future demand for schemes to suppress three-body reactions besides the existing ones for two-body reactions [43].

We thank Olivier Dulieu, Jesús Pérez-Ríos, and Chris H. Greene for fruitful discussions. This work was supported by the German Research Foundation DFG within the SFB/TRR21. A.K. acknowledges support from the Carl Zeiss Foundation.

D Notes on Ba^+-Rb-Rb three-body Recombination

This section is a publication where I am second author. The first author is Artjom Krükow who has used this work as a main part of his PhD thesis (published by university of Ulm, 2016). The publication is inserted here because it is closely related to my own PhD topic.

Energy Scaling of Cold Atom-atom-ion Three-body Recombination

Physical Review Letters **116**, 193201 (2016)

Artjom Krükow, Amir Mohammadi, Arne Härter and Johannes Hecker Denschlag

Institut für Quantenmaterie und Center for Integrated Quantum Science and Technology IQ^{ST}, Universität Ulm, 89069 Ulm, Germany

Jesús Pérez-Ríos and Chris H. Greene

Department of Physics and Astronomy, Purdue University, West Lafayette, Indiana 47907, USA

We study three-body recombination of + Rb + Rb in the mK regime where a single $^{138}Ba^{+}$ ion in a Paul trap is immersed into a cloud of ultracold ^{87}Rb atoms. We measure the energy dependence of the three-body rate coefficient k_3 and compare the results to the theoretical prediction, $k_3 \propto E_{\mathrm{col}}^{-3/4}$ where E_{col} is the collision energy. We find agreement if we assume that the nonthermal ion energy distribution is determined by at least two different micromotion induced energy scales. Furthermore, using classical trajectory calculations we predict how the median binding energy of the formed molecules scales with the collision energy. Our studies give new insights into the kinetics of an ion immersed in an ultracold atom cloud and yield important prospects for atom-ion experiments targeting the s-wave regime.

D1 Introduction

When three atoms collide, a diatomic molecule can form in a three-body recombination (TBR) process. In cold neutral atomic gases, TBR was investigated for spin-polarized hydrogen as well as alkalis (see e.g. [170–172]). In the context of Bose-Einstein condensation, TBR plays a crucial role as a main loss mechanism. By now, the scaling of TBR as a function of collision energy and scattering lengths in *neutral* ultracold gases has been investigated in detail [173]. When considering TBR in atom-ion systems, one can expect three-body interactions to be more pronounced due to the underlying longer-range r^{-4} polarization potential. Energy scaling of TBR in charged gases was studied at temperatures down to a few K, especially for hydrogen and helium due to their relevance in plasmas and astrophysics (e.g. [174, 175]). Depending on the studied temperature range a variety of power laws was found but not a common threshold law. The recent development of novel hybrid traps for both laser cooled atoms and ions has opened the possibility to investigate cold atom-ion interactions and chemical reactions in the mK regime and below. First experiments in such setups studied elastic and reactive two-body collisions (e.g. [39, 40, 93, 100, 101, 163, 176, 177]). In accordance with the well-known Langevin theory, the corresponding reactive rates were measured to be independent of the collision energy [93, 164]. Very recently we predicted a theoretical threshold law on the scaling properties for cold atom-atom-ion three-body collisions [169]. Understanding the scaling of reaction rates with quantities such as the collision energy is crucial for fundamentally understanding TBR and for the prospects of the experimental realization of ultracold s-wave atom-ion collisions. Furthermore, as we will show here, studying TBR allows for insights into the kinetics of an ion immersed in a cloud of atoms. Experimentally, TBR in the mK regime was recently observed for

$Rb^+ + Rb + Rb$ [109] and $+ Rb + Rb$ [178]. In the experiments TBR was already dominating over two-body reactions even for moderate atomic densities of $10^{12}\,\mathrm{cm}^{-3}$.

This Letter reports on the combined theoretical and experimental investigation of the energy scaling of three-body atom-atom-ion collisions in the mK regime. We measure the TBR rate coefficient $\overline{k}_3$ of in an ultracold Rb cloud as a function of the mean collision energy of the ion, $\overline{E}_{\mathrm{col}}$, which we control via the excess micromotion (eMM) of the Paul trap. $\overline{k}_3$ is formally distinguished from k_3 which is the TBR rate coefficient for a precise collision energy E_{col} in the center-of-mass frame. By averaging k_3 over the ion energy distribution $\overline{k}_3$ is obtained. We calculate k_3 using classical trajectory calculations (CTC) [169, 179] and derive its energy scaling, $k_3 \propto E_{\mathrm{col}}^{-3/4}$. Agreement is found between theory and experiment if we assume that the energy distribution of the ion depends on multiple energy scales due to various sources of excess micromotion. Besides the prediction of k_3, the CTC calculations also provide the binding energy distribution of the formed molecules and the scaling properties of these distributions when the collision energy is varied.

D2 Experimental Setup

The experiments are performed in a hybrid apparatus that has already been described in detail elsewhere [48]. After loading a single $^{138}Ba^+$ ion by isotope selective, resonant two-photon ionization it is stored in a linear Paul trap driven at a frequency of 4.21MHz with radial and axial trapping frequencies of $(\omega_r;\omega_a) = 2\pi\times(59.5;38.4)$kHz, respectively. There, it is laser cooled to Doppler temperatures of $\approx 0.5\,\mathrm{mK}$. In order to perform our experiments in the electronic ground state, we switch off the cooling and repumper light, before immersing the ion into the ultracold atomic cloud.

Once in the cloud, there is a complicated interplay of elastic two-body atom-ion collisions and the driven micromotion of the Paul trap. This interplay leads to a non-Maxwell-Boltzmann distribution of the ion's kinetic energy E_{kin} [78,164,167,168] with an equilibration time on the ms time scale [2]. The average kinetic energy $\overline{E}_{\mathrm{kin}}$ of the ion in the atom cloud is then determined by the available energy sources for the ion, such as the eMM energy [164]. In our experiment we can adjust $\overline{E}_{\mathrm{kin}}$ by controlling one part of the eMM energy, E_{fMM}, which is set via static electric fields. Concretely, we can write $\overline{E}_{\mathrm{kin}} = c_{dyn}(E_{\mathrm{fMM}} + E_{\mathrm{min}})$, where the offset energy E_{min} contains all other energy contributions, *e.g.* phase micromotion (ϕMM) [61] or residual collisional effects [78, 168]. The proportionality factor $c_{dyn} \approx 5.0$, which depends on the atom-

[2] The equilibration time can be estimated from the Langevin collision rate which at our given density is about $4\,\mathrm{ms}^{-1}$.

ion mass ratio and the trap parameters, is extracted from a MC calculation similar to [82]. We can tune E_{fMM} accurately between $5\mu\mathrm{K}\times$ and $100\mathrm{mK}\times$. E_{min}, on the other hand, is not known precisely. From independent measurements and MC calculations based on the scaling of elastic atom-ion collisions, we estimate E_{min} to be in the range between 200 and 800 $\mu\mathrm{K}\times$.

The cloud consists of $N \approx 1.2 \times 10^5$ ^{87}Rb atoms at a temperature of $T_{\mathrm{at}} \approx 700\,\mathrm{nK}$ with a peak density of $n \approx 19 \times 10^{11}\ \mathrm{cm}^{-3}$. It is cigar shaped with a radial and axial size of roughly 10 μm and 50 μm, respectively. The atoms are spin polarized ($F = 1, m_F = -1$) and confined in a far off-resonant crossed optical dipole trap at a wavelength of 1064 nm with a trap depth of $\approx 10\,\mu\mathrm{K}\times$. We shift the ion into the cloud over a distance of 120 μm within 2 ms by changing the endcap voltage of the linear ion trap. After an interaction time of $\tau = 300\,\mathrm{ms}$, during which the Ba^+ ion is typically lost with a probability of up to 65 %, we separate the two traps again and detect whether the Ba^+ ion is still present. For this, we shine a laser cooling beam focused to a waist of 20 μm through the Paul trap center and collect the possible fluorescence on a EMCCD camera for 100 ms. If no is detected, we conclude that a reaction must have taken place during τ [3].

D3 Energy dependent reactions

Repeating the single ion experiment roughly 170 times we extract the probability p that is still present. For the given experimental settings the ion loss is well described by an exponential decay of the form $p = \exp(-\Gamma\tau)$. This can be seen in the inset of Fig. D1, where we plot p as a function of interaction time τ measured at $E_{\mathrm{fMM}} \approx 8\,\mu\mathrm{K}$. Figure D1 plots the loss rate Γ as a function of E_{fMM}. A Ba^+ ion in our experiment is lost either by a two-body charge transfer or by a three-body event [178]. The corresponding loss rate Γ of the ion is $\Gamma = -nk_2 - n^2\overline{k}_3$. The charge transfer rate coefficient k_2 has been previously measured for + Rb, $k_2 = 3.1(6)(6) \times 10^{-13}\mathrm{cm}^3/\mathrm{s}$ (statistical and systematic errors in parentheses) [178] (see also [101, 110]), and contributes less than $1\,\mathrm{s}^{-1}$ to the loss rate Γ for the given atomic density. Also, it has been verified that k_2 is energy independent [93, 100, 164], consistent with Langevin theory. By subtracting this constant k_2 loss from Γ and dividing by the (constant) density n^2 we obtain $\overline{k}_3$ (see Figs. 1 and 3b). Clearly, $\overline{k}_3$ is energy

[3] We note that our detection scheme cannot detect a reaction if the final product (e.g. after a secondary process) is again a cold Ba^+ ion. From parallel experiments where we investigate the reaction products, however, we have no evidence for such a reaction outcome. In fact, our present work shows good agreement between theory and experiment if we assume that a reaction channel producing cold Ba^+ ions is negligible.

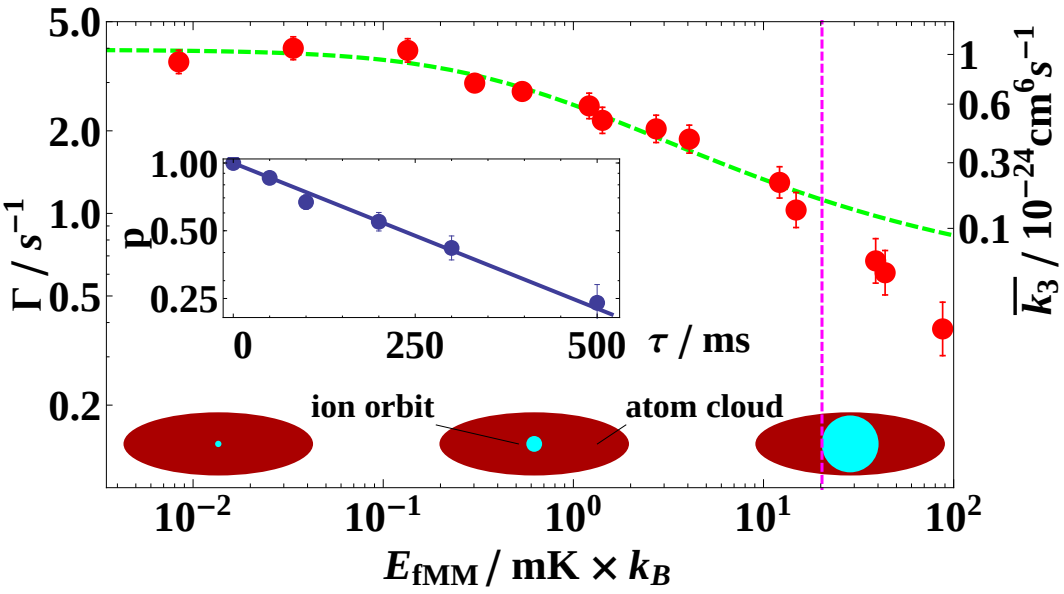

Figure D1: Double-logarithmic plot of the measured loss rate Γ for as a function of the tuned eMM energy E_{fMM}. Red circles are the experimental data; the curve represents a fit of Eq. (1) (see text for details). The corresponding values of $\overline{k}_3$ are indicated on the right-hand side. The inset is the Logarithmic plot of the decay curve of the ion. p is the probability to recover after interacting with Rb. The straight line is an exponential fit to the data. The sketch shows the ion orbit in the atom cloud. With increasing ion energy its orbit becomes comparable to the atom cloud size.

dependent. As we discuss later, we expect a scaling of k_3 with a power law, $k_3 \propto E_{\mathrm{col}}^{\alpha}$. Neglecting the atom motion due to ultracold temperatures we can express E_{col} in terms of the ion kinetic energy E_{kin}, $E_{\mathrm{col}} = (1 - \frac{m_{\mathrm{Ba}}}{m_{\mathrm{Ba}}+2m_{\mathrm{Rb}}})E_{\mathrm{kin}}$. We attempt to describe the scaling of the measured $\overline{k}_3$ with a power law $\overline{k}_3 \propto \overline{E}_{\mathrm{kin}}^{\alpha}$ by fitting the expression

$$\overline{k}_3 = \overline{k}_{3,\mathrm{min}} \left[(E_{\mathrm{fMM}} + E_{\mathrm{min}})/E_{\mathrm{min}}\right]^{\alpha} \tag{D1}$$

to the data. Here, E_{min} and α are free parameters. The constant $\overline{k}_{3,\mathrm{min}} = 1.04(4)(45)\times 10^{-24}\mathrm{cm}^6/\mathrm{s}$ is $\overline{k}_3$ at $E_{\mathrm{fMM}} = 0$ and was determined in a parallel study [178]. For the fit we discard data points above $E_{\mathrm{fMM}} > 20\,\mathrm{mK}\times$, as for such energies, the ion is not localized well enough in the center of the cloud. It probes areas of the atomic cloud at lower densities, hence decreasing the observed loss rate (see sketch in Fig. 1). The fit yields $\alpha = -0.46(9)$ and $E_{\mathrm{min}} = 410(180)\,\mu\mathrm{K}\times$ (green dashed line in Fig. D1), with the errors denoting a 1σ statistical uncertainty of the fitted values. Interestingly, in our previous study of TBR of + Rb + Rb [109] we observed a similar scaling exponent of $\alpha = -0.43$.

D4 Theoretical approach

We now turn to investigate the scaling of TBR theoretically with a CTC formalism. A classical treatment of the collision dynamics is appropriate, since the experiments described here in general involve much higher energies than the threshold energy of $\sim 50\,\mathrm{nK}\times$ for entering the s-wave regime of Ba^+-Rb. We have adapted a recently developed method for the calculation of three-body recombination cross sections based on classical trajectories [169,179] for the study of atom-atom-ion recombination. The method employed relies on mapping the three-body problem into a six-dimensional configuration space, described in hyperspherical coordinates, after separating out the center-of-mass motion [179]. Since the kinetic energy of the ion is typically several orders of magnitude higher than the temperature of the ultracold neutral atoms we fix one of the hyperangles associated to the ratio of the atom-ion versus the atom-atom initial momentum, guaranteeing that in the center-of-mass coordinate system 95 % of the collision energy E_{col} is along the direction of the ion. In the classical trajectory calculations only Rb-Rb collisions in triplet states are considered and spin flip transitions are neglected. For the Rb-Rb pair interaction we employ the $a^3\Sigma_u^+$ potential of Strauss *et al.* [128]. On the other hand, the Ba^+-Rb interaction potential is taken to be $-C_4(1-(r_m/r)^4/2)/r^4$, where $C_4 = 160$ a.u. denotes the experimental long-range value of the interaction and r_m represents the position of the minimum of the potential, taken from Ref. [158].

The TBR rate for $Ba^+ + Rb + Rb$ has been computed by running 10^5 trajectories per collision energy. We checked that during the simulation the total energy and angular momentum are conserved up to the fifth decimal place. Details about the numerical method employed to solve Hamilton's equations of motion, in conjunction with the sampling of the initial conditions, can be found in [179]. Figure D2a shows a three-body trajectory that results in a recombination event with a collision energy of $100\ \mu\mathrm{K}\times$. This particular trajectory leads to large size ($\sim 800\ \mathrm{a_0}$), very weakly-bound molecular ion. Counting the fraction of trajectories that lead to molecule formation we can extract the TBR rate coefficient k_3 for $Ba^+ + Rb + Rb$. Figure D2b plots k_3 as a function of collision energy E_{col}. We compare these CTC calculations (diamonds) with an analytically derived scaling law [169] where $k_3 \propto E_{\mathrm{col}}^{-3/4}$ (dashed line in Fig. D2b and find very good agreement.

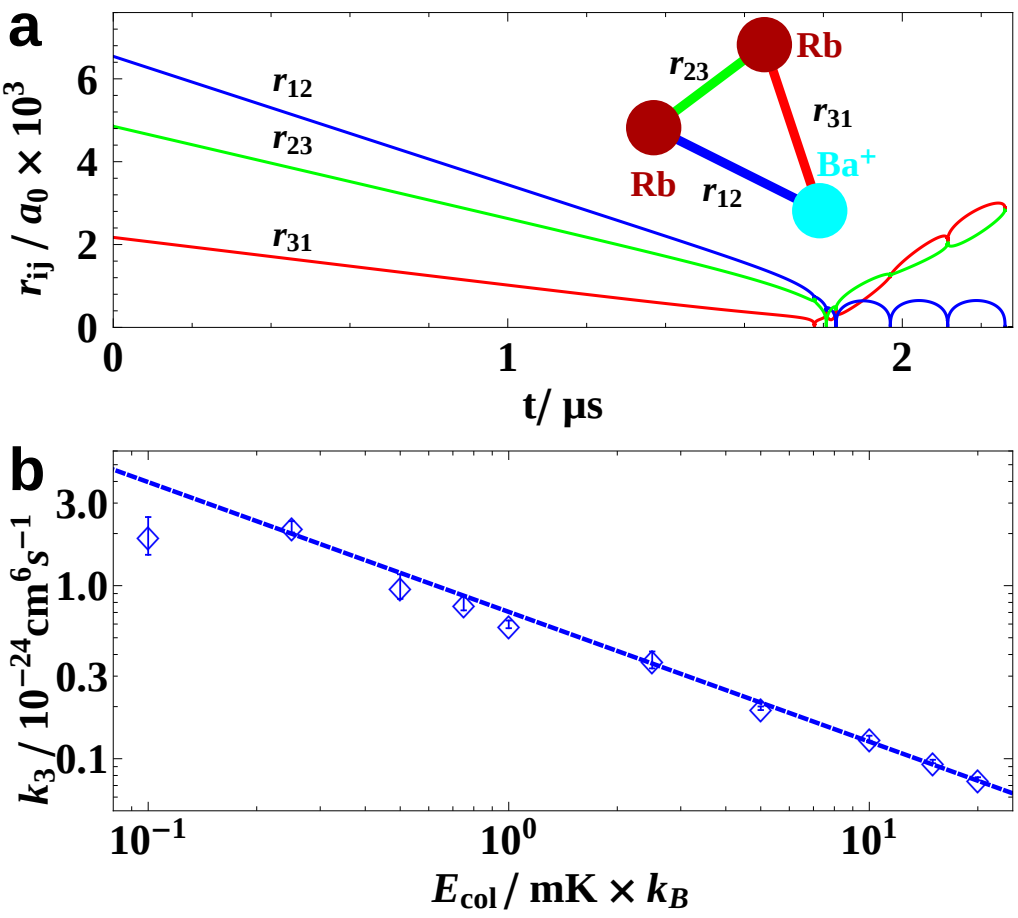

Figure D2: (a) A typical trajectory at a collision energy of 100 μK× associated with the three-body collision $Ba^+ + Rb + Rb$ that leads to the formation of $BaRb^+$. We show the distances r_{ij} between the particles as indicated in the sketch. (b) Double log plot of k_3 obtained with CTC for $Ba^+ + Rb + Rb$ as a function of the collision energy E_{col} (circles). The straight line shows the analytically predicted power law dependence $k_3 \propto E_{col}^{-3/4}$.

D5 Comparing experiment to theory

Strikingly, the theory prediction of $\alpha = -0.75$ does not seem to agree well with the experimentally observed value of $\alpha = -0.46(9)$ from the fit of Eq. (D1) to our data. We explain this discrepancy as follows. In contrast to the theoretical approach where k_3 is determined for a precisely defined collision energy E_{col}, in the experiments we observe $\overline{k}_3$, an average over a distribution $P(E_{col}, \{E_i^S\})$ of collision energies, calculated as

$$\overline{k}_3(\{E_i^S\}) = \int k_3(E_{col})\ P(E_{col}, \{E_i^S\})\ dE_{col}. \tag{D2}$$

Here, $\{E_i^S\}$ is a list of the relevant energy scales that determine the distribution, such as the experimentally tuned E_{fMM} or $E_{\phi\mathrm{MM}}$. We extract these distributions with a MC calculation based on [82]. If only a single scale E_1^S is present, the energy distributions can be expressed as functions of the ratio E_{col}/E_1^S,

$$P(E_{\mathrm{col}}, E_1^S)dE_{\mathrm{col}} = \tilde{P}(E_{\mathrm{col}}/E_1^S)dE_{\mathrm{col}}/E_1^S. \tag{D3}$$

Figure D3a shows three calculated distributions each with its own scale E_1^S. The distributions $P(E_{\mathrm{col}}, E_{\mathrm{fMM}})$ for $E_{\mathrm{fMM}} = 1$ mK (green) and 20 mK (red) have the exact same shape, a consequence of Eq. (D3). The third distribution $P(E_{\mathrm{col}}, E_{\phi\mathrm{MM}} = 1\,\mathrm{mK})$ (blue), generated with a phase micromotion has a somewhat different shape. Using Eq. (D2) one can show which distributions which satisfy Eq. (D3) translate the power law $k_3 \propto E_{\mathrm{col}}^{-3/4}$ into $\overline{k}_3 \propto (E_1^S)^{-3/4}$. In our experiment, however, where at least two energy scales, E_{fMM} and E_{min} occur, this translation of the scaling breaks down and Eq. (D1) cannot be used in the data analysis anymore. Instead, we calculate $\overline{k}_3$ with Eq. (D2) to directly compare theory and experiment. The choice and magnitude of E_{min} is the only free model parameter. Here, we assume that E_{min} is entirely determined by phase micromotion, $E_{\mathrm{min}} = E_{\phi\mathrm{MM}}$. The phase micromotion is chosen to be shared equally between both pairs of opposing radio frequency (rf) driven electrodes [61]. Figure D3b shows the experimental $\overline{k}_3$ (full circles), together with the calculation (blue solid line) with $E_{\phi\mathrm{MM}} = 790\,\mu\mathrm{K}$[4]. The shape of the theory curve describes the experimental data quite well, apart from an overall factor of about 1.1 (see blue and red solid lines). In general, the overall magnitude and energy dependence of $\overline{k}_3$ is reproduced by the presented *ab initio* CTC treatment down to the mK Regime, which is remarkable as E_{min} is the only free parameter.

D6 Binding energy distribution

We now turn to briefly discuss the molecular products after TBR. In a previous study of TBR for He, it was suggested that the binding energy of the products is correlated with the collision energy [179]. We find again the same behavior for TBR of an ion with two atoms. Figure D4a shows two logarithmically binned histograms of molecular binding energies after TBR. The maximum of each histogram can be considered the typical binding energy and is shown in Fig. D4b as a function of the

[4]Such a phase micromotion can be caused by a relative length difference of $\Delta l/l \approx 10^{-3}$ between the cables supplying opposing rf electrodes, which is well within the tolerances of our setup.

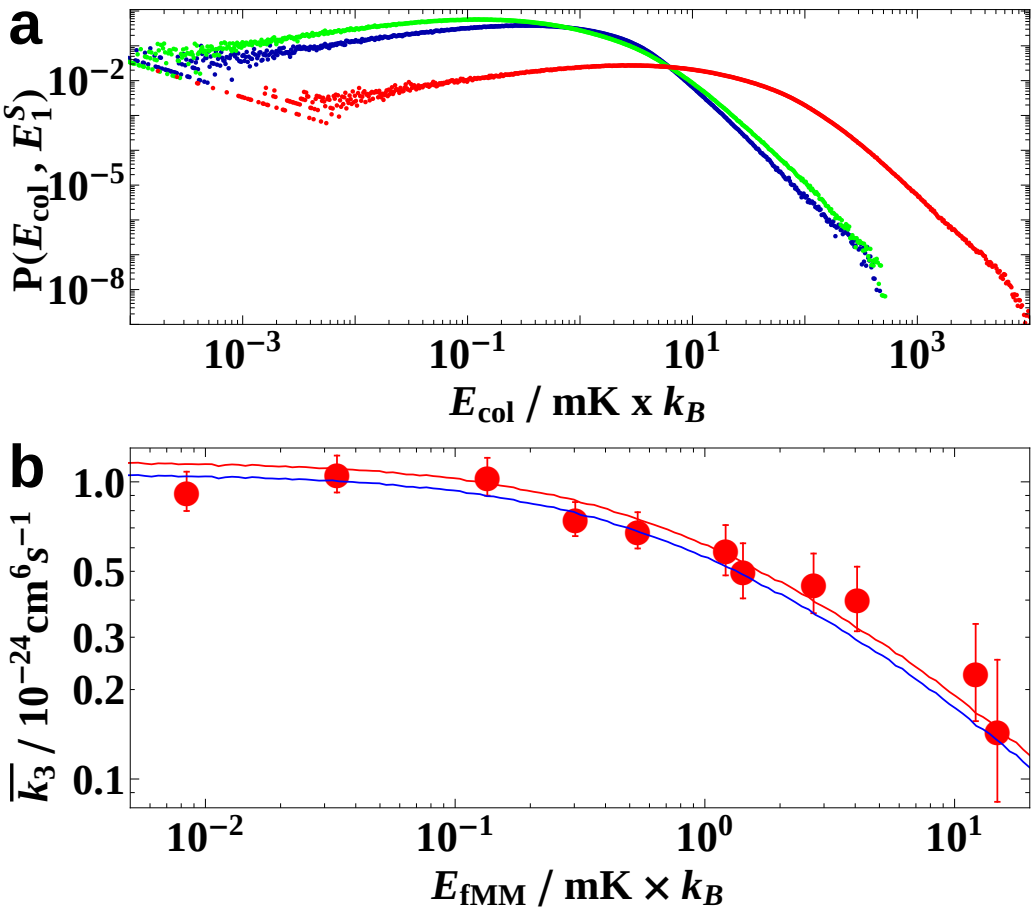

Figure D3: (a) Calculated ion energy distributions $P(E_{\rm col}, E_1^S)$ each with a single energy scale E_1^S. An energy of $E_1^S = E_{\rm fMM} = 1$ mK (20 mK) was used for the green (red) distribution. Choosing $E_1^S = E_{\phi\rm MM} = 1$ mK produces the blue distribution, which has a different shape compared to both previous distributions. (b) Comparison of the experimental (full circles) $\overline{k}_3$ data as a function of $E_{\rm fMM}$ with the full calculation (blue line). The red line is the same calculation but multiplied by 1.1.

collision energy $E_{\rm col}$. A fit to a power-law dependence gives $E_{\rm binding} \sim E_{\rm col}^{0.88\pm0.02}$ for the energy range investigated here. Thus our calculations suggest that the formation of deeply bound molecules after TBR should be highly improbable at low collision energies.

The present CTC results also suggest that $BaRb^+$ should be the dominant product state of the three-body recombination in the collision energy range considered here. Indeed, we have observed the formation of $BaRb^+$ ions in our experiment. However, collisional or light induced secondary processes lead to short lifetimes. A detailed study of the initial TBR products and involved secondary reactions is currently in progress and needs to be discussed elsewhere.

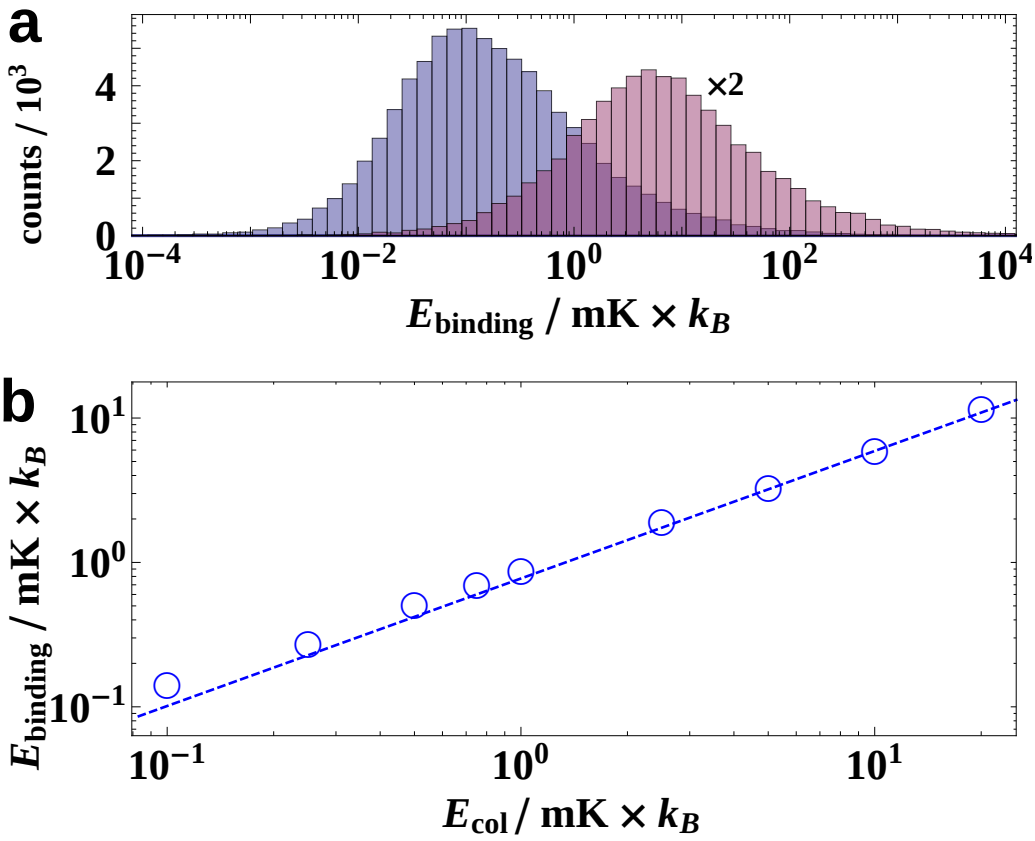

Figure D4: (a) Logarithmically binned histogram of the binding energies at collision energies of 100 μK$\times$ (blue) and 10 mK$\times$ (red). The second histogram is magnified by a factor of two. (b) Double-logarithmic plot of the typical binding energy of the formed molecule as a function of the collision energy. The dashed line represents a power law fit.

D7 Conclusion

In conclusion, we have investigated the energy scaling of three-body recombination in an atom-ion system down to mK energies. Single ions in contact with ultracold Rb atoms have been used to measure the TBR rate coefficient $\overline{k}_3$. Utilizing classical trajectory calculations, we numerically accessed the TBR rate coefficient k_3 for the + Rb + Rb system for various collision energies. We find a power law scaling of the form $k_3(E_{\rm col}) \propto E_{\rm col}^{\alpha}$ with an exponent $\alpha = -3/4$. Our experimental and theoretical studies indicate that the presence of several energy scales gives rise to energy distributions of the immersed ion that impede a direct application of scaling laws to the measured data. The obtained energy scaling provides an important insight for prospects of atom-ion experiments in the ultracold regime, as the already strong TBR rate observed here will increase by another three orders of magnitude

once the s-wave regime at 50 nK is reached.

This work was supported by the German Research Foundation DFG within the SFB/TRR21 and by the U.S. Department of Energy, Office of Science, under Award Number DE-SC0010545. A.K. acknowledges support from the Carl Zeiss Foundation. J.P.-R. and C.H.G. thank Francis Robicheaux for many fruitful discussions. J.H.D. and C.H.G acknowledge inspiring interactions within program INT-14-1.

Bibliography

[1] T. Hänsch and A. Schawlow, "Cooling of gases by laser radiation," Optics Communications, vol. 13, no. 1, pp. 68 – 69, 1975.

[2] D. Wineland and H. Dehmelt, "Proposed $10^{14} \triangle \nu < \nu$ laser fluorescence spectroscopy on TI^{+} mono-ion oscillator iii," Bull. Am. Phys. Soc., vol. 20, p. 637, 1975.

[3] D. J. Wineland, R. E. Drullinger, and F. L. Walls, "Radiation-pressure cooling of bound resonant absorbers," Phys. Rev. Lett., vol. 40, pp. 1639–1642, Jun 1978.

[4] W. Neuhauser, M. Hohenstatt, P. Toschek, and H. Dehmelt, "Optical-sideband cooling of visible atom cloud confined in parabolic well," Phys. Rev. Lett., vol. 41, pp. 233–236, Jul 1978.

[5] A. L. Migdall, J. V. Prodan, W. D. Phillips, T. H. Bergeman, and H. J. Metcalf, "First observation of magnetically trapped neutral atoms," Phys. Rev. Lett., vol. 54, pp. 2596–2599, Jun 1985.

[6] S. Chu, J. E. Bjorkholm, A. Ashkin, and A. Cable, "Experimental observation of optically trapped atoms," Phys. Rev. Lett., vol. 57, pp. 314–317, Jul 1986.

[7] W. D. Phillips, "Nobel lecture: Laser cooling and trapping of neutral atoms," Rev. Mod. Phys., vol. 70, pp. 721–741, Jul 1998.

[8] M. H. Anderson, J. R. Ensher, M. R. Matthews, C. E. Wieman, and E. A. Cornell, "Observation of Bose-Einstein condensation in a dilute atomic vapor," Science, vol. 269, no. 5221, pp. 198–201, 1995.

[9] K. B. Davis, M. O. Mewes, M. R. Andrews, N. J. van Druten, D. S. Durfee, D. M. Kurn, and W. Ketterle, "Bose-Einstein condensation in a gas of sodium atoms," Phys. Rev. Lett., vol. 75, pp. 3969–3973, Nov 1995.

[10] F. Diedrich, J. C. Bergquist, W. M. Itano, and D. J. Wineland, "Laser cooling to the zero-point energy of motion," Phys. Rev. Lett., vol. 62, pp. 403–406, Jan 1989.

[11] C. J. Ballance, T. P. Harty, N. M. Linke, M. A. Sepiol, and D. M. Lucas, "High-fidelity quantum logic gates using trapped-ion hyperfine qubits," Phys. Rev. Lett., vol. 117, p. 060504, Aug 2016.

[12] J. P. Gaebler, T. R. Tan, Y. Lin, Y. Wan, R. Bowler, A. C. Keith, S. Glancy, K. Coakley, E. Knill, D. Leibfried, and D. J. Wineland, "High-fidelity universal gate set for $^{9}Be^{+}$ ion qubits," Phys. Rev. Lett., vol. 117, p. 060505, Aug 2016.

[13] T. Rosenband, D. B. Hume, P. O. Schmidt, C. W. Chou, A. Brusch, L. Lorini, W. H. Oskay, R. E. Drullinger, T. M. Fortier, J. E. Stalnaker, S. A. Diddams, W. C. Swann, N. R. Newbury, W. M. Itano, D. J. Wineland, and J. C. Bergquist, "Frequency ratio of Al^{+} and Hg^{+} single-ion optical clocks; metrology at the 17th decimal place," Science, vol. 319, no. 5871, pp. 1808–1812, 2008.

[14] H. Haffner, W. Hansel, C. F. Roos, J. Benhelm, D. Chek-al kar, M. Chwalla, T. Korber, U. D. Rapol, M. Riebe, P. O. Schmidt, C. Becher, O. Guhne, W. Dur, and R. Blatt, "Scalable multiparticle entanglement of trapped ions," Nature, vol. 438, pp. 643–646, Dec 2005.

[15] T. Monz, P. Schindler, J. T. Barreiro, M. Chwalla, D. Nigg, W. A. Coish, M. Harlander, W. Hänsel, M. Hennrich, and R. Blatt, "14-qubit entanglement: Creation and coherence," Phys. Rev. Lett., vol. 106, p. 130506, Mar 2011.

[16] W. G. Rellergert, S. T. Sullivan, S. J. Schowalter, S. Kotochigova, K. Chen, and E. R. Hudson, "Evidence for sympathetic vibrational cooling of translationally cold molecules," Nature, vol. 495, pp. 490–494, Mar 2013.

[17] G. Werth, T. Beier, S. Djekic, H.-J. Kluge, W. Quint, T. Valenzuela, J. Verdu, and M. Vogel, "Precision studies in traps: Measurement of fundamental constants and tests of fundamental theories," Nuclear Instruments and Methods in Physics Research Section B: Beam Interactions with Materials and Atoms, vol. 205, pp. 1 – 8, 2003. 11th International Conference on the Physics of Highly Charged Ions.

[18] S. Giorgini, L. P. Pitaevskii, and S. Stringari, "Theory of ultracold atomic fermi gases," Rev. Mod. Phys., vol. 80, pp. 1215–1274, Oct 2008.

[19] M. Lewenstein, A. Sanpera, V. Ahufinger, B. Damski, A. Sen(De), and U. Sen, "Ultracold atomic gases in optical lattices: mimicking condensed matter physics and beyond," Advances in Physics, vol. 56, no. 2, pp. 243–379, 2007.

[20] E. A. Hinds and I. G. Hughes, "Magnetic atom optics: mirrors, guides, traps, and chips for atoms," Journal of Physics D: Applied Physics, vol. 32, pp. R119–R146, sep 1999.

[21] M. Keil, O. Amit, S. Zhou, D. Groswasser, Y. Japha, and R. Folman, "Fifteen years of cold matter on the atom chip: promise, realizations, and prospects," Journal of Modern Optics, vol. 63, no. 18, pp. 1840–1885, 2016.

[22] D. A. Meyer, "Quantum lattice gases and their invariants," International Journal of Modern Physics C, vol. 08, no. 04, pp. 717–735, 1997.

[23] T. Lahaye, C. Menotti, L. Santos, M. Lewenstein, and T. Pfau, "The physics of dipolar bosonic quantum gases," Reports on Progress in Physics, vol. 72, p. 126401, nov 2009.

[24] M. A. Baranov, M. Dalmonte, G. Pupillo, and P. Zoller, "Condensed matter theory of dipolar quantum gases," Chemical Reviews, vol. 112, no. 9, pp. 5012–5061, 2012. PMID: 22877362.

[25] K. Modi, "Quantum many-body physics in a nutshell," Contemporary Physics, vol. 60, no. 2, pp. 197–197, 2019.

[26] I. M. Georgescu, S. Ashhab, and F. Nori, "Quantum simulation," Rev. Mod. Phys., vol. 86, pp. 153–185, Mar 2014.

[27] M. Johanning, A. F. Varón, and C. Wunderlich, "Quantum simulations with cold trapped ions," Journal of Physics B: Atomic, Molecular and Optical Physics, vol. 42, p. 154009, jul 2009.

[28] A. J. Daley, "Quantum computing and quantum simulation with group-ii atoms," Quantum Information Processing, vol. 10, p. 865, Sep 2011.

[29] D. Jaksch, "Optical lattices, ultracold atoms and quantum information processing," Contemporary Physics, vol. 45, no. 5, pp. 367–381, 2004.

[30] R. V. Krems, "Cold controlled chemistry," Phys. Chem. Chem. Phys., vol. 10, pp. 4079–4092, 2008.

[31] B. R. Heazlewood, "Cold ion chemistry within coulomb crystals," Molecular Physics, vol. 117, no. 14, pp. 1934–1941, 2019.

[32] C. Zipkes, L. Ratschbacher, S. Palzer, C. Sias, and M. Köhl, "Hybrid quantum systems of atoms and ions," Journal of Physics: Conference Series, vol. 264, p. 012019, jan 2011.

[33] A. Härter and J. H. Denschlag, "Cold atom ion experiments in hybrid traps," Contemporary Physics, vol. 55, no. 1, pp. 33–45, 2014.

[34] M. Tomza, K. Jachymski, R. Gerritsma, A. Negretti, T. Calarco, Z. Idziaszek, and P. S. Julienne, "Cold hybrid ion-atom systems," Rev. Mod. Phys., vol. 91, p. 035001, Jul 2019.

[35] F. H. Hall, M. Aymar, M. Raoult, O. Dulieu, and S. Willitsch, "Light-assisted cold chemical reactions of barium ions with rubidium atoms," Molecular Physics, vol. 111, no. 12-13, pp. 1683–1690, 2013.

[36] F. H. Hall, P. Eberle, G. Hegi, M. Raoult, M. Aymar, O. Dulieu, and S. Willitsch, "Ion-neutral chemistry at ultralow energies: dynamics of reactive collisions between laser-cooled Ca^+ ions and Rb atoms in an ion-atom hybrid trap," Molecular Physics, vol. 111, no. 14-15, pp. 2020–2032, 2013.

[37] W. G. Rellergert, S. T. Sullivan, S. Kotochigova, A. Petrov, K. Chen, S. J. Schowalter, and E. R. Hudson, "Measurement of a large chemical reaction rate between ultracold closed-shell ^{40}Ca atoms and open-shell $^{174}Yb^+$ ions held in a hybrid atom-ion trap," Phys. Rev. Lett., vol. 107, p. 243201, Dec 2011.

[38] N. Akerman, Y. Glickman, S. Kotler, A. Keselman, and R. Ozeri, "Quantum control of $^{88}Sr^+$ in a miniature linear paul trap," Applied Physics B, vol. 107, no. 4, pp. 1167–1174, 2012.

[39] S. Haze, S. Hata, M. Fujinaga, and T. Mukaiyama, "Observation of elastic collisions between lithium atoms and calcium ions," Phys. Rev. A, vol. 87, p. 052715, May 2013.

[40] K. Ravi, S. Lee, A. Sharma, G. Werth, and S. A. Rangwala, "Cooling and stabilization by collisions in a mixed ion-atom system," Nat Commun, vol. 3, p. 1126, Oct 2012.

[41] R. Blümel, J. E. Wells, D. S. Goodman, J. M. Kwolek, and W. W. Smith, "Universal nonmonotonic structure in the saturation curves of magneto-optical-trap-loaded Na^+ ions stored in an ion-neutral hybrid trap: Prediction and observation," Phys. Rev. A, vol. 92, p. 063402, Dec 2015.

[42] W. Ketterle, K. B. Davis, M. A. Joffe, A. Martin, and D. E. Pritchard, "High densities of cold atoms in a dark spontaneous-force optical trap," Phys. Rev. Lett., vol. 70, pp. 2253–2256, Apr 1993.

[43] M. Tomza, C. P. Koch, and R. Moszynski, "Cold interactions between an Yb^+ ion and a Li atom: Prospects for sympathetic cooling, radiative association, and feshbach resonances," Phys. Rev. A, vol. 91, p. 042706, Apr 2015.

[44] F. H. Hall, P. Eberle, G. Hegi, M. Raoult, M. Aymar, O. Dulieu, and S. Willitsch, "Ion-neutral chemistry at ultralow energies: dynamics of reactive collisions between laser-cooled Ca^+ ions and Rb atoms in an ion-atom hybrid trap," Molecular Physics, vol. 111, no. 14-15, pp. 2020–2032, 2013.

[45] R. Côté, "From classical mobility to hopping conductivity: Charge hopping in an ultracold gas," Phys. Rev. Lett., vol. 85, pp. 5316–5319, Dec 2000.

[46] W. Casteels, J. Tempere, and J. T. Devreese, "Polaronic properties of an ion in a bose-einstein condensate in the strong-coupling limit," Journal of Low Temperature Physics, vol. 162, no. 3, pp. 266–273, 2011.

[47] R. Côté, V. Kharchenko, and M. D. Lukin, "Mesoscopic molecular ions in Bose-Einstein condensates," Phys. Rev. Lett., vol. 89, p. 093001, Aug 2002.

[48] S. Schmid, A. Härter, A. Frisch, S. Hoinka, and J. H. Denschlag, "An apparatus for immersing trapped ions into an ultracold gas of neutral atoms," Review of Scientific Instruments, vol. 83, no. 5, 2012.

[49] A. Härter, A. Krükow, A. Brunner, and J. Hecker Denschlag, "Minimization of ion micromotion using ultracold atomic probes," Applied Physics Letters, vol. 102, no. 22, p. 221115, 2013.

[50] B. L. Chuah, N. C. Lewty, R. Cazan, and M. D. Barrett, "Detection of ion micromotion in a linear paul trap with a high finesse cavity," Opt. Express, vol. 21, pp. 10632–10641, May 2013.

[51] U. Tanaka, K. Masuda, Y. Akimoto, K. Koda, Y. Ibaraki, and S. Urabe, "Micromotion compensation in a surface electrode trap by parametric excitation of trapped ions," Applied Physics B, vol. 107, pp. 907–912, Jun 2012.

[52] S. Narayanan, N. Daniilidis, S. A. Möller, R. Clark, F. Ziesel, K. Singer, F. Schmidt-Kaler, and H. Häffner, "Electric field compensation and sensing with a single ion in a planar trap," Journal of Applied Physics, vol. 110, no. 11, p. 114909, 2011.

[53] J. Keller, H. L. Partner, T. Burgermeister, and T. E. Mehlstäubler, "Precise determination of micromotion for trapped-ion optical clocks," Journal of Applied Physics, vol. 118, no. 10, p. 104501, 2015.

[54] Z. Meir, T. Sikorsky, R. Ben-shlomi, N. Akerman, M. Pinkas, Y. Dallal, and R. Ozeri, "Experimental apparatus for overlapping a ground-state cooled ion with ultracold atoms," Journal of Modern Optics, vol. 65, no. 5-6, pp. 501–519, 2018.

[55] M. D. Gregoire, I. Hromada, W. F. Holmgren, R. Trubko, and A. D. Cronin, "Measurements of the ground-state polarizabilities of cs, rb, and k using atom interferometry," Phys. Rev. A, vol. 92, p. 052513, Nov 2015.

[56] E. G. M. van Kempen, S. J. J. M. F. Kokkelmans, D. J. Heinzen, and B. J. Verhaar, "Interisotope determination of ultracold rubidium interactions from three high-precision experiments," Phys. Rev. Lett., vol. 88, p. 093201, Feb 2002.

[57] P. Langevin Ann. Chim. Phys, vol. 5, p. 245, 1905.

[58] J. J. Sakurai, Modern quantum mechanics; rev. ed. Reading, MA: Addison-Wesley, 1994.

[59] R. Côté and A. Dalgarno, "Ultracold atom-ion collisions," Phys. Rev. A, vol. 62, p. 012709, Jun 2000.

[60] Private comminucation with H. da Silva Jr. and O. Dulieu.

[61] D. J. Berkeland, J. D. Miller, J. C. Bergquist, W. M. Itano, and D. J. Wineland, "Minimization of ion micromotion in a paul trap," Journal of Applied Physics, vol. 83, no. 10, pp. 5025–5033, 1998.

[62] J. Ye, S. Swartz, P. Jungner, and J. L. Hall, "Hyperfine structure and absolute frequency of the ^{87}Rb 5P3/2 state," Opt. Lett., vol. 21, pp. 1280–1282, Aug 1996.

[63] S. Bize, Y. Sortais, M. S. Santos, C. Mandache, A. Clairon, and C. Salomon, "High-accuracy measurement of the ^{87} Rb ground-state hyperfine splitting in an atomic fountain," EPL (Europhysics Letters), vol. 45, no. 5, p. 558, 1999.

[64] T. Esslinger, I. Bloch, and T. W. Hänsch, "Bose-einstein condensation in a quadrupole-ioffe-configuration trap," Phys. Rev. A, vol. 58, pp. R2664–R2667, Oct 1998.

[65] H. Häffner, C. Roos, and R. Blatt, "Quantum computing with trapped ions," Physics Reports, vol. 469, no. 4, pp. 155 – 203, 2008.

[66] A. Bermudez, P. Schindler, T. Monz, R. Blatt, and M. Müller, "Micromotion-enabled improvement of quantum logic gates with trapped ions," New Journal of Physics, vol. 19, no. 11, p. 113038, 2017.

[67] M. Johanning, A. F. Varón, and C. Wunderlich, "Quantum simulations with cold trapped ions," Journal of Physics B: Atomic, Molecular and Optical Physics, vol. 42, no. 15, p. 154009, 2009.

[68] D. J. Wineland, W. M. Itano, J. C. Bergquist, and R. G. Hulet, "Laser-cooling limits and single-ion spectroscopy," Phys. Rev. A, vol. 36, pp. 2220–2232, Sep 1987.

[69] A. L. Wolf, S. A. van den Berg, C. Gohle, E. J. Salumbides, W. Ubachs, and K. S. E. Eikema, "Frequency metrology on the $4s\,^2s_{12} - 4p\,^2p_{12}$ transition in $^{40}Ca^+$ for a comparison with quasar data," Phys. Rev. A, vol. 78, p. 032511, Sep 2008.

[70] A. D. Ludlow, M. M. Boyd, J. Ye, E. Peik, and P. O. Schmidt, "Optical atomic clocks," Rev. Mod. Phys., vol. 87, pp. 637–701, Jun 2015.

[71] A. Härter and J. H. Denschlag, "Cold atom – ion experiments in hybrid traps," Contemporary Physics, vol. 55, no. 1, pp. 33–45, 2014.

[72] D. Zhang and S. Willitsch, "Chapter 10 cold ion chemistry," in Cold Chemistry: Molecular Scattering and Reactivity Near Absolute Zero, pp. 496–536, The Royal Society of Chemistry, 2018.

[73] D. T. C. Allcock, J. A. Sherman, D. N. Stacey, A. H. Burrell, M. J. Curtis, G. Imreh, N. M. Linke, D. J. Szwer, S. C. Webster, A. M. Steane, and D. M. Lucas, "Implementation of a symmetric surface-electrode ion trap with field compensation using a modulated raman effect," New Journal of Physics, vol. 12, no. 5, p. 053026, 2010.

[74] T. F. Gloger, P. Kaufmann, D. Kaufmann, M. T. Baig, T. Collath, M. Johanning, and C. Wunderlich, "Ion-trajectory analysis for micromotion minimization and the measurement of small forces," Phys. Rev. A, vol. 92, p. 043421, Oct 2015.

[75] T. Huber, A. Lambrecht, J. Schmidt, L. Karpa, and T. Schaetz, "A far-off-resonance optical trap for a ba+ ion," Nature Communications, vol. 5, p. 5587, Nov 2014.

[76] A. Brunner, "Excess micromotion in atom-ionen experimenten," diploma thesis, Universität Ulm, 2013.

[77] P. F. Herskind, A. Dantan, M. Albert, J. P. Marler, and M. Drewsen, "Positioning of the rf potential minimum line of a linear paul trap with micrometer precision," vol. 42, p. 154008, jul 2009.

[78] M. Cetina, A. T. Grier, and V. Vuletić, "Micromotion-induced limit to atom-ion sympathetic cooling in paul traps," Phys. Rev. Lett., vol. 109, p. 253201, Dec 2012.

[79] T. Secker, N. Ewald, J. Joger, H. Fürst, T. Feldker, and R. Gerritsma, "Trapped ions in rydberg-dressed atomic gases," Phys. Rev. Lett., vol. 118, p. 263201, Jun 2017.

[80] L. H. Nguyên, A. Kalev, M. D. Barrett, and B.-G. Englert, "Micromotion in trapped atom-ion systems," Phys. Rev. A, vol. 85, p. 052718, May 2012.

[81] B. Höltkemeier, P. Weckesser, H. López-Carrera, and M. Weidemüller, "Buffer-gas cooling of a single ion in a multipole radio frequency trap beyond the critical mass ratio," Phys. Rev. Lett., vol. 116, p. 233003, Jun 2016.

[82] C. Zipkes, L. Ratschbacher, C. Sias, and M. Köhl, "Kinetics of a single trapped ion in an ultracold buffer gas," New Journal of Physics, vol. 13, p. 053020, may 2011.

[83] S. Haze, M. Sasakawa, R. Saito, R. Nakai, and T. Mukaiyama, "Cooling dynamics of a single trapped ion via elastic collisions with small-mass atoms," Phys. Rev. Lett., vol. 120, p. 043401, Jan 2018.

[84] S. Dutta, R. Sawant, and S. A. Rangwala, "Collisional cooling of light ions by cotrapped heavy atoms," Phys. Rev. Lett., vol. 118, p. 113401, Mar 2017.

[85] I. Rouse and S. Willitsch, "Energy distributions of an ion in a radio-frequency trap immersed in a buffer gas under the influence of additional external forces," Phys. Rev. A, vol. 97, p. 042712, Apr 2018.

[86] H. da Silva Jr, M. Raoult, M. Aymar, and O. Dulieu, "Formation of molecular ions by radiative association of cold trapped atoms and ions," New Journal of Physics, vol. 17, no. 4, p. 045015, 2015.

[87] H. A. Fürst, N. V. Ewald, T. Secker, J. Joger, T. Feldker, and R. Gerritsma, "Prospects of reaching the quantum regime in Li-Yb^+ mixtures," Journal of Physics B: Atomic, Molecular and Optical Physics, vol. 51, p. 195001, sep 2018.

[88] K. M. Jones, E. Tiesinga, P. D. Lett, and P. S. Julienne, "Ultracold photoassociation spectroscopy: Long-range molecules and atomic scattering," Rev. Mod. Phys., vol. 78, pp. 483–535, May 2006.

[89] J. M. Hutson and P. Soldán, "Molecule formation in ultracold atomic gases," International Reviews in Physical Chemistry, vol. 25, no. 4, pp. 497–526, 2006.

[90] J. Ulmanis, J. Deiglmayr, M. Repp, R. Wester, and M. Weidemüller, "Ultracold molecules formed by photoassociation: Heteronuclear dimers, inelastic collisions, and interactions with ultrashort laser pulses," Chemical Reviews, vol. 112, no. 9, pp. 4890–4927, 2012. PMID: 22931226.

[91] T. Köhler, K. Góral, and P. S. Julienne, "Production of cold molecules via magnetically tunable feshbach resonances," Rev. Mod. Phys., vol. 78, pp. 1311–1361, Dec 2006.

[92] C. Chin, R. Grimm, P. Julienne, and E. Tiesinga, "Feshbach resonances in ultracold gases," Rev. Mod. Phys., vol. 82, pp. 1225–1286, Apr 2010.

[93] F. H. J. Hall, M. Aymar, N. Bouloufa-Maafa, O. Dulieu, and S. Willitsch, "Light-assisted ion-neutral reactive processes in the cold regime: Radiative molecule formation versus charge exchange," Phys. Rev. Lett., vol. 107, p. 243202, Dec 2011.

[94] C. H. Greene, P. Giannakeas, and J. Pérez-Ríos, "Universal few-body physics and cluster formation," Rev. Mod. Phys., vol. 89, p. 035006, Aug 2017.

[95] J. Meyer and R. Wester, "Ion–molecule reaction dynamics," Annual Review of Physical Chemistry, vol. 68, no. 1, pp. 333–353, 2017. PMID: 28463654.

[96] B. R. Heazlewood and T. P. Softley, "Low-temperature kinetics and dynamics with coulomb crystals," Annual Review of Physical Chemistry, vol. 66, no. 1, pp. 475–495, 2015. PMID: 25594853.

[97] J. Mikosch, M. Weidemüller, and R. Wester, "On the dynamics of chemical reactions of negative ions," International Reviews in Physical Chemistry, vol. 29, no. 4, pp. 589–617, 2010.

[98] D. Gerlich, The Study of Cold Collisions Using Ion Guides and Traps, pp. 121–174.

[99] K. Jachymski and F. Meinert, "Vibrational quenching of weakly bound cold molecular ions immersed in their parent gas," Applied Sciences, vol. 10, no. 7, p. 2371, 2020.

[100] A. T. Grier, M. Cetina, F. Oručević, and V. Vuletić, "Observation of cold collisions between trapped ions and trapped atoms," Phys. Rev. Lett., vol. 102, p. 223201, Jun 2009.

[101] S. Schmid, A. Härter, and J. H. Denschlag, "Dynamics of a cold trapped ion in a Bose-Einstein condensate," Phys. Rev. Lett., vol. 105, p. 133202, Sep 2010.

[102] L. Ratschbacher, C. Zipkes, C. Sias, and M. Köhl, "Controlling chemical reactions of a single particle," Nature Physics, vol. 8, pp. 649–652, Sep 2012.

[103] D. S. Goodman, J. E. Wells, J. M. Kwolek, R. Blümel, F. A. Narducci, and W. W. Smith, "Measurement of the low-energy $Na^+ - Na$ total collision rate in an ion-neutral hybrid trap," Phys. Rev. A, vol. 91, p. 012709, Jan 2015.

[104] S. Haze, R. Saito, M. Fujinaga, and T. Mukaiyama, "Charge-exchange collisions between ultracold fermionic lithium atoms and calcium ions," Phys. Rev. A, vol. 91, p. 032709, Mar 2015.

[105] J. Joger, H. Fürst, N. Ewald, T. Feldker, M. Tomza, and R. Gerritsma, "Observation of collisions between cold Li atoms and Yb^+ ions," Phys. Rev. A, vol. 96, p. 030703, Sep 2017.

[106] T. Sikorsky, Z. Meir, R. Ben-shlomi, N. Akerman, and R. Ozeri, "Spin-controlled atom-ion chemistry," Nature Communications, vol. 9, p. 920, Mar 2018.

[107] H. Fürst, T. Feldker, N. V. Ewald, J. Joger, M. Tomza, and R. Gerritsma, "Dynamics of a single ion-spin impurity in a spin-polarized atomic bath," Phys. Rev. A, vol. 98, p. 012713, Jul 2018.

[108] D. Hauser, S. Lee, F. Carelli, S. Spieler, O. Lakhmanskaya, E. S. Endres, S. S. Kumar, F. Gianturco, and R. Wester, "Rotational state-changing cold collisions of hydroxyl ions with helium," Nature Physics, vol. 11, pp. 467–470, Jun 2015.

[109] A. Härter, A. Krükow, A. Brunner, W. Schnitzler, S. Schmid, and J. H. Denschlag, "Single ion as a three-body reaction center in an ultracold atomic gas," Phys. Rev. Lett., vol. 109, p. 123201, Sep 2012.

[110] F. H. Hall, M. Aymar, M. Raoult, O. Dulieu, and S. Willitsch, "Light-assisted cold chemical reactions of barium ions with rubidium atoms," Molecular Physics, vol. 111, no. 12-13, pp. 1683–1690, 2013.

[111] S. T. Sullivan, W. G. Rellergert, S. Kotochigova, K. Chen, S. J. Schowalter, and E. R. Hudson, "Trapping molecular ions formed via photo-associative ionization of ultracold atoms," Phys. Chem. Chem. Phys., vol. 13, pp. 18859–18863, 2011.

[112] F. H. J. Hall and S. Willitsch, "Millikelvin reactive collisions between sympathetically cooled molecular ions and laser-cooled atoms in an ion-atom hybrid trap," Phys. Rev. Lett., vol. 109, p. 233202, Dec 2012.

[113] J. Deiglmayr, A. Göritz, T. Best, M. Weidemüller, and R. Wester, "Reactive collisions of trapped anions with ultracold atoms," Phys. Rev. A, vol. 86, p. 043438, Oct 2012.

[114] P. Puri, M. Mills, C. Schneider, I. Simbotin, J. A. Montgomery, R. Côté, A. G. Suits, and E. R. Hudson, "Synthesis of mixed hypermetallic oxide $BaOCa^+$ from laser-cooled reagents in an atom-ion hybrid trap," Science, vol. 357, no. 6358, pp. 1370–1375, 2017.

[115] P. Puri, M. Mills, I. Simbotin, J. A. Montgomery, R. Côté, C. Schneider, A. G. Suits, and E. R. Hudson, "Reaction blockading in a reaction between an excited atom and a charged molecule at low collision energy," Nature Chemistry, vol. 11, pp. 615–621, Jul 2019.

[116] We use the vertical ODT beam with an intensity of $1.8\,\mathrm{kW\,cm^{-2}}$ which is only about 10% of the intensity of the crossed ODT used for the experiments in figure 5.2. The light is switched on for 300 ms which is about three orders of magnitude longer than the typical photodissociation time scale.

[117] About a quarter of the cold Ba^+ signal stems from experiments where due to a technical glitch no initial Rb cloud was produced and therefore the Ba^+ ion could never collide with Rb atoms. These glitches occur in about 1% of all runs.

[118] The subsitution reaction $BaRb^+ + Rb \rightarrow BaRb + Rb^+$ can be neglected, as discussed in Appendix B4.1.

[119] The $X^1\Sigma_g^+$ electronic ground state of the Rb_2 molecule has a potential depth of about $4000\,\mathrm{cm^{-1}}$ [128]. Furthermore, e.g. the vibrational level $v = 55$ of the $(X)^1\Sigma^+$ state of the $BaRb^+$ molecule has a binding energy of about $3800\,\mathrm{cm^{-1}}$. When assuming that in the substitution reaction $BaRb^+ + Rb \rightarrow Ba + Rb_2^+$ a Rb_2^+ molecule can be produced with about the same binding energy as the former $BaRb^+$ molecule then the substitution reaction $Rb_2^+ + Rb \rightarrow Rb^+ + Rb_2$ is energetically allowed.

[120] Photodissociation of a $BaRb^+$ molecule in the $(X)^1\Sigma^+$ state is also possible with a photon at 614nm. We do not take into account this process here, because when working with the 614 nm laser only low powers of a few W were used.

[121] M. Larsson, W. D. Geppert, and G. Nyman, "Ion chemistry in space," Reports on Progress in Physics, vol. 75, p. 066901, may 2012.

[122] T. P. Snow and V. M. Bierbaum, "Ion chemistry in the interstellar medium," Annual Review of Analytical Chemistry, vol. 1, no. 1, pp. 229–259, 2008. PMID: 20636080.

[123] S. Petrie and D. K. Bohme, "Ions in space," Mass Spectrometry Reviews, vol. 26, no. 2, pp. 258–280, 2007.

[124] D. Smith, "The ion chemistry of interstellar clouds," Chemical Reviews, vol. 92, no. 7, pp. 1473–1485, 1992.

[125] The measured atom number is $6.0 \pm 1.2 \times 10^6$. In our model simulations we use 6.2×10^6 because this optimizes the agreement with the experimental data.

[126] A. Härter, A. Krükow, M. Deiß, B. Drews, E. Tiemann, and J. H. Denschlag, "Population distribution of product states following three-body recombination in an ultracold atomic gas," Nature Physics, vol. 9, pp. 512 EP –, Jun 2013. Article.

[127] J. Pérez-Ríos, "Vibrational quenching and reactive processes of weakly bound molecular ions colliding with atoms at cold temperatures," Phys. Rev. A, vol. 99, p. 022707, Feb 2019.

[128] C. Strauss, T. Takekoshi, F. Lang, K. Winkler, R. Grimm, J. Hecker Denschlag, and E. Tiemann, "Hyperfine, rotational, and vibrational structure of the $a^3\Sigma_u^+$ state of $^{87}Rb_2$," Phys. Rev. A, vol. 82, p. 052514, Nov 2010.

[129] M. D. Gregoire, I. Hromada, W. F. Holmgren, R. Trubko, and A. D. Cronin, "Measurements of the ground-state polarizabilities of Cs, Rb, and K using atom interferometry," Phys. Rev. A, vol. 92, p. 052513, Nov 2015.

[130] S. Schäfer, M. Mehring, R. Schäfer, and P. Schwerdtfeger, "Polarizabilities of ba and ba_2: Comparison of molecular beam experiments with relativistic quantum chemistry," Phys. Rev. A, vol. 76, p. 052515, Nov 2007.

[131] R. V. Krems and A. Dalgarno, "Quantum-mechanical theory of atom-molecule and molecular collisions in a magnetic field: Spin depolarization," The Journal of Chemical Physics, vol. 120, no. 5, pp. 2296–2307, 2004.

[132] A. V. Avdeenkov and J. L. Bohn, "Ultracold collisions of oxygen molecules," Phys. Rev. A, vol. 64, p. 052703, Oct 2001.

[133] A. Dalgarno, M. R. H. Rudge, and D. R. Bates, "Spin-change cross-sections for collisions between alkali atoms," Proceedings of the Royal Society of London. Series A. Mathematical and Physical Sciences, vol. 286, no. 1407, pp. 519–524, 1965.

[134] L. Ratschbacher, Ph.D. thesis, St Catherine's college, University of Cambridge, 2013.

[135] M. Aymar and O. Dulieu, "Calculation of accurate permanent dipole moments of the lowest $\Sigma^{+1,3}$ states of heteronuclear alkali dimers using extended basis sets," The Journal of Chemical Physics, vol. 122, no. 20, p. 204302, 2005.

[136] M. Aymar and O. Dulieu, "Comment on "calculation of accurate permanent dipole moments of the lowest $\Sigma^{+1,3}$ states of heteronuclear alkali dimers using extended basis sets" [j. chem. phys. 122, 204302 (2005)]," The Journal of Chemical Physics, vol. 125, no. 4, p. 047101, 2006.

[137] M. Aymar, R. Guérout, and O. Dulieu, "Structure of the alkali-metal-atom + strontium molecular ions: Towards photoassociation and formation of cold molecular ions," The Journal of Chemical Physics, vol. 135, no. 6, p. 064305, 2011.

[138] B. Huron, J. P. Malrieu, and P. Rancurel, "Iterative perturbation calculations of ground and excited state energies from multiconfigurational zeroth-order wavefunctions," The Journal of Chemical Physics, vol. 58, no. 12, pp. 5745–5759, 1973.

[139] P. Durand and J. Barthelat, "New atomic pseudopotentials for electronic structure calculations of molecules and solids," Chemical Physics Letters, vol. 27, no. 2, pp. 191 – 194, 1974.

[140] P. Durand and J.-C. Barthelat, "A theoretical method to determine atomic pseudopotentials for electronic structure calculations of molecules and solids," Theoretica chimica acta, vol. 38, pp. 283–302, Dec 1975.

[141] P. Fuentealba, L. von Szentpaly, H. Preuss, and H. Stoll, "Pseudopotential calculations for alkaline-earth atoms," Journal of Physics B: Atomic and Molecular Physics, vol. 18, pp. 1287–1296, apr 1985.

[142] P. Fuentealba and O. Reyes, "Pseudopotential calculations on the ground state of the alkaline-earth monohydride ions," Molecular Physics, vol. 62, no. 6, pp. 1291–1296, 1987.

[143] W. Müller, J. Flesch, and W. Meyer, "Treatment of intershell correlation effects in ab initio calculations by use of core polarization potentials. method and application to alkali and alkaline earth atoms," The Journal of Chemical Physics, vol. 80, no. 7, pp. 3297–3310, 1984.

[144] M. Foucrault, P. Millie, and J. P. Daudey, "Nonperturbative method for core–valence correlation in pseudopotential calculations: Application to the Rb_2 and Cs_2 molecules," The Journal of Chemical Physics, vol. 96, no. 2, pp. 1257–1264, 1992.

[145] R. Guérout, M. Aymar, and O. Dulieu, "Ground state of the polar alkali-metal-atom–strontium molecules: Potential energy curve and permanent dipole moment," Phys. Rev. A, vol. 82, p. 042508, Oct 2010.

[146] M. Aymar and O. Dulieu, "The electronic structure of the alkaline-earth-atom (Ca, Sr, Ba) hydride molecular ions," Journal of Physics B: Atomic, Molecular and Optical Physics, vol. 45, p. 215103, oct 2012.

[147] T. Bouissou, G. Durand, M.-C. Heitz, and F. Spiegelman, "A comprehensive theoretical investigation of the electronic states of Ca_2 up to the Ca(4s2s1)+Ca(4s5pp1) dissociation limit," The Journal of Chemical Physics, vol. 133, no. 16, p. 164317, 2010.

[148] V. Kokoouline, O. Dulieu, R. Kosloff, and F. Masnou-Seeuws, "Mapped fourier methods for long-range molecules: Application to perturbations in the $Rb_2(0u^+)$ photoassociation spectrum," The Journal of Chemical Physics, vol. 110, no. 20, pp. 9865–9876, 1999.

[149] B. R. Johnson, "The renormalized numerov method applied to calculating bound states of the coupled-channel schroedinger equation," The Journal of Chemical Physics, vol. 69, no. 10, pp. 4678–4688, 1978.

[150] K. P. Kirby and E. F. V. Dishoeck], "Photodissociation processes in diatomic molecules of astrophysical interest," vol. 25 of Advances in Atomic and Molecular Physics, pp. 437 – 476, Academic Press, 1989.

[151] S. Bovino, M. Tacconi, and F. A. Gianturco, "Photon-induced evolutionary rates of LiHe $^+$ ($^1\Sigma^+$) in early universe from accurate quantum computations," The Astrophysical Journal, vol. 740, p. 101, oct 2011.

[152] A. Hansson and J. K. Watson, "A comment on Hönl-London factors," Journal of Molecular Spectroscopy, vol. 233, no. 2, pp. 169 – 173, 2005.

[153] Figure B4 indicates that for the transition $(1)^3\Sigma^+ \rightarrow (3)^3\Pi$ a deviation from the scaling law sets in at about $10\,\mathrm{K} \times k_\mathrm{B}$. For $(2)^1\Sigma^+ \rightarrow (4)^1\Sigma^+$ and $(1)^3\Sigma^+ \rightarrow$

$(3)^3\Sigma^+$ such deviations set in at higher energies of $60\,\mathrm{K} \times k_\mathrm{B}$ and $600\,\mathrm{K} \times k_\mathrm{B}$, respectively (not shown in figure B4). For the $(2)^1\Sigma^+ \rightarrow (4)^1\Sigma^+$ transition, the deviation can partially be explained by distortions of the wave functions due to the double-well structure of the singlet entrance channel PEC [see figure 5.1(b)].

[154] Photodissociation Dynamics: Spectroscopy and Fragmentation of Small Polyatomic Molecules, (Cambridge University Press, Cambridge, 1993), Chap. 6, p. 109.

[155] L. D. Landau, E. M. Lifshitz, *Quantum Mechanics (Third Edition)* (Pergamon, 1977).

[156] C. Sias and M. Köhl, "Hybrid quantum systems of ions and atoms," Quantum Gas Experiments, World Scientific Publishing, Singapore, p. 267, 2014.

[157] S. Willitsch, "Ion-atom hybrid systems," Proc. Int. Sch. Phys. Enrico Fermi, vol. 189, p. 255, 2015.

[158] M. Krych, W. Skomorowski, F. Pawłowski, R. Moszynski, and Z. Idziaszek, "Sympathetic cooling of the Ba^+ ion by collisions with ultracold Rb atoms: Theoretical prospects," Phys. Rev. A, vol. 83, p. 032723, Mar 2011.

[159] H. Doerk, Z. Idziaszek, and T. Calarco, "Atom-ion quantum gate," Phys. Rev. A, vol. 81, p. 012708, Jan 2010.

[160] U. Bissbort, D. Cocks, A. Negretti, Z. Idziaszek, T. Calarco, F. Schmidt-Kaler, W. Hofstetter, and R. Gerritsma, "Emulating solid-state physics with a hybrid system of ultracold ions and atoms," Phys. Rev. Lett., vol. 111, p. 080501, Aug 2013.

[161] D. S.-K. D. Ketterle, D. Durfee, "Bose-Einstein condensation in atomic gases, proceedings of the international school of physics enrico fermi, course cxl, varenna," pp. 7–17, 1999.

[162] O. P. Makarov, R. Côté, H. Michels, and W. W. Smith, "Radiative charge-transfer lifetime of the excited state of $(NaCa)^+$," Phys. Rev. A, vol. 67, p. 042705, Apr 2003.

[163] S. T. Sullivan, W. G. Rellergert, S. Kotochigova, and E. R. Hudson, "Role of electronic excitations in ground-state-forbidden inelastic collisions between ultracold atoms and ions," Phys. Rev. Lett., vol. 109, p. 223002, Nov 2012.

[164] C. Zipkes, S. Palzer, L. Ratschbacher, C. Sias, and M. Köhl, "Cold heteronuclear atom-ion collisions," Phys. Rev. Lett., vol. 105, p. 133201, Sep 2010.

[165] W. W. Smith, D. S. Goodman, I. Sivarajah, J. E. Wells, S. Banerjee, R. Côté, H. H. Michels, J. A. Mongtomery, and F. A. Narducci, "Experiments with an ion-neutral hybrid trap: cold charge-exchange collisions," Applied Physics B, vol. 114, pp. 75–80, Jan 2014.

[166] See Appendix D of this dissertation for more detail.

[167] R. G. DeVoe, "Power-law distributions for a trapped ion interacting with a classical buffer gas," Phys. Rev. Lett., vol. 102, p. 063001, Feb 2009.

[168] M. Krych and Z. Idziaszek, "Description of ion motion in a paul trap immersed in a cold atomic gas," Phys. Rev. A, vol. 91, p. 023430, Feb 2015.

[169] J. Pérez-Ríos and C. H. Greene, "Communication: Classical threshold law for ion-neutral-neutral three-body recombination," The Journal of Chemical Physics, vol. 143, no. 4, p. 041105, 2015.

[170] B. D. Esry, C. H. Greene, and J. P. Burke, "Recombination of three atoms in the ultracold limit," Phys. Rev. Lett., vol. 83, pp. 1751–1754, Aug 1999.

[171] H. F. Hess, D. A. Bell, G. P. Kochanski, R. W. Cline, D. Kleppner, and T. J. Greytak, "Observation of three-body recombination in spin-polarized hydrogen," Phys. Rev. Lett., vol. 51, pp. 483–486, Aug 1983.

[172] E. A. Burt, R. W. Ghrist, C. J. Myatt, M. J. Holland, E. A. Cornell, and C. E. Wieman, "Coherence, correlations, and collisions: What one learns about Bose-Einstein condensates from their decay," Phys. Rev. Lett., vol. 79, pp. 337–340, Jul 1997.

[173] J. P. D'Incao and B. D. Esry, "Scattering length scaling laws for ultracold three-body collisions," Phys. Rev. Lett., vol. 94, p. 213201, Jun 2005.

[174] P. S. Krstić, R. K. Janev, and D. R. Schultz, "Three-body, diatomic association in cold hydrogen plasmas," Journal of Physics B: Atomic, Molecular and Optical Physics, vol. 36, no. 16, p. L249, 2003.

[175] R. Plašil, I. Zymak, P. Jusko, D. Mulin, D. Gerlich, and J. Glosík, "Stabilization of H^+–H_2 collision complexes between 11 and 28k," Philosophical

Transactions of the Royal Society of London A: Mathematical, Physical and Engineering Sciences, vol. 370, no. 1978, pp. 5066–5073, 2012.

[176] C. Zipkes, S. Palzer, C. Sias, and M. Köhl, "A trapped single ion inside a Bose-Einstein condensate," Nature, vol. 464, pp. 388–391, 2010.

[177] I. Sivarajah, D. S. Goodman, J. E. Wells, F. A. Narducci, and W. W. Smith, "Evidence of sympathetic cooling of Na^+ ions by a Na magneto-optical trap in a hybrid trap," Phys. Rev. A, vol. 86, p. 063419, Dec 2012.

[178] See Appendix C of this dissertation for more detail.

[179] J. Pérez-Ríos, S. Ragole, J. Wang, and C. H. Greene, "Comparison of classical and quantal calculations of helium three-body recombination," J. Chem. Phys., vol. 140, no. 4, pp. –, 2014.

Erklärung

Ich versichere hiermit, dass ich die Arbeit selbständig angefertigt habe und keine anderen als die angegebenen Quellen und Hilfsmittel benutzt sowie die wörtlich oder inhaltlich übernommenen Stellen als solche kenntlich gemacht habe.

Ulm, den

.....
Vorname Nachname / Unterschrift

Acknowledgment

I would like to express my sincere gratitude to my supervisor, Professor Johannes Hecker Denschlag for giving me this chance to work on the Barium Rubidium Ion Experiment (BaRbIE). He convincingly guided and encouraged me to be professional and do the right thing even when the road got tough.
I would like to thank my colleagues in the lab: Artjom for what I have learned from him, from operating the system to fruitful discussions we had about experiments. Joschka, for being always supportive, friendly, and providing me the necessary tools for doing my experiments. Amir, who was always open to new discussions and challenges and also for helping me to do my experiments by taking care of the experimental machine.
My special thanks go to Markus for all supports and assistance he has given me, in particular, the correction of my manuscripts which were time-consuming tasks.
Besides my colleagues, I would like to thank Moritz who was simply great and very friendly. He was always extremely patient and supportive so I enjoyed working with him. Also, I thank Holger, Wolfgang, and Wladimir for being nice to me and helping me when things went wrong during the work. I thank Daniel and Thomas for keeping the doors of LiLaLab open for the BaRbIE team and did not hesitate to help us.
My thanks and appreciations also go to previous and the present secretaries of the institute, Martina and Astrid, for being very kind to me and for assisting me in many different ways and handling all paperwork.
Last but not least, I would like to thank my beautiful wife, Sepideh, for all sacrifices she has made for our life which I will never be able to compensate for her. Without her support and encouragement, finishing this dissertation was not possible for me. I also would like to thank Mehran, my lovely brother, that took care of everything when I was far from home.